Ab-initio **dynamics of Electrons and Nuclei in Solids**

Dissertation

zur Erlangung des Doktorgrades der Naturwissenschaften
(Dr. rer. nat.)

der

Naturwissenschaftlichen Fakultät II
Chemie, Physik und Mathematik

der Martin-Luther-Universität
Halle-Wittenberg,

vorgelegt von

Chung-Yu Wang

Gutachter:

Prof. Dr. E. K. U. Groß (Betreuer), Prof. Dr. I. Mertig,
und Prof. Dr. C. Ullrich (Univeristy of Missouri at Columbia)

Verteidigung: 06.05.2024

Notation

General

- Unless otherwise stated, all quantities throughout this work are given in atomic units (a.u.), i.e. $\hbar = |e| = m_\mathrm{e} = 1$. The vacuum speed of light is then equal to the inverse of the fine-structure constant, $c \approx 137$. The Bohr magneton is simply given by $\mu_\mathrm{B} = \frac{1}{2c}$.

Abbreviations

ALDA   Adiabatic LDA
APW   Augmented plane wave
BZ   Brillouin Zone
DFT   Density functional theory
DOS   Density of states
EMW   Electromagnetic wave
FWHM   Full width at half-maximum
GS   Ground state
HK   Hohenberg-Kohn
IR   Interstitial region
KS   Kohn-Sham
LAPW   Linearised Augmented plane wave
LDA   Local density approximation
MT   Muffin-tin
RG   Runge-Gross
SC-DFT   Superconducting DFT
TD-DFT   Time-dependent DFT
TRS   Time-reversal symmetry
XC   Exchange-correlation

Contents

1.   Introduction

One of the most important corner stones of modern condensed-matter theory is the adiabatic approximation. It rests on the intuitive picture that the electrons instantaneously adjust to the nuclear positions and hence are well-described by eigenfunctions of a Coulomb Hamiltonian with *clamped* nuclear positions, the well-known Born-Oppenheimer (BO) Hamiltonian[1]. The BO eigenfunctions $\psi_{\underline{\boldsymbol{R}}}^{\text{BO}}(\underline{\boldsymbol{r}})$ depend parametrically on the nuclear positions $\underline{\boldsymbol{R}}$ and have the physical meaning of a conditional probability amplitude of finding the electrons at positions $\underline{\boldsymbol{r}}$, given the nuclei are at the (clamped) positions $\underline{\boldsymbol{R}}$. By multiplying such a BO state with a nuclear probability amplitude $\chi(\underline{\boldsymbol{R}}, t)$, which may be time-dependent or static, one obtains the total electron-nuclear wave function in *adiabatic approximation*. The nuclear probability amplitude is obtained as solution of a (time-dependent or stationary) Schrödinger equation in which the electronic BO eigenvalue as function of nuclear coordinates serves as scalar potential. Often the latter is treated in harmonic approximation, yielding harmonic-oscillator states in terms of suitable collective coordinates, or vibrational wave packets (coherent phonons) in the time-dependent case.

By definition, the adiabatic approximation means that one and only one BO surface is involved in the process. One may deduce the adiabatic approximation by expanding the full electron-nuclear wave function in the complete basis of BO states (the so-called Born-Huang expansion[2]), plugging this expansion into the time-dependent Schrödinger equation and subsequently neglecting the non-adiabatic coupling matrix elements[3].

The adiabatic approximation not only makes computations feasible, it also provides an intuitive picture of many phenomena, such as chemical reactions and isomerization processes, vibrational spectroscopy as well as coherent phonon processes. Although the adiabatic approximation is a standard ingredient in the *ab-initio* treatment of condensed-matter, there exist plenty of intriguing phenomena which cannot be described within the framework of the adiabatic approximation. Examples in quantum chemistry are the radiationless relaxation through a conical intersection during tunnel ionization[4], as well as photodissociation dynamics[5, 6] in strong laser pulses. Dealing with those phenomena requires calculations involving multiple BO surfaces as the non-adiabatic coupling terms are no longer negligible. In solids, novel and fascinating non-adiabatic phenomena can be observed using ultrashort and intense laser pulses. Such laser pulses can give rise to structural phase

transitions[7, 8] which happen on ultra-short time scales and, hence, are distinct from the usual temperature-driven equilibrium phase transitions. At longer time-scales, different non-adiabatic processes occur which involve the energy transfer from the electronic to the nuclear subsystem, associated with damping processes in the thermalization of solids after excitation with laser pulses[9, 10]. Other examples are magnon-phonon scattering in ultrafast spin-dynamics[11], ultrafast laser melting and order-to-disorder transitions[12–14] as well as recent developments in light-induced superconductivity[15–19], all of which live in the regime of non-adiabaticity. In order to realize and manipulate these phenomena, it is desirable to have a theoretical tool to describe non-adiabatic electron-nuclear interaction in solids.

Most of the above processes involve an electronic excitation as first step, followed by nuclear motion on a somewhat slower time scale. Aiming for a reliable theoretical description of laser-induced non-adiabatic processes, one needs both an accurate description of the initial electronic excitation and a reliable treatment of nuclear motion. For large-amplitude nuclear motion, like in laser-induced structural phase transitions, one usually invokes classical trajectories in the description, while small-amplitude nuclear motion (typically found at low temperature) is best treated in terms of phonon degrees of freedom. Part of the non-adiabatic processes can then be captured by the electron-phonon interaction. These three topics, electronic excitation, classical nuclear motion and phononic description of the nuclear degrees of freedom, form the three major sections of this thesis:

I Real-time time-dependent density functional theory (RT-TD-DFT) for the calculation of electron excitation under strong external electric fields.

II Electron dynamics in solids within a given (classical) nuclear trajectory;

III Quantum mechanical approach to non-adiabatic electron-phonon interactions.

In order to describe the laser-driven electron dynamics in solids, we apply the RT-TD-DFT approach. This easy-to-implement time-resolved method allows us to explore the electronic excitation process during and after the external influence and it enables us to deal with the nonlinear regime in a natural way. In the work on *Real time scissor correction in TD-DFT* we present a simple scheme, the so-called scissor correction, to improve the well-known underestimation of the Kohn-Sham band gap in adiabatic local density approximation (ALDA). We show that with the scissor correction, the energy after the influence of laser pulses can be significantly modified in both the linear and the nonlinear regime. This correction is particularly important in the calculation of optical spectra with real-time linear response TD-DFT. Comparing with the modified Becke-Johnson potential[20, 21] and scissor-corrected ALDA, we find that scissor-corrected ALDA produces a more accurate optical spectrum.

Next, the non-adiabatic electron-nuclear coupling is studied in a semi-classical manner in the work on *The dynamical Born effective charges*. This work discusses the calculation and properties of the linear response function of electrons in a material induced by nuclear motion. Similar to Ehrenfest dynamics which treats the

nuclei as classical particles, we propagate our systems with a given nuclear trajectory within a RT-TD-DFT approach. We extend the definition of the Born effective charge to the dynamical regime within this approach. The dynamical Born effective charge is defined as the Fourier transform of the macroscopic current divided by the Fourier transform of the velocity of a nucleus which induces the current. We find plentiful spectra with prominent resonance peaks for the selected materials in this work. Notably different from previous work on frequency-dependent Born effective charges which referred to spectra in the phonon frequency regime[22] and to the zero frequency limit[23], the dynamical Born effective charge in our work predicts interesting structures at energies above 100 eV.

Finally, in our work on *Coupled Bogoliubov equations for electrons and phonons*, we propose a fully quantum mechanical approach dealing with small amplitude nuclear motions in solids. Applying Wick's theorem to the square of the Fröhlich Hamiltonian leads to a set of two coupled Bogoliubov-type mean-field equations, one for the electrons and one for the phonon degrees of freedom. These two equations are coupled to each other through the mean-field potentials which depend on the density matrices of fermions and bosons; therefore, these equations have to be solved self-consistently alongside each other. Both the fermionic and bosonic Hamiltonian are diagonalized via a Bogoliubov transformation. These coupled Bogoliubov equations can be extended to the time-dependent case straightforwardly. The Bogoliubov equations of bosons are non-Hermitian in general, and thus the time evolution is non-unitary. This formalism allows us to explore non-adiabatic electron-phonon coupling through real-time evolution for the future applications. To show that our theory is reliable, we calculate phenomena associated to the adiabatic electron-phonon interaction (time-independent). We examine our theory through the calculations of the band gap renormalization of diamond and silicon and the superconducting gaps of niobium and MgB_2. It is a crucial step to test our theory because we should obtain the correct ground states of these systems before we extend our theory to the time-dependent regime. We find that the band gap renormalization of these insulators and the superconducting gap can be predicted with the same set of the equations. Non-trivially, the absence of the superconducting gap in copper is also verified.

2. Theoretical Background

Any physical observable of a many-body system with multiple electrons and nuclei is extremely difficult to calculate due to the enormously large number of degrees of freedom. In this section we will first discuss the adiabatic approximation which is the standard starting point of condensed matter physics and quantum chemistry. After this, we will discuss how to go beyond the adiabatic approximation. The main references for the content of this chapter are as follows: Lecture note by R. Heid[24] for section 2.2; Book by Engel and Dreizler [25] for section 2.3; Book by Carsten Ullich[26] for section 2.4; Book by D.J. Singh [27] for section 2.7.

2.1 The Adiabatic Approximation

The full Hamiltonian of a system with N_e electrons and N_n nuclei is

$$\hat{H}(\underline{\boldsymbol{r}}, \underline{\boldsymbol{R}}) = \hat{T}_e(\underline{\boldsymbol{r}}) + \hat{T}_n(\underline{\boldsymbol{R}}) + \hat{V}_{ee}(\underline{\boldsymbol{r}}) + \hat{V}_{nn}(\underline{\boldsymbol{R}}) + \hat{V}_{en}(\underline{\boldsymbol{r}}, \underline{\boldsymbol{R}}) \tag{2.1}$$

where $\underline{\boldsymbol{r}} \equiv (\boldsymbol{r}_1, \cdots, \boldsymbol{r}_{N_e})$ and $\underline{\boldsymbol{R}} \equiv (\boldsymbol{R}_1, \cdots, \boldsymbol{R}_{N_n})$ stand for the coordinates of electrons and nuclei. The corresponding kinetic and interacting terms of the full Hamiltonian are

$$\hat{T}_e(\underline{\boldsymbol{r}}) = \sum_{i=1}^{N_e} -\frac{\boldsymbol{\nabla}_i^2}{2m_e}, \qquad\qquad \hat{T}_n(\underline{\boldsymbol{R}}) = \sum_{\alpha=1}^{N_n} -\frac{\boldsymbol{\nabla}_\alpha^2}{2M_\alpha},$$

$$\hat{V}_{ee}(\underline{\boldsymbol{r}}) = \frac{1}{2} \sum_{\substack{i,j \\ i \neq j}}^{N_e} \frac{1}{|\underline{\boldsymbol{r}}_i - \underline{\boldsymbol{r}}_j|}, \qquad \hat{V}_{nn}(\underline{\boldsymbol{R}}) = \frac{1}{2} \sum_{\substack{\alpha,\beta \\ \alpha \neq \beta}}^{N_n} \frac{Z_\alpha Z_\beta}{|\underline{\boldsymbol{R}}_\alpha - \underline{\boldsymbol{R}}_\beta|} \tag{2.2}$$

$$\hat{V}_{en}(\underline{\boldsymbol{r}}, \underline{\boldsymbol{R}}) = -\sum_{i=1}^{N_e} \sum_{\alpha=1}^{N_n} \frac{Z_\alpha}{|\underline{\boldsymbol{r}}_i - \underline{\boldsymbol{R}}_\alpha|}.$$

With this Hamiltonian plus, in the most general case, a time-dependent external field $v_{\text{ext}}(\underline{\boldsymbol{r}}, \underline{\boldsymbol{R}}, t)$ (e.g. laser pulses) we have to solve the time-dependent Schrödinger equation

$$i\frac{\partial \Psi(\underline{\boldsymbol{r}}, \underline{\boldsymbol{R}}, t)}{\partial t} = \left[\hat{H}(\underline{\boldsymbol{r}}, \underline{\boldsymbol{R}}) + v_{\text{ext}}(\underline{\boldsymbol{r}}, \underline{\boldsymbol{R}}, t) \right] \Psi(\underline{\boldsymbol{r}}, \underline{\boldsymbol{R}}, t). \tag{2.3}$$

This defines the fully interacting electron-nuclear problem. A numerical solution is possible only for very few degrees of freedom. To make progress, one first addresses

the Born-Oppenheimer[1] (BO) or "clamped-nuclei" problem where in the Hamiltonian (2.1) the nuclear kinetic energy is dropped. This amounts to the infinite-nuclear-mass limit where the nuclei do not move, i.e. the nuclei are clamped at given positions, $\underline{\boldsymbol{R}}$, which enter the BO equation as parameters:

$$\left(\hat{T}_e(\underline{\boldsymbol{r}}) + \hat{V}_{ee}(\underline{\boldsymbol{r}}) + \hat{V}_{nn}(\underline{\boldsymbol{R}}) + \hat{V}_{en}(\underline{\boldsymbol{r}}, \underline{\boldsymbol{R}})\right) \psi_{\underline{\boldsymbol{R}},k}^{\mathrm{BO}}(\underline{\boldsymbol{r}}) = \mathcal{E}_k^{\mathrm{BO}}(\underline{\boldsymbol{R}})\psi_{\underline{\boldsymbol{R}},k}^{\mathrm{BO}}(\underline{\boldsymbol{r}}). \tag{2.4}$$

At each fixed $\underline{\boldsymbol{R}}$, the solution of Eq. (2.4) yields a complete set $\psi_{\underline{\boldsymbol{R}},k}^{\mathrm{BO}}(\underline{\boldsymbol{r}})$ which can be used as a basis of the electronic Hilbert space. In the next step, we use this fact to expand the full electron-nuclear wavefunction as

$$\Psi(\underline{\boldsymbol{r}}, \underline{\boldsymbol{R}}, t) = \sum_k \psi_{\underline{\boldsymbol{R}},k}^{\mathrm{BO}}(\underline{\boldsymbol{r}})\chi_k(\underline{\boldsymbol{R}}, t). \tag{2.5}$$

This is still a formally exact representation of the full wavefunction $\Psi(\underline{\boldsymbol{r}}, \underline{\boldsymbol{R}}, t)$. This expansion is also called the Born-Huang expansion[2]. Substituting Eq. (2.5) into the full Schrödinger equation leads to the following set of equations for the nuclear degrees of freedom:

$$i\frac{\partial}{\partial t}\chi_k(\underline{\boldsymbol{R}}, t) = \left[\hat{T}_n(\underline{\boldsymbol{R}}) + \mathcal{E}_k(\underline{\boldsymbol{R}})\right]\chi_k(\underline{\boldsymbol{R}}, t) + \Delta H_1 + \Delta H_2, \tag{2.6}$$

where the two additional terms ΔH_1 and ΔH_2 are given by

$$\Delta H_1 = -\sum_{k'\alpha}\frac{1}{M_\alpha}\langle\psi_{\underline{\boldsymbol{R}},k}^{\mathrm{BO}}(\underline{\boldsymbol{r}})|\nabla_{R_\alpha}|\psi_{\underline{\boldsymbol{R}},k'}^{\mathrm{BO}}(\underline{\boldsymbol{r}})\rangle\nabla_{R_\alpha}\chi_{k'}(\underline{\boldsymbol{R}}, t) \tag{2.7}$$

$$\Delta H_2 = -\sum_{k'\alpha}\frac{1}{2M_\alpha}\langle\psi_{\underline{\boldsymbol{R}},k}^{\mathrm{BO}}(\underline{\boldsymbol{r}})|\nabla_{R_\alpha}^2|\psi_{\underline{\boldsymbol{R}},k'}^{\mathrm{BO}}(\underline{\boldsymbol{r}})\rangle\chi_{k'}(\underline{\boldsymbol{R}}, t) \tag{2.8}$$

This is a set of coupled partial differential equations for the nuclear amplitudes $\chi_k(\underline{\boldsymbol{R}}, t)$. The quantities

$$\langle\psi_{\underline{\boldsymbol{R}},k}^{\mathrm{BO}}(\underline{\boldsymbol{r}})|\nabla_{R_\alpha}|\psi_{\underline{\boldsymbol{R}},k'}^{\mathrm{BO}}(\underline{\boldsymbol{r}})\rangle$$
$$\langle\psi_{\underline{\boldsymbol{R}},k}^{\mathrm{BO}}(\underline{\boldsymbol{r}})|\nabla_{R_\alpha}^2|\psi_{\underline{\boldsymbol{R}},k'}^{\mathrm{BO}}(\underline{\boldsymbol{r}})\rangle$$

are called non-adiabatic coupling (NAC) matrix of first and second order, respectively. The bracket notation indicates integration over the electronic coordinates only, so the matrix elements are functions of $(\underline{\boldsymbol{R}}, t)$. It turns out that these functions are extremely small except in the vicinity of conical intersections or narrow avoided crossings. Hence, as long as one is far from conical intersections, neglecting the NACs should be a good approximation so that we end up with the approximate equation

$$i\frac{\partial}{\partial t}\chi_k(\underline{\boldsymbol{R}}, t) = \left[\hat{T}_n(\underline{\boldsymbol{R}} + \mathcal{E}_k^{\mathrm{BO}}(\underline{\boldsymbol{R}})\right]\chi_k(\underline{\boldsymbol{R}}, t). \tag{2.9}$$

For the electron-nuclear wavefunction, this means that we approximate the infinite Born-Huang series by one single term:

$$\Psi^{\mathrm{adia}}(\underline{\boldsymbol{r}}, \underline{\boldsymbol{R}}, t) = \chi_k(\underline{\boldsymbol{R}}, t)\psi_{\underline{\boldsymbol{R}},k}^{\mathrm{BO}}(\underline{\boldsymbol{r}}) \tag{2.10}$$

if, at the initial time, only one BO state is occupied. Furthermore, Eq. (2.9) can be reduced to the stationary Schrödinger equation

$$\left(\hat{T}_n(\underline{\boldsymbol{R}}) + \mathcal{E}_k^{\mathrm{BO}}\right)\chi_k(\underline{\boldsymbol{R}}) = \xi_k\chi(\underline{\boldsymbol{R}}). \tag{2.11}$$

by setting $\chi_k(\underline{\boldsymbol{R}}, t) = e^{-i\xi_k t}\chi_k(\underline{\boldsymbol{R}})$ if the initial condition of Eq. (2.9) is the eigenfunction $\chi_k(\underline{\boldsymbol{R}})$ of Eq. (2.11). Eq. (2.11) is the basis of essentially all calculations of vibrational spectra. Usually one makes, in addition, the harmonic approximation by replacing $\mathcal{E}_k^{\mathrm{BO}}(\underline{\boldsymbol{R}})$ by its Taylor expansion around the equilibrium position $\underline{\boldsymbol{R}}_0$ to second order (see Section 2.2). Eq. (2.10) is usually called adiabatic approximation. It is relatively easy to calculate Ψ^{adia} by solving Eq. (2.11) with the BO potential energy surface (PES) obtained from Eq. (2.4). The evaluation of the BO PES for all nuclear positions $\underline{\boldsymbol{R}}$ is not possible in practice. Fortunately, the calculation of phonon spectra in harmonic approximation only requires the matrix of second derivatives of the BO PES (the so-called Hessian) at the equilibrium position $\underline{\boldsymbol{R}}_0$

$$\Phi_{i,j}(\alpha, \beta) = \left.\frac{\partial^2 \mathcal{E}^{\mathrm{BO}}(\underline{\boldsymbol{R}})}{\partial R_{i,\alpha}\partial R_{j,\beta}}\right|_{\underline{\boldsymbol{R}}_0} \tag{2.12}$$

where index i and j labels the Cartesian components of the position vectors of nuclei α and β.

2.2   Adiabatic Phonons

Section 2.1 shows that within the adiabatic approximation and by making the harmonic approximation of the PES one can straightforwardly calculate the vibrational spectrum of solids. We now write out explicitly the Taylor expansion of the PES at the equilibrium position $\underline{\boldsymbol{R}}_0$ with respect to the nuclear displacement $u_{i,\alpha}$.

$$\mathcal{E}^{\mathrm{BO}}(\underline{\boldsymbol{R}}) = \mathcal{E}^{\mathrm{BO}}(\underline{\boldsymbol{R}}_0) + \sum_{i,\alpha}\Phi_i(\alpha)u_{i,\alpha} + \frac{1}{2}\sum_{i,j,\alpha,\beta}u_{i,\alpha}\Phi_{i,j}(\alpha, \beta)u_{j,\beta} + \cdots. \tag{2.13}$$

$\Phi_i(\alpha)$ in equation (2.13) is the first-order derivative of the PES with respect to the displacement of nucleus α

$$\Phi_i(\alpha) = \left.\frac{\partial \mathcal{E}^{\mathrm{BO}}(\underline{\boldsymbol{R}})}{\partial R_{i,\alpha}}\right|_{\underline{\boldsymbol{R}}_0} \tag{2.14}$$

which is zero since we have chosen the equilibrium position $\underline{\boldsymbol{R}}_0$ as the reference coordinate for the Taylor expansion. Note that the equation above is representing a linear force applied to the atoms which can be non-zero when we apply an external field to excite the system and resulting in a non-zero displacement from the equilibrium. The second term of the expansion in equation (2.13) is the desired harmonic potential with the Hessian in Eq. (2.12). So, in harmonic approximation, the Hamiltonian reads

$$H = \sum_{i,\alpha}\frac{p_{i,\alpha}^2}{2M_\alpha} + \sum_{ij,\alpha\beta}\frac{u_{i,\alpha}\Phi_{i,j}(\alpha, \beta)u_{j,\beta}}{2}. \tag{2.15}$$

Solving the stationary Schrödinger equation with this Hamiltonian gives us the eigenvalue problem

$$M\omega^2\vec{u} = -\Phi\vec{u} \tag{2.16}$$

where M is a diagonal matrix representing the masses of the nuclei. The dimension of the matrix is $3N$, where N is the total number of atoms in a $3-$dimensional unit cell. Both Φ and M are symmetric matrices and the equation of motion above is a generalized eigenvalue problem. Since $M^{-1}\Phi$ is not a symmetric matrix unless all the masses of the nuclei are the same and noting that M is a positive definite matrix, we can thus follow the procedure of solving generalized eigenvalue problems and decompose the matrix M into the form of

$$M = UM^{\frac{1}{2}}U^\dagger UM^{\frac{1}{2}}U^\dagger, \tag{2.17}$$

where U is a $3N \times 3N$ unitary matrix. We thus have

$$M^{-\frac{1}{2}}\Phi M^{-\frac{1}{2}} = \mathcal{D} \tag{2.18}$$

and the transformed engenvectors $\vec{v}$ satisfy $\vec{u} = M^{\frac{1}{2}}\vec{v}$. The generalized eigenvalue problem can now be written as

$$\omega^2 v = \mathcal{D}v \tag{2.19}$$

where v is the transformed displacement. It can be proved by applying Rayleigh quotient that the transformed eigenvalue problem possesses the same eigenvalues as the original generalized eigenvalue problem. Here we transform the displacement $v_{i,\alpha}$ into normal coordinates with the relation

$$v_{i,\alpha} = \sum_{\lambda}^{3N} \mathcal{S}_{i,\alpha}^{\lambda} \mathcal{Q}_{\lambda} \tag{2.20}$$

where $\mathcal{S}_{i,\alpha}^{\lambda}$ is an element of the matrix $\mathcal{S}$ while $\mathcal{S}$ is a matrix that contains all the eigenvectors of the transformed eigenvalue problem and λ is the index labelling the eigenvalue and the corresponding eigenvector. The matrix $\mathcal{D}$ is the so-called dynamical matrix. So far, everything is evaluated in discrete picture and is thus also valid for the study of molecules. In solids, the index of an atom α is labelled by two indices (k, μ) where k represents the index of the unit cell and μ is the index of the individual atom in the unit cell. For a solid which has lattice periodicity, we perform a Fourier transform of the discrete atoms in the unit cell. In this way, the dynamical matrix becomes a function of the crystal momentum $\boldsymbol{q}$:

$$\mathcal{D}_{i,\mu,j,\mu'}(\boldsymbol{q}) = \frac{1}{\sqrt{M_\mu M_{\mu'}}} \sum_k \Phi_{i,j}(k, \mu, 0, \mu')e^{-\boldsymbol{q}(R_{k,\mu}^0 - R_{0,\mu'}^0)} \tag{2.21}$$

where $R_{k,\mu}^0$ representing the rest coordinate of the μ-th atom inside the k-th unit cell of the solid.

With this representation for solids, we can now rewrite the Hamiltonian in terms of the operators associated with the normal coordinates and the conjugate momenta:

$$\hat{H} = \sum_{\lambda,q} \frac{1}{2}\hat{\mathcal{P}}^{\dagger}_{\lambda,q}\hat{\mathcal{P}}_{\lambda,q} + \sum_{\lambda,q} \frac{1}{2}\omega^2_{\lambda,q}\hat{\mathcal{Q}}^{\dagger}_{\lambda,q}\hat{\mathcal{Q}}_{\lambda,q}. \tag{2.22}$$

Similarly to solving the standard harmonic oscillator problem, we can diagonalize the Hamiltonian by defining the following operators

$$\begin{aligned} \hat{d}_{\lambda,q} &= \sqrt{\frac{\omega_{\lambda,q}}{2}}\hat{\mathcal{Q}}_{\lambda,q} + i\frac{1}{\sqrt{2\omega_{\lambda,q}}}\hat{\mathcal{P}}^{\dagger}_{\lambda,q} \\ \hat{d}^{\dagger}_{\lambda,q} &= \sqrt{\frac{\omega_{\lambda,q}}{2}}\hat{\mathcal{Q}}^{\dagger}_{\lambda,q} - i\frac{1}{\sqrt{2\omega_{\lambda,q}}}\hat{\mathcal{P}}_{\lambda,q} \end{aligned} \tag{2.23}$$

and the Hamiltonian becomes

$$\hat{H} = \sum_{\lambda,q} \omega_{\lambda,q}(\hat{d}^{\dagger}_{\lambda,q}\hat{d}_{\lambda,q} + \frac{1}{2}). \tag{2.24}$$

The displacement and momentum of an atom in the solid along one direction can be calculated by performing the inverse transformation back to the original coordinates and making an inverse Fourier transform back to the discrete index. The displacement and momentum operators are then given by

$$\begin{aligned} \hat{u}_{i,\alpha} &= \frac{1}{\sqrt{N}}\sum_{\lambda,q} e^{iqR_{i,\alpha}}\frac{1}{\sqrt{2M_{\alpha}\omega_{\lambda,q}}}\mathcal{S}^{\lambda}_{i,\alpha,q}(\hat{d}_{\lambda,q} + \hat{d}^{\dagger}_{\lambda,-q}) \\ \hat{p}_{i,\alpha} &= \frac{i}{\sqrt{N}}\sum_{\lambda,q} e^{-iqR_{i,\alpha}}\sqrt{\frac{M_{\alpha}\omega_{\lambda,q}}{2}}\mathcal{S}^{\lambda}_{i,\alpha,q}(\hat{d}^{\dagger}_{\lambda,q} - \hat{d}_{\lambda,-q}). \end{aligned} \tag{2.25}$$

In the context of solid state physics, we usually focus on the observables in momentum space which can be directly evaluated by the linear combination of the creation and annihilation operators in equation (2.23).

2.3 Density Functional Theory for Many Electron Systems

It is still a difficult task to treat the many electron system even within the BO approximation. To solve the many electron problem, we still need a good approximation with acceptable accuracy and efficiency. Density functional theory (DFT) first proposed by P. Hohenberg and W. Kohn in 1964[28] has nowadays become the standard approach for dealing with many electron problems. In this section, we will briefly introduce DFT which will be the basis of the calculations done throughout this thesis.

2.3.1 The Hohenberg-Kohn Theorem and the Kohn-Sham equations

To start with, we introduce the Hohenberg-Kohn (HK) theorem which is the foundation of density functional theory. Hohenberg-Kohn theorem proves that one can represent a stationary interacting many-electron system just by the ground state densities.

Considering a non-relativistic interacting N-electron (or any fermion) Hamiltonian as follow:

$$\hat{H} = \hat{T} + \hat{V}_{\text{int}} + \hat{V}_{\text{ext}}, \tag{2.26}$$

where operator $\hat{T}$, $\hat{V}_{\text{int}}$ and $\hat{V}_{\text{ext}}$ are the kinetic energy, interacting potential and external potential operators respectively.

$$\hat{T} = -\frac{\hbar^2}{2m} \sum_{\sigma=\uparrow,\downarrow} \int d^3r \hat{\psi}^\dagger(\boldsymbol{r}\sigma) \nabla^2 \hat{\psi}(\boldsymbol{r}\sigma). \tag{2.27}$$

$\hat{V}_{\text{ext}}$ is a time-independent, local (i. e. multiplicative) potential

$$\hat{V}_{\text{ext}} = \int d^3r v_{\text{ext}}(\boldsymbol{r}) \hat{n}(\boldsymbol{r}) \tag{2.28}$$

where $\hat{n}(\boldsymbol{r})$ is the density of the particles defined as follows:

$$\hat{n}(\boldsymbol{r}) = \sum_{\sigma=\uparrow,\downarrow} \hat{\psi}^\dagger(\boldsymbol{r}\sigma) \hat{\psi}(\boldsymbol{r}\sigma). \tag{2.29}$$

The time-independent particle-particle interaction $\hat{V}_{\text{int}}$ is

$$\hat{V}_{\text{int}} = \frac{1}{2} \sum_{\sigma\sigma'} \int d^3r \int d^3r' \hat{\psi}^\dagger(\boldsymbol{r}\sigma) \hat{\psi}^\dagger(\boldsymbol{r}'\sigma') v_{\text{int}}(\boldsymbol{r},\boldsymbol{r}') \hat{\psi}(\boldsymbol{r}'\sigma') \hat{\psi}(\boldsymbol{r}\sigma). \tag{2.30}$$

The particle-particle interaction discussed in DFT is usually the Coulomb interaction. Here we do not specify what kind of the interaction $v_{\text{int}}(\boldsymbol{r},\boldsymbol{r}')$ is.

The Hohenberg-Kohn theorem states that there is a one-to-one mapping between the density determined from the electron ground state $|\psi_o\rangle$ and the external potential. This statement can be proven via a two-step proof:

I A wavefunction $\psi_0(\boldsymbol{r})$ cannot simultaneously be the ground state of two systems if the external potentials of these systems, v_{ext}^a and v_{ext}^b, differ by more than an additive constant.

II Two different ground states do not produce the same density.

Note that we restrict the system to be non-degenerate for this two-step proof. The first step can be proven via *reductio ad absurdum*. Assuming that a wave

function is simultaneously a ground state of two different external potentials v_{ext}^a and v_{ext}^b with $v_{\text{ext}}^a - v_{\text{ext}}^b \neq \text{const}$. Thus $|\psi_0\rangle$ satisfies two Schrödinger equations,

$$\hat{H}^a|\psi_o\rangle = \left[\hat{T} + \hat{V}_{\text{int}} + \hat{V}_{\text{ext}}^a\right]|\psi_0\rangle = E_0^a|\psi_0\rangle \tag{2.31}$$

$$\hat{H}^b|\psi_o\rangle = \left[\hat{T} + \hat{V}_{\text{int}} + \hat{V}_{\text{ext}}^b\right]|\psi_0\rangle = E_0^b|\psi_0\rangle \tag{2.32}$$

Subtracting equation (2.32) from (2.31) we have

$$\left[\hat{H}^a - \hat{H}^b\right]|\psi_0\rangle = \left[\hat{V}_{\text{ext}}^a - \hat{V}_{\text{ext}}^b\right]|\psi_0\rangle = \left[E_0^a - E_0^b\right]|\psi_0\rangle. \tag{2.33}$$

Since the external potentials are multiplicative, one can divide equation (2.33) by $|\psi_0\rangle$ and find the relation

$$\sum_i^N \left(v_{\text{ext}}^a(\boldsymbol{r}_i) - v_{\text{ext}}^b(\boldsymbol{r}_i)\right) = E_0^a - E_0^b. \tag{2.34}$$

This shows that the wave function can only be the ground state eigenfunction simultaneously of two external potentials if the difference between the external potentials is a constant, in contradiction to the original assumption.

For the second step, we have to prove that the ground states of arbitrary systems never lead to the same density. We first assume that a ground state density n_0 comes from two different ground states $|\psi_0^a\rangle$ and $|\psi_0^b\rangle$ which are the corresponding ground states of two Hamiltonians $\hat{H}^a$ and $\hat{H}^b$. From the Ritz variational principle, we can find

$$E_0^a = \langle\psi_0^a|\hat{H}^a|\psi_0^a\rangle < \langle\psi_0^b|\hat{H}^a|\psi_0^b\rangle. \tag{2.35}$$

Using $\hat{H}^a = \hat{H}^b + \hat{V}_{\text{ext}}^a - \hat{V}_{\text{ext}}^b$, we find

$$E_0^a < E_0^b + \langle\psi_0^b|\hat{V}_{\text{ext}}^a - \hat{V}_{\text{ext}}^b|\psi_0^b\rangle \tag{2.36}$$

or, equivalently,

$$E_0^a < E_0^b + \int d^3r n_0(\boldsymbol{r})(v_{\text{ext}}^a(\boldsymbol{r}) - v_{\text{ext}}^b(\boldsymbol{r})). \tag{2.37}$$

However, we can simply exchange the indices a and b and find by the same argument

$$E_0^b < E_0^a + \int d^3r n_0(\boldsymbol{r})(v_{\text{ext}}^b(\boldsymbol{r}) - v_{\text{ext}}^a(\boldsymbol{r})). \tag{2.38}$$

Adding Eq (2.37) and Eq. (2.38) leads to the contradiction

$$E_0^a + E_0^b < E_0^b + E_0^a \tag{2.39}$$

In the above proof we take advantage of the assumption of non-degeneracy. It can be proven that the HK theorem can be extended to degenerate systems[29] as well.

The external potentials in the proof above are local potentials. The proof of the second step for nonlocal external potentials was later given by Gilbert[30] in 1975. In his proof, it states that there exists a one-to-one correspondence between the

density matrices and the wave functions. However, the first part of the HK theorem for nonlocal potentials is not true in general, as can be shown by counter examples.

So far, the HK theorem has not shown any advantage for solving many-electron problems. The power of DFT only showed up when the Kohn-Sham (KS) equations were introduced in 1965[31]. KS equations represent the complex interacting Hamiltonian into the non-interacting fashion which gives great advantage in calculating real materials. The KS equations describe an auxiliary system which reproduces the density of the corresponding interacting many-electron systems and, with the knowledge of HK theorem, every physical observable can be described by the density of the system. The KS equation is given by

$$\left[-\frac{\nabla^2}{2} + v_{\mathrm{s}}(\boldsymbol{r}) \right] \psi_i(\boldsymbol{r}) = \epsilon_i \psi_i(\boldsymbol{r}), \tag{2.40}$$

where the single particle eigenstates $\psi_i(\boldsymbol{r})$ are the so-called KS orbitals. The ground state density of the KS system is then

$$n_{\mathrm{s}}(\boldsymbol{r}) = \sum_{i=1}^{N} |\psi_i(\boldsymbol{r})|^2 \tag{2.41}$$

which is the same density as the density of the interacting systems at hand. We can thus use this density obtained from this auxiliary non-interacting system to evaluate the observables of interest:

$$\langle \hat{O} \rangle = \langle \Psi[n_{\mathrm{s}}] | \hat{O} | \Psi[n_{\mathrm{s}}] \rangle \tag{2.42}$$

Furthermore we define the exchange-correlation(XC) energy functional by

$$E_{\mathrm{xc}}[n] = F_{\mathrm{HK}}[n] - \frac{1}{2} \int \int d^3 r d^3 r' n(\boldsymbol{r}) v_{\mathrm{int}}(\boldsymbol{r}, \boldsymbol{r}') n(\boldsymbol{r}') - T_{\mathrm{s}}[n], \tag{2.43}$$

where $T_{\mathrm{s}}[n]$ is the kinetic energy of non-interacting particles, and $F_{\mathrm{HK}}[n]$ is a universal functional related to the total energy $E[n]$ by:

$$E[n] = F_{\mathrm{HK}}[n] + \int d^3 r v_{\mathrm{ext}}(\boldsymbol{r}) n(\boldsymbol{r}). \tag{2.44}$$

Using the variational principle,

$$\frac{\delta E[n]}{\delta n(\boldsymbol{r})} \Big|_{n_0} = 0, \tag{2.45}$$

and taking the functional derivative of equation (2.43) with respect to the density we arrive at

$$v_{\mathrm{s}}(\boldsymbol{r}) = v_{\mathrm{ext}}(\boldsymbol{r}) + \int d^3 r' v_{\mathrm{int}}(\boldsymbol{r}, \boldsymbol{r}') n_0(\boldsymbol{r}) + v_{\mathrm{xc}}[n_0](\boldsymbol{r}), \tag{2.46}$$

where $n_0(\boldsymbol{r})$ is the ground state density. The exchange-correlation potential is thus given by

$$v_{\mathrm{xc}}[n_0](\boldsymbol{r}) = \frac{\delta E_{\mathrm{xc}}}{\delta n(\boldsymbol{r})}\Big|_{n_0}. \tag{2.47}$$

Since v_{s} depends on the density which can be evaluated by solving equation (2.40), we have to solve the KS system self-consistently. The biggest advantage of solving KS equation is that the kinetic energy $T_{\mathrm{s}}[n]$ is now determined from non-interacting Kohn-Sham orbitals instead of many-body wavefunctions. The remaining part of the exact kinetic energy is included in the exchange-correlation energy $E_{\mathrm{xc}}[n]$. How to find a good approximation for a XC functional is a main topic in DFT.

2.3.2 Exchange-correlation Functional

The only approximation needed to use the KS equations in practice is for the exchange-correlation functional. The approximated XC functionals used in this work are briefly introduced in this section.

Local Density Approximation
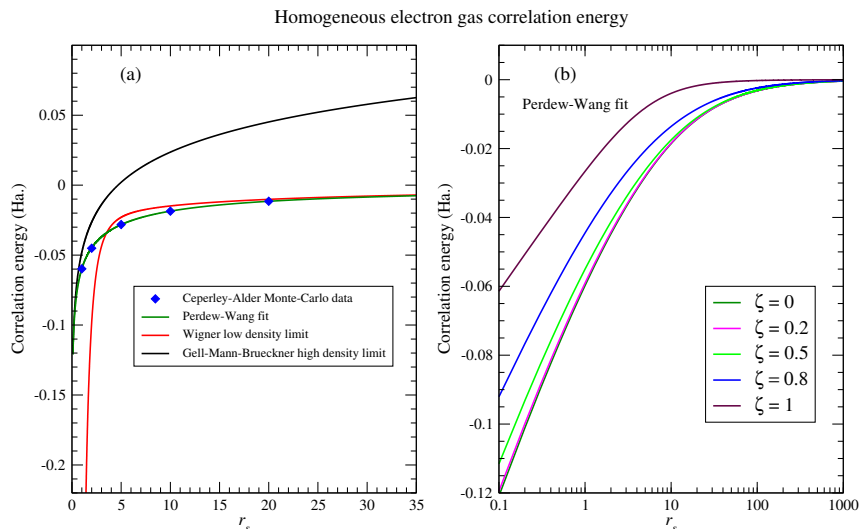
Figure 2.1
The correlation energy of (a) the non-spin polarized homogeneous electron gas as a function of the Wigner-Seitz radius r_{s} and (b) the spin-polarized correlation energy of a homogeneous electron gas of the Perdew-Wang fit. ζ is the relative spin polarization given by $\zeta = \frac{n_\uparrow - n_\downarrow}{n_\uparrow + n_\downarrow}$.

The local density approximation (LDA) was the very first XC functional in the history of DFT. The exchange-correlation energy functional of LDA is given by

$$E_{\mathrm{xc}}^{\mathrm{LDA}}[n] = \int d^3 r \epsilon_{\mathrm{xc}}^{\mathrm{hom}}\left(n(\boldsymbol{r})\right) n(\boldsymbol{r}), \tag{2.48}$$

where $\epsilon_{\mathrm{xc}}^{\mathrm{hom}}(n(\boldsymbol{r}))$ is the XC energy density of the homogeneous electron gas (HEG). The exchange and correlation parts can be written down separately as

$$\epsilon_{\mathrm{xc}}^{\mathrm{hom}}(n(\boldsymbol{r})) = \epsilon_{\mathrm{x}}^{\mathrm{hom}}(n(\boldsymbol{r})) + \epsilon_{\mathrm{c}}^{\mathrm{hom}}(n(\boldsymbol{r})). \tag{2.49}$$

The exchange energy density of the unpolarized HEG of density $n = 3/\left(4\pi r_{\mathrm{s}}^3\right)$ is

$$\epsilon_{\mathrm{x}}^{\mathrm{hom}}(n) = -\frac{c}{r_{\mathrm{s}}}, \; c = \frac{3}{4\pi}\left(\frac{9\pi}{4}\right)^{\frac{1}{3}}, \tag{2.50}$$

where r_{s} is the Wigner-Seitz radius and a_{B} is the Bohr radius. The correlation energy of a HEG is usually evaluated by Monte-Carlo calculation. Presented in Fig. 2.1(a), the analytic representation of the correlation energy for the HEG of the Perdew-Wang (PW) fit[32] matches the Monte-Carlo data by Ceperley and Alder[33] and goes smoothly toward the Wigner low density limit[34] and the Gell-Mann-Brueckner high density limit[35]. In the case of a spin-polarized HEG, Fig. 2.1(b) shows that, the correlation energy of a spin-polarized HEG is determined through the spin-scaling relationship[32] within the Perdew-Wang fit. This simple functional is surprisingly successful for various systems and is still a convenient functional of choice today.

Generalized Gradient Approximation

The generalized gradient approximation (GGA) introduces the gradient of the charge density into the XC energy functional thereby making the functional dependence on the density (slightly) nonlocal. One of the most popular GGA functionals is the so called PBE functional proposed by Perdew, Burke and Ernzerhof in 1996[36]. This functional is constructed to satisfy the following conditions:

(i) In the slowly varying density gradient limit, the gradient contribution in the correlation functional is given by its second-order gradient expansion.

(ii) In the rapid varying density gradient limit, the correlation energy has to be zero.

(iii) Under uniform scaling to the high density limit, the correlation energy has to scale to a constant.

(iv) It correctly reduces to local spin density (LSD) approximation for uniform electron densities.

(v) It recovers the LSD linear response for small-amplitude density variations around the uniform density.

(vi) The Lieb-Oxford bound is satisfied.

GGA functionals have seen several successes such as better atomization energies of molecules and more precise lattice constants of alkali metals. More details of the success stories can be found in reference[37].

Modified Becke-Johnson Potential

The modified Becke-Johnson (mBJ) exchange potential[21, 38] is a type of meta-GGA functional which improves the accuracy of band gaps to a similar level as the hybrid functionals or the GW methods with the advantage of lower computational cost. The mBJ exchange potential is given by

$$v_{\text{x},\sigma}^{\text{MBJ}}(\boldsymbol{r}) = c v_{\text{x},\sigma}^{BR}(\boldsymbol{r}) + (3c - 2)\frac{1}{\pi}\sqrt{\frac{5}{12}}\sqrt{\frac{2\tau_\sigma(\boldsymbol{r})}{n_\sigma(\boldsymbol{r})}}, \tag{2.51}$$

where $\tau_\sigma(\boldsymbol{r})$ is the non-interacting kinetic energy density defined by

$$\tau_\sigma(\boldsymbol{r}) = \frac{1}{2}\sum_{i,\sigma}^{N_{el}} \nabla\psi_{i,\sigma}^*(\boldsymbol{r})\cdot\nabla\psi_{i,\sigma}(\boldsymbol{r}) \tag{2.52}$$

and

$$v_{\text{x},\sigma}^{\text{BR}}(\boldsymbol{r}) = -\frac{1}{b_\sigma(\boldsymbol{r})}\left(1 - e^{-x_\sigma(\boldsymbol{r})} - \frac{1}{2}x_\sigma(\boldsymbol{r})e^{-x_\sigma(\boldsymbol{r})}\right) \tag{2.53}$$

is the Becke-Roussel exchange potential[20] which was introduced for modelling the Coulomb potential created by the exchange hole. The function $x_\sigma(\boldsymbol{r})$ in equation (2.53) is determined by n_σ, ∇n_σ, $\nabla^2 n_\sigma$ and τ_σ:

$$\frac{x_\sigma(\boldsymbol{r})e^{-x_\sigma(\boldsymbol{r})/3}}{x_\sigma(\boldsymbol{r}) - 2} = \frac{2}{3}\pi^{2/3}\frac{n_\sigma^{5/3}(\boldsymbol{r})}{Q_\sigma(\boldsymbol{r})} \tag{2.54}$$

where

$$Q_\sigma(\boldsymbol{r}) = \frac{1}{6}(\nabla^2 n_\sigma(\boldsymbol{r}) - 2\gamma D_\sigma(\boldsymbol{r})) \tag{2.55}$$

and

$$D_\sigma(\boldsymbol{r}) = \tau_\sigma(\boldsymbol{r}) - \frac{1}{4}\frac{(\nabla n_\sigma(\boldsymbol{r}))^2}{n_\sigma(\boldsymbol{r})}. \tag{2.56}$$

The parameter γ in Eq. (2.55) should be taken to be 1 in principle. However, as demonstrated in Ref.[20], it was shown that the exchange potential of the HEG can be recovered by choosing $\gamma = 0.8$. b_σ is then given by

$$b_\sigma(\boldsymbol{r}) = \left[x_\sigma^3(\boldsymbol{r})e^{-x_\sigma(\boldsymbol{r})}/(8\pi n_\sigma(\boldsymbol{r}))\right]^{\frac{1}{3}} \tag{2.57}$$

The coefficient c is determined by

$$c = \alpha + \beta\left(\frac{1}{V_{\text{cell}}}\int_{V_{\text{cell}}}d^3r'\frac{|\nabla n(\boldsymbol{r}')|}{n(\boldsymbol{r}')}\right)^{\frac{1}{2}}, \tag{2.58}$$

where α and β are free parameters and V_{cell} is the unit cell volume. The values of the two free parameters are $\alpha = -0.012$ and $\beta = 1.023$ bohr$^{1/2}$ in accordance with the minimization of the mean absolute value error for the experimental band gap of solids[38]. The correlation potential implemented together with the mBJ exchange potential is the LDA correlation potential.

2.3.3 Superconducting DFT

Superconducting DFT (SC-DFT) was first introduced by Oliveira, Gross and Kohn in 1988[39] as a generalization of finite temperature DFT including the anomalous density that couples with a pairing potential. Their formalism leads to Kohn-Sham type and formally exact self-consistent Bogoliubov-de Gennes equations for inhomogeneous superconductors.

The Hamiltonian of SC-DFT is in fact the Hamiltonian of interacting electrons and nuclei as depicted in equation (2.1). In addition one includes an external pairing potential that is crucial for the phase symmetry breaking. As described both in BCS and Eliashberg theory, this potential can be written as

$$\hat{V}_{\Delta ext} = \int d\boldsymbol{r}d\boldsymbol{r}'\Delta_{\text{ext}}^*(\boldsymbol{r},\boldsymbol{r}')\hat{\psi}_\uparrow(\boldsymbol{r})\hat{\psi}_\downarrow(\boldsymbol{r}') + h.c., \tag{2.59}$$

where $\hat{\psi}_\uparrow^\dagger(\boldsymbol{r})\hat{\psi}_\downarrow^\dagger(\boldsymbol{r}') \equiv \hat{\chi}(\boldsymbol{r},\boldsymbol{r}')$ is the superconducting order parameter. Here and throughout this thesis, the order parameter is a spin singlet. Δ_{ext} can be viewed as the proximity-induced pairing field of a superconductor adjacent to the system of interest. If the adjacent superconductor is absent, we set $\Delta_{\text{ext}} = 0$.

The HK theorem at finite temperature was proved by Mermin [40] at 1965. In SC-DFT, the statements are generalized for the additional anomalous and nuclear densities. In order to make the SC-DFT useful, one must cast SC-DFT in a KS-like scheme. The KS potentials of SC-DFT are

$$v_{\text{s}}(\boldsymbol{r}) = v_{\text{xc}}(\boldsymbol{r}) + v_{\text{H}}(\boldsymbol{r}) + v_{\text{ext}}(\boldsymbol{r}) \tag{2.60}$$

$$\Delta_{\text{s}}(\boldsymbol{r},\boldsymbol{r}') = \Delta_{\text{xc}}(\boldsymbol{r},\boldsymbol{r}') + \Delta_{\text{ext}}(\boldsymbol{r},\boldsymbol{r}') \tag{2.61}$$

$$w_{\text{s}}(\underline{\boldsymbol{R}}) = w_{\text{xc}}(\underline{\boldsymbol{R}}) + w_{\text{H}}(\underline{\boldsymbol{R}}) + w_{\text{ext}}(\underline{\boldsymbol{R}}). \tag{2.62}$$

The XC potentials can be evaluated via the functional derivative of the exchange-correlation free-energy functional $F_{\text{xc}}[n,\chi,\Gamma]$ which includes the nuclear N_n-body density Γ, the normal electronic density n and the anomalous density χ. The electronic KS Hamiltonian is then given by

$$H_{\text{s}} = \sum_\sigma \int d\boldsymbol{r}\psi_\sigma^\dagger(\boldsymbol{r})\left[\frac{-\nabla^2}{2} + v_{\text{s}} - \mu\right]\psi_\sigma(\boldsymbol{r}) + \int d\boldsymbol{r}d\boldsymbol{r}'\left[\Delta_s^*(\boldsymbol{r},\boldsymbol{r}')\psi_\uparrow(\boldsymbol{r})\psi_\downarrow(\boldsymbol{r}' + h.c.)\right]. \tag{2.63}$$

This Hamiltonian can be diagonalized via a Bogoliubov-Valatin transformation leading to the Kohn-Sham Bogoliubov-deGennes equations:

$$\begin{cases} \left[-\frac{\nabla^2}{2} + v_{\text{s}}(\boldsymbol{r}) - \mu\right]u_i(\boldsymbol{r}) + \int \Delta_{\text{s}}(\boldsymbol{r},\boldsymbol{r}')v_i(\boldsymbol{r}')d\boldsymbol{r}' = \varepsilon_i u_i(\boldsymbol{r}) \\ \\ -\left[-\frac{\nabla^2}{2} + v_{\text{s}} - \mu\right]v_i(\boldsymbol{r}) + \int \Delta_{\text{s}}^*(\boldsymbol{r},\boldsymbol{r}')u_i(\boldsymbol{r}')d\boldsymbol{r}' = \varepsilon_i v_i(\boldsymbol{r}). \end{cases} \tag{2.64}$$

The nuclear Kohn-Sham equation is an N_n-body Schrödinger equation

$$\left[T_n(\underline{\boldsymbol{R}}) + w_{\text{s}}(\underline{\boldsymbol{R}})\right]X(\underline{\boldsymbol{R}}) = \xi X(\underline{\boldsymbol{R}}) \tag{2.65}$$

similar to the BO equation (2.11) but the N_n-body interaction, w_{s} is such that the wavefunction $X(\underline{\boldsymbol{R}})$ reproduces the true nuclear N_n-body density $\Gamma(\underline{\boldsymbol{R}})$. For normal-conducting systems, the order parameters vanishes and equation (2.64) returns to ordinary but more general DFT KS equations because the exchange-correlation free energy functional is a functional of electron and nuclear densities,$F_{\mathrm{xc}}[n, \Gamma]$, and hence includes the effect of temperature and motion of nuclei.

The last step is to find the XC functional for SC-DFT. Marques[41] extended the Sham Schlüter equation to SC-DFT which connects the Eliashberg theory to SC-DFT. With this connection, one can construct a KS pairing potential of SC-DFT from any many-body self energy because, by construction of the KS system, the superconducting order parameter is the same as the order parameter of the interacting Hamiltonian.

2.4 Time-dependent Density Functional Theory

The density functional formalism discussed so far is aimed to determine the ground-state or thermal-equilibrium properties of interacting electrons. In order to investigate the dynamics of interacting systems under the influence of time-dependent external fields, i.e. electric fields and magnetic fields or laser pulses, one must solve the time-dependent many-body Schrödinger equation which is extremely difficult in practice. Time-dependent density functional theory is developed to tackle time-dependent systems with similar improvement on the computational efficiency as ordinary density functional theory.

2.4.1 Runge-Gross Theorem

Like the Hohenberg-Kohn theorem in DFT, the Runge-Gross (RG) theorem[42] is the basis of time-dependent density functional theory. The Runge-Gross theorem states that there exists a one-to-one mapping between a time-dependent external potential $v_{\mathrm{ext}}(\boldsymbol{r}, t)$ and the time-dependent density $n(\boldsymbol{r}, t) = \langle \psi(t) | \hat{n}(\boldsymbol{r}) | \psi(t) \rangle$. In their paper published in 1984, Runge and Gross proved that for two densities $n_a(\boldsymbol{r}, t)$ and $n_b(\boldsymbol{r}, t)$ evolved from the same initial state $|\psi_0\rangle$ under the influence of two external potentials that the densities become different shortly after the initial time if the difference between the potentials is more than a pure scalar time-dependent function. Two potentials differing by an additive time-dependent scalar function are considered the same (to be precise, they are elements of the same gauge class) because the corresponding wavefunctions only differ by a time-dependent phase factor leading to the same time-dependent densities.

The RG theorem provides the basis of TD-DFT. However, just like DFT, the theory only becomes useful when one calculates the interacting system via an auxiliary non-interacting system which reproduces the density of the interacting system. The Van Leeuwen theorem[43] shows that one can indeed do so with some restrictions. The statement of the Van Leeuwen theorem is as follows: For a many-body sys-

tem with a given external potential $v_{\text{ext}}(\boldsymbol{r}, t)$, particle-particle interaction $v_{\text{int}}(\boldsymbol{r}, \boldsymbol{r}')$ and initial state $|\psi_0\rangle$, one can find a different many-body system with interaction $v'_{\text{int}}(\boldsymbol{r}, \boldsymbol{r}')$ and a unique external potential $v'_{\text{ext}}(\boldsymbol{r}, t)$ which reproduce the same time-dependent density $n(\boldsymbol{r}, t)$ as the original many-body Hamiltonian with the requirement of that the initial state of this system $|\psi'_0\rangle$ must be chosen to reproduce the given density and its time derivative at the initial time.

With the van Leeuwen theorem, one can solve the interacting many-body problem in an auxiliary non-interacting system which yields the same density as the interacting one. In TD-DFT, this is done via the time-dependent Kohn-Sham equation

$$i\frac{\partial}{\partial t}|\psi_i(\boldsymbol{r}, t)\rangle = \left\{-\frac{\nabla^2}{2} + v_{\text{s}}(\boldsymbol{r}, t)\right\}|\psi_i(\boldsymbol{r}, t)\rangle \qquad (2.66)$$

which evolves with the effective potential

$$v_{\text{s}}(\boldsymbol{r}, t) \equiv v_{\text{s}}[n, \Psi_0, \Phi_0](\boldsymbol{r}, t) \qquad (2.67)$$

where $|\Psi_0\rangle$ and $|\Phi_0\rangle$ are the initial states of the interacting system and the non-interacting system respectively. The RG theorem guarantees the uniqueness of v_{s} while the Van Leeuwen theorem insures its existence. It is worth to mention that such existence of the effective potential can only be insured in TD-DFT (not in the ground-state DFT) because of the Sturm-Liouville type equations with the given boundary condition in the Van Leeuwen theorem[43]. The TD-KS equations are similar in spirit to static DFT, while the KS orbitals $\psi_i(\boldsymbol{r}, t)$ are now time-dependent explicitly. The time-dependent density is simply

$$n(\boldsymbol{r}, t) = \sum_{i=1}^{N} |\psi_i(\boldsymbol{r}, t)|^2. \qquad (2.68)$$

The initial condition for Eq. (2.66) is $\psi_i(\boldsymbol{r}, t = 0) = \psi_i^0(\boldsymbol{r})$ where $\psi_i^0(\boldsymbol{r})$ are the initially occupied KS orbitals calculated from GS DFT and the static XC potential applied to evaluate the initial ground state has to match with the time-dependent XC potential at the initial time. The effective potential is given by

$$v_{\text{s}}(\boldsymbol{r}, t) = v_{\text{ext}}(\boldsymbol{r}, t) + \int d^3r' \frac{n(\boldsymbol{r}', t)}{|\boldsymbol{r} - \boldsymbol{r}'|} + v_{\text{xc}}(\boldsymbol{r}, t) \qquad (2.69)$$

and all we need is to find an approximate functional for the XC potential in the TD-KS equations.

The approximation usually adopted for the XC functional of TD-DFT is the adiabatic approximation. In the adiabatic approximation, one simply uses the static XC potential of DFT and makes it time-dependent explicitly by inserting the time-dependent density $n(\boldsymbol{r}, t)$ as in equation (2.68). For a given time t, the XC potential with adiabatic approximation is

$$v_{\text{xc}}^{\text{A}}(\boldsymbol{r}, t) = v_{\text{xc}}^0[\underline{n}](\boldsymbol{r})\Big|_{\underline{n}(\boldsymbol{r}) \to n(\boldsymbol{r}, t)}. \qquad (2.70)$$

The basic assumption in the adiabatic approximation is that the external perturbation acting on a physical system is slow enough so that system is able to keep its instantaneous ground-state. Though most of the studies of time-dependent systems are non-adiabatic, the adiabatic approximation for XC potential works very well in practice.

2.4.2 Linear Response Theory

Suppose that we have a weak time-dependent external potential $v_{\text{ext}}(\boldsymbol{r}, t)$ and that the change of the electron density with respect to the external potential is in linear regime. We write the density at time t as $n(\boldsymbol{r}, t)$ and the density of the initial ground state is $n_0(\boldsymbol{r})$. The difference of the charge density up to linear order induced by the external potential $n'(\boldsymbol{r}, t) = n(\boldsymbol{r}, t) - n_0(\boldsymbol{r})$ is obtained from the density response function $\chi(\boldsymbol{r}, \boldsymbol{r}', t - t')$ with the following relation:

$$n'(\boldsymbol{r}, t) = \int_{-\infty}^{\infty} dt' \int d\boldsymbol{r}' \chi(\boldsymbol{r}, \boldsymbol{r}', t - t') v_{\text{ext}}(\boldsymbol{r}', t'). \tag{2.71}$$

The density-density response function of a time-independent many-body Hamiltonian can be written as

$$\chi(\boldsymbol{r}, \boldsymbol{r}', t - t') = -i\theta(t - t') \langle \psi_0 | \left[\hat{n}(\boldsymbol{r}, t), \hat{n}(\boldsymbol{r}', t') \right] | \psi_0 \rangle \tag{2.72}$$

where $|\psi_0\rangle$ is the ground state wave function of the unperturbed time-independent Hamiltonian H and the time-dependent density operator $\hat{n}(\boldsymbol{r}, t)$ is defined as

$$\hat{n}(\boldsymbol{r}, t) = e^{iHt} \hat{n}(\boldsymbol{r}) e^{-iHt} \tag{2.73}$$

with the ordinary density operator $\hat{n}(\boldsymbol{r})$ defined in equation (2.29).

Instead of representing the linear response function in real-time, it is actually much more common to work in frequency space. The density-density response function in frequency representation is simply the Fourier transform of equation (2.72). The explicit expression of the frequency dependent density-density response function is

$$\chi(\boldsymbol{r}, \boldsymbol{r}', \omega) = \lim_{\eta \to 0^+} \sum_j \frac{\langle \psi_0 | \hat{n}(\boldsymbol{r}) | \psi_j \rangle \langle \psi_j | \hat{n}(\boldsymbol{r}') | \psi_0 \rangle}{\omega - (\varepsilon_j - \varepsilon_0) + i\eta} - \frac{\langle \psi_0 | \hat{n}(\boldsymbol{r}') | \psi_j \rangle \langle \psi_j | \hat{n}(\boldsymbol{r}) | \psi_0 \rangle}{\omega + (\varepsilon_j - \varepsilon_0) + i\eta} \tag{2.74}$$

where the index j runs over all possible states of the unperturbed Hamiltonian and ε_i is the eigen-energy and the corresponding eigenstate of the unperturbed Hamiltonian satisfying $\hat{H}|\psi_j\rangle = \varepsilon_j |\psi_j\rangle$. Here are some properties of the linear response function of equation (2.74). We can separate the response function into real part $\chi'(\boldsymbol{r}, \boldsymbol{r}', \omega)$ and imaginary part $\chi''(\boldsymbol{r}, \boldsymbol{r}', \omega)$. For imaginary part, we can write it as

$$\chi''(\boldsymbol{r}, \boldsymbol{r}', \omega) = -\frac{i}{2} \int_{-\infty}^{\infty} dt e^{i\omega t} \left[\chi(\boldsymbol{r}, \boldsymbol{r}', t) - \chi(\boldsymbol{r}, \boldsymbol{r}', -t) \right]. \tag{2.75}$$

We immediately find that the imaginary part is an odd function of ω and it is corresponding to the part of the response function which is not time reversal invariant thus it must be account for dissipative or absorption processes. In practice, the imaginary part is indeed the spectral function that can be experimentally measured such as optical absorption spectra. We also rewrite the real part of the linear response function as

$$\chi'(\boldsymbol{r}, \boldsymbol{r}', \omega) = \frac{1}{2} \int_{-\infty}^{\infty} dt e^{i\omega t} \left[\chi(\boldsymbol{r}, \boldsymbol{r}', t) + \chi(\boldsymbol{r}, \boldsymbol{r}', -t)\right] \tag{2.76}$$

and find the real part is an even function of ω and the corresponding part of the response function $\chi(\boldsymbol{r}, \boldsymbol{r}', t)$ obeys time reversal symmetry. The poles in equation (2.74) show that $\chi(\boldsymbol{r}, \boldsymbol{r}', \omega)$ is analytic in the upper-half of the complex plane. It is because of the causality that is represented by the heaviside step function in equation (2.72). The frequency dependent density response is simply given by

$$n'(\boldsymbol{r}, \omega) = \int d\boldsymbol{r}' \chi(\boldsymbol{r}, \boldsymbol{r}', \omega) v_{\text{ext}}(\boldsymbol{r}', \omega). \tag{2.77}$$

From the time-dependent Schrödinger equation, it follows that the density is a functional of the external potential

$$n(\boldsymbol{r}, t) = n[v_{\text{ext}}](\boldsymbol{r}, t). \tag{2.78}$$

The same is true for non-interacting particles. The non-interacting density is a functional of the potential $v_{\text{s}}(\boldsymbol{r}, t)$ appearing in the one-body Schrödinger equation of non-interacting particles:

$$n_{\text{s}}(\boldsymbol{r}, t) = n[v_{\text{s}}](\boldsymbol{r}, t). \tag{2.79}$$

Accordingly, the linear density response of non-interacting particles is given by

$$n'_{\text{s}}(\boldsymbol{r}, t) = \int dt' \int d\boldsymbol{r}' \chi_{\text{s}}(\boldsymbol{r}, \boldsymbol{r}', t, t') v'_{\text{s}}(\boldsymbol{r}', t'), \tag{2.80}$$

where the density-density response function χ_{s} of non-interacting particles is the functional derivative:

$$\chi_{\text{s}}(\boldsymbol{r}, \boldsymbol{r}', t, t') = \left. \frac{\delta n[v_{\text{s}}](\boldsymbol{r}, t)}{\delta v_{\text{s}}(\boldsymbol{r}', t')} \right|_{v_{\text{s}}[n_0]}. \tag{2.81}$$

By virtue of the RG theorem, the TD-KS density reproduces the density of interacting systems. Therefore equation (2.80) reproduces the density response (2.71) of the interacting system if v'_{s} on the right hand side of Eq. (2.80) is the linearized TD-KS potential given by:

$$v'_{\text{s}}(\boldsymbol{r}, t) = v_{\text{ext}}(\boldsymbol{r}, t) + \int d^3 r' \frac{n'(\boldsymbol{r}', t)}{|\boldsymbol{r} - \boldsymbol{r}'|} + v'_{\text{xc}}(\boldsymbol{r}, t). \tag{2.82}$$

The last term of equation (2.82) is the linearised exchange-correlation potential which can be evaluated again by functional Taylor expansion with respect to the time-dependent density:

$$v'_{\text{xc}}(\boldsymbol{r}, t) = \int dt' \int d^3 r' \left. \frac{\delta v_{\text{xc}}[n](\boldsymbol{r}, t)}{\delta n(\boldsymbol{r}', t')} \right|_{n_0} n'(\boldsymbol{r}', t'). \tag{2.83}$$

The functional derivative of XC potential in equation (2.83) is the so-called time-dependent exchange correlation kernel,

$$f_{\text{xc}}(\boldsymbol{r}, t, \boldsymbol{r}', t') = \left. \frac{\delta v_{\text{xc}}[n](\boldsymbol{r}, t)}{\delta n(\boldsymbol{r}', t')} \right|_{n_0}, \tag{2.84}$$

which is the crucial object in the linear response theory of TD-DFT. With the functional derivative of the KS potential, the potential has included the dynamical screening with the electron density. Plugging equation (2.82) into equation (2.80), we arrive at the linear density response equation of TD-DFT:

$$\begin{aligned} n'(\boldsymbol{r}, t) = \int dt' \int dr'^3 \chi_{\text{s}}(\boldsymbol{r}, t, \boldsymbol{r}', t') &\bigg\{ v_{\text{ext}}(\boldsymbol{r}', t') \\ &+ \int dt'' \int dr''^3 \left[\frac{\delta(t' - t'')}{|\boldsymbol{r}' - \boldsymbol{r}''|} + f_{\text{xc}}(\boldsymbol{r}', t', \boldsymbol{r}'', t'') \right] n'(\boldsymbol{r}'', t'') \bigg\}. \end{aligned} \tag{2.85}$$

Equation (2.85) has to be solved self-consistently because the charge density n' appears on both sides of Eq. (2.85). Up to now, we have introduced the non-interacting linear response function χ_{s}. By inserting Eq. (2.71) into equation (2.85), we arrive at the so-called Dyson-like equation which connects the interacting and non-interacting response functions:

$$\begin{aligned} \chi(\boldsymbol{r}, t, \boldsymbol{r}', t') = \chi_{\text{s}}(\boldsymbol{r}, t, \boldsymbol{r}', t') \\ + \int d\underline{t} \int d^3 \underline{r} \int d\underline{t}' \int d^3 \underline{r}' \chi_{\text{s}}(\boldsymbol{r}, t, \underline{\boldsymbol{r}}, \underline{t}) \left[\frac{\delta(\underline{t} - \underline{t}')}{|\underline{\boldsymbol{r}} - \underline{\boldsymbol{r}}'|} + f_{\text{xc}}(\underline{\boldsymbol{r}}, \underline{t}, \underline{\boldsymbol{r}}', \underline{t}') \right] \chi(\underline{\boldsymbol{r}}', \underline{t}', \boldsymbol{r}', t'). \end{aligned} \tag{2.86}$$

We again convert the representation of the TD-DFT response function to frequency space by Fourier transform since both of the interacting and non-interacting response function only depend on the difference of time. The linear density response in frequency space is simply

$$n'(\boldsymbol{r}, \omega) = \int d^3 r' \chi_{\text{s}}(\boldsymbol{r}, \boldsymbol{r}', \omega) \left\{ v_{\text{ext}}(\boldsymbol{r}', \omega) + \int d^3 \underline{r} \left[\frac{1}{|\boldsymbol{r}' - \underline{\boldsymbol{r}}|} + f_{\text{xc}}(\boldsymbol{r}', \underline{\boldsymbol{r}}, \omega) \right] n'(\underline{\boldsymbol{r}}, \omega) \right\} \tag{2.87}$$

and the frequency-dependent KS response function is given by

$$\chi_{\text{s}}(\boldsymbol{r}, \boldsymbol{r}', \omega) = \lim_{\eta \to 0} \sum_{j,k=1}^{\infty} (n_k - n_j) \frac{\varphi_j(\boldsymbol{r}) \varphi_k^*(\boldsymbol{r}) \varphi_j^*(\boldsymbol{r}') \varphi_k(\boldsymbol{r}')}{\omega + (\epsilon_k - \epsilon_j) + i\eta}, \tag{2.88}$$

where n_j and n_k are the occupation numbers of the KS ground state. Equation (2.88) has poles when the frequency ω equals the difference between KS energies representing the excitation spectrum of the KS system. The frequency dependent XC kernel in equation (2.87) can be obtained directly via Fourier transform. Alternatively, the Fourier transform of the Dyson-like equation provides another definition of the frequency dependent XC kernel:

$$f_{\text{xc}}(\boldsymbol{r}, \boldsymbol{r}', \omega) = \chi_{\text{s}}^{-1}(\boldsymbol{r}, \boldsymbol{r}', \omega) - \chi^{-1}(\boldsymbol{r}, \boldsymbol{r}'.\omega) - \frac{1}{|\boldsymbol{r} - \boldsymbol{r}'|}. \tag{2.89}$$

In the development of linear response TD-DFT, finding a suitable XC kernel is still an important topic. For example, in order to calculate spectra of insulators including the exciton effect, we have to use an XC kernel which is able to capture the exciton effect such as the long range kernel[44, 45] and the boostrap kernel[46]. We will have more discussion about the optical properties obtained by XC kernel and real-time evolution of TD-DFT in Chapter (3).

2.5 Ehrenfest dynamics

Ehrenfest dynamics is a mixed quantum-classical approach. The equations of motion of Ehrenfest dynamics are usually deduced by first approximating the full electron-nuclear wave function by an uncorrelated product of a purely electronic and a purely nuclear wave function, i.e.

$$\Psi(\underline{\boldsymbol{r}}, \underline{\boldsymbol{R}}, t) \approx \chi(\underline{\boldsymbol{R}}, t)\psi(\underline{\boldsymbol{r}}, t). \tag{2.90}$$

Plugging this approximate form into the time-dependent Schrodinger equation, multiplying with the nuclear wave function and integrating over the nuclear coordinates leads to the following equation of motion for $\psi(\underline{\boldsymbol{r}}, t)$:

$$i\frac{\partial\psi(\underline{\boldsymbol{r}}, t)}{\partial t} = \Big(\int d^3\underline{\boldsymbol{R}}\chi^*(\underline{\boldsymbol{R}}, t)\hat{H}_{\underline{\boldsymbol{R}}}^e(\underline{\boldsymbol{r}})\chi(\underline{\boldsymbol{R}}, t)\Big)\psi(\underline{\boldsymbol{r}}, t). \tag{2.91}$$

Multiplying with the electronic factor and integrating out the electronic coordinates leads to an analogous equation for the nuclear wave function $\chi(\underline{\boldsymbol{R}}, t)$. This set of coupled time-dependent mean-field equations is the starting point of the derivation. Furthermore we use the Ehrenfest theorem to evaluate the time-derivative of the nuclear momentum expectation value:

$$\frac{\partial\langle\boldsymbol{P}_\alpha\rangle}{\partial t} = \langle\Psi| - i[-i\nabla_{\underline{\boldsymbol{R}}_\alpha}, \hat{H}(\underline{\boldsymbol{R}}, \underline{\boldsymbol{r}})]|\Psi\rangle = -\langle\Psi|\nabla_{\underline{\boldsymbol{R}}_\alpha}\hat{H}_{\underline{\boldsymbol{R}}}^e(\underline{\boldsymbol{r}})|\Psi\rangle. \tag{2.92}$$

As a further approximation we now assume that the nuclear wave function $\chi(\underline{\boldsymbol{R}}, t)$ is a very narrow wave packet, e.g. a Gaussian with a very small width which ultimately is taken to zero. In this limit, Eq. (2.92) reduces to a Newton-like equation of motion

yielding a classical $3N_n$ dimensional trajectory $\underline{\boldsymbol{R}}_t$ for the nuclei, so that the right-hand side of equation (2.92) reduces to

$$\langle\Psi|\nabla_{\underline{\boldsymbol{R}}_\alpha}\hat{H}^e_{\underline{\boldsymbol{R}}}(\underline{\boldsymbol{r}})|\Psi\rangle \approx \langle\psi|\nabla_{\underline{\boldsymbol{R}}_\alpha}\hat{H}^e_{\underline{\boldsymbol{R}}}(\underline{\boldsymbol{r}})\big|_{\underline{\boldsymbol{R}}_t}|\psi\rangle. \tag{2.93}$$

In the following discussion, we denote $\nabla_{\underline{\boldsymbol{R}}_\alpha}\hat{H}^e_{\underline{\boldsymbol{R}}}(\underline{\boldsymbol{r}})\big|_{\underline{\boldsymbol{R}}_t}$ as $\nabla_{\underline{\boldsymbol{R}}_\alpha}\hat{H}^e_{\underline{\boldsymbol{R}}_t}(\underline{\boldsymbol{r}})$. We now expand the electron wavefunction with the complete set of BO basis,

$$\psi(\underline{\boldsymbol{r}},t) = \sum_k c_k(t)\psi^{\mathrm{BO}}_{\underline{\boldsymbol{R}}'_t,k}(\underline{\boldsymbol{r}}) \tag{2.94}$$

Note that we label the nuclear coordinate of the BO basis as $\underline{\boldsymbol{R}}'_t$ to distinguish it from the nuclear trajectory in Eq. (2.92) and Eq. (2.93). Thus, there is still no correlation between the electronic and nuclear wavefunctions. The nuclear coordinate $\underline{\boldsymbol{R}}'_t$ can then be determined through the following coordinate transformation:

$$\underline{\boldsymbol{R}}'_t = \underline{\boldsymbol{R}}_t. \tag{2.95}$$

The coordinate transformation in Eq. (2.95) is not at all trivial as it might appear because it points out that there are two different sets of independent variables[47]:$\{\psi;\underline{\boldsymbol{R}}_t\}$ and $\{c_k(t);\underline{\boldsymbol{R}}'_t\}$. Therefore, as stated at the beginning of this section, the electronic wavefunction ψ has no explicit dependence on nuclear coordinate $\underline{\boldsymbol{R}}$. We just expand the electronic wavefunctions with BO basis where the nuclear coordinate $\underline{\boldsymbol{R}}'_t$ is just a parameter.

Plug Eq. (2.94) into Eq. (2.93) within the primed coordinate and use the following relation:

$$\nabla_{\boldsymbol{R}'_\alpha}\langle\psi^{\mathrm{BO}}_{\underline{\boldsymbol{R}}'_t,j}(\underline{\boldsymbol{r}})|\hat{H}^e_{\underline{\boldsymbol{R}}'_t}|\psi^{\mathrm{BO}}_{\underline{\boldsymbol{R}}'_t,k}(\underline{\boldsymbol{r}})\rangle = \nabla_{\boldsymbol{R}'_\alpha}\mathcal{E}^{\mathrm{BO}}_{\underline{\boldsymbol{R}}'_t,k}\delta_{jk}, \tag{2.96}$$

we find the nuclear trajectory can be determined by

$$\begin{aligned}
\sum_\alpha M_\alpha\frac{d^2\boldsymbol{R}'_\alpha(t)}{dt^2} =\; &-\sum_{k,\alpha}|c_k(t)|^2\nabla_{\boldsymbol{R}'_\alpha}\mathcal{E}^{\mathrm{BO}}_{\underline{\boldsymbol{R}}'_t,k} \\
&+\sum_{j,k,\alpha}c^*_j(t)c_k(t)[\mathcal{E}^{\mathrm{BO}}_{\underline{\boldsymbol{R}}'_t,j}-\mathcal{E}^{\mathrm{BO}}_{\underline{\boldsymbol{R}}'_t,k}]\langle\psi^{\mathrm{BO}}_{\underline{\boldsymbol{R}}'_t,j}(\underline{\boldsymbol{r}})|\nabla_{\boldsymbol{R}'_\alpha}|\psi^{\mathrm{BO}}_{\underline{\boldsymbol{R}}'_t,k}(\underline{\boldsymbol{r}})\rangle,
\end{aligned} \tag{2.97}$$

where $\boldsymbol{R}'_\alpha(t)$ is the nuclear trajectory of nucleus α. One can immediately identify the non-adiabatic coupling matrix element $\langle\psi^{\mathrm{BO}}_{\underline{\boldsymbol{R}}'_t,j}(\underline{\boldsymbol{r}})|\nabla_{\boldsymbol{R}'_\alpha}|\psi^{\mathrm{BO}}_{\underline{\boldsymbol{R}}'_t,k}(\underline{\boldsymbol{r}})\rangle$ in Eq. (2.97). The non-adiabatic effect enters via the terms couple to the non-adiabatic coupling matrix elements. Now the nuclear amplitudes are classical trajectories, the Schrödinger equation of electrons of Eq. (2.91) becomes

$$i\frac{\partial\psi(\underline{\boldsymbol{r}},t)}{\partial t} = \hat{H}^e_{\underline{\boldsymbol{R}}_t}(\underline{\boldsymbol{r}})\psi(\underline{\boldsymbol{r}},t). \tag{2.98}$$

Plug Eq. (2.94) into Eq. (2.98) and integrate through the electron coordinate $\underline{\boldsymbol{r}}$ after multiplying Eq. (2.98) by $\psi^{\mathrm{BO}*}_{\underline{\boldsymbol{R}}'_t,k}(\underline{\boldsymbol{r}})$, we find

$$i\frac{\partial c_k(t)}{\partial t} = \mathcal{E}^{\mathrm{BO}}_k(\underline{\boldsymbol{R}}'_t)c_k(t) - \sum_j c_j(t) \sum_\alpha \frac{i}{M_\alpha} \langle\psi^{\mathrm{BO}}_{\underline{\boldsymbol{R}}'_t,k}|\nabla_{R'_\alpha}|\psi^{\mathrm{BO}}_{\underline{\boldsymbol{R}}'_t,j}\rangle \cdot \boldsymbol{P}_{\underline{\boldsymbol{R}}'_t,\alpha} \qquad (2.99)$$

where $\boldsymbol{P}_{\underline{\boldsymbol{R}}'_t,\alpha}$ is the momentum of nucleus α. Similar to Eq. (2.97), through classical nuclei trajectories and the non-adiabatic coupling matrix elements, the second term accounts for non-adiabatic effects in the electronic motion. From the equations above and removing all the primes, we can summarize the Ehrenfest dynamics as the follows:

$$\begin{aligned}
i\frac{\partial \psi(\underline{\boldsymbol{r}},t)}{\partial t} &= \hat{H}^e_{\underline{\boldsymbol{R}}_t}(\underline{\boldsymbol{r}})\psi(\underline{\boldsymbol{r}},t) \\
\sum_\alpha M_\alpha \frac{d^2\boldsymbol{R}_\alpha(t)}{dt^2} &= \sum_\alpha \langle\psi(\underline{\boldsymbol{r}},t)|\nabla_{\boldsymbol{R}_\alpha}\hat{H}^e_{\underline{\boldsymbol{R}}_t}(\underline{\boldsymbol{r}})|\psi(\underline{\boldsymbol{r}},t)\rangle
\end{aligned} \qquad (2.100)$$

Finally, as emphasized by X. Andrade et al.[47], the Ehrenfest dynamics is fully quantum coherent because the coefficients $c_k(t)$ are only responsible for the superposition of the electronic wavefunctions. Thus Ehrenfest dynamics is not able to describe quantum decoherence of a system.

2.6 Non-adiabatic Phonons

In Chapter 2.2, we described the calculation of the adiabatic vibrational spectrum by diagonalizing the Hessian, i.e. the matrix of second derivatives of a single Born-Oppenheimer surface. In practice one applies density-functional perturbation theory where the perturbation is the change in the Born-Oppenheimer Hamiltonian produced by the static displacement of the nuclei:

$$\Delta v(\underline{\boldsymbol{r}}) = H^{\mathrm{BO}}(\underline{\boldsymbol{r}},\underline{\boldsymbol{R}}+\underline{\boldsymbol{u}}) - H^{\mathrm{BO}}(\underline{\boldsymbol{r}},\underline{\boldsymbol{R}}). \qquad (2.101)$$

Non-adiabatic effects in the phonon spectrum can be defined[48] from the linear response to a time-dependent displacement

$$\Delta v(\underline{\boldsymbol{r}},t) = H^{\mathrm{BO}}(\underline{\boldsymbol{r}},\underline{\boldsymbol{R}}_0+\underline{\boldsymbol{u}}(t)) - H^{\mathrm{BO}}(\underline{\boldsymbol{r}},\underline{\boldsymbol{R}}_0) \qquad (2.102)$$

in the BO Hamiltonian. The force, $\boldsymbol{F}_\alpha(t)$ acting at time t on the α-th nucleus, produced by the displacement, $\boldsymbol{u}_\beta(t')$, of the β-th nucleus at time t', then leads to a time dependent generalization of the Hessian:

$$\Phi^{i,j}_{\alpha,\beta}(t,t') = -\frac{\delta F^i_\alpha(t)}{\delta u^j_\beta(t-t')} \qquad (2.103)$$

where indices i and j represent the Cartesian components of the nuclear position vectors. This quantity clearly depends on the time difference $(t - t')$, so we can perform a Fourier transform

$$\Phi^{i,j}_{\alpha,\beta}(\omega) = \int dt e^{i\omega(t-t')} \Phi^{i,j}_{\alpha,\beta}(t - t').$$
(2.104)

Since the perturbation of Eq. (2.102) is now time-dependent, it will trigger excitations to higher eigenstates of the BO Hamiltonian which makes the electronic response non-adiabatic. The diagonalization of the generalized frequency-dependent Hessian $\Phi_{\alpha,\beta}(\omega)$ leads to frequency-dependent eigenvalues $W_n(\omega)$. The non-adiabatic phonon-spectrum Ω^{NA} is finally calculated from the self-consistency condition:

$$\Omega^{\mathrm{NA}}_n = W_n(\Omega^{\mathrm{NA}}_n)$$
(2.105)

2.7 LAPW Method

Throughout this work, all the numerical calculation has been done by the Elk code. The Elk code is an all-electron full-potential linearised augmented-plane wave (LAPW) code with many advanced features. This section is aimed to briefly introduce the background of numerical implementation of the Elk code.

The Basis of the Calculation
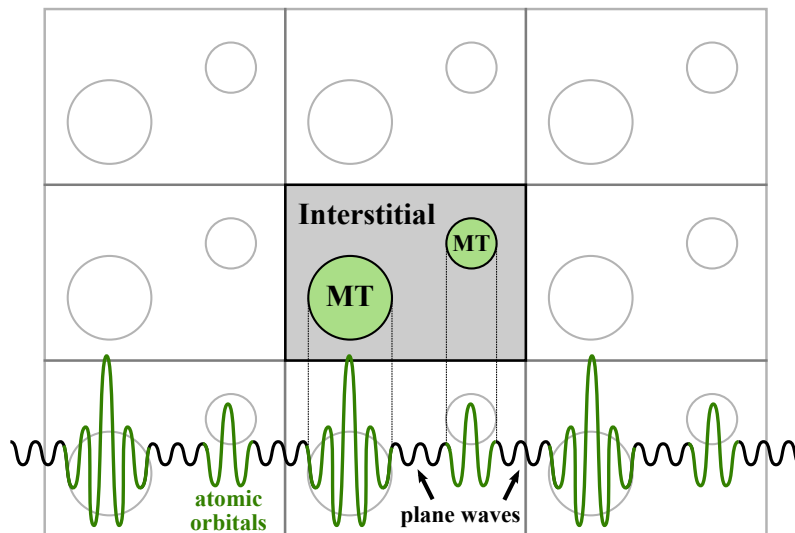
Figure 2.2
Schematic of the LAPW basis. The basis functions consist of a plane wave augmented by a linear combination of atomic-like functions in the muffin-tins, chosen such that the resulting function is continuous across the boundary.

We first describe the essential periodicity of our basis. In this work, we study solids with periodic structure. To deal with the periodic boundary condition, the Bloch theorem is the method of attack. Bloch's theorem states that the wave functions of the non-interacting electrons in a system with periodic potential $v(\boldsymbol{r}) = v(\boldsymbol{r} + \boldsymbol{R})$, where $\boldsymbol{R}$ is the lattice vector, must satisfy the following relation:

$$\phi_{\boldsymbol{k}}(\boldsymbol{r}) = e^{i\boldsymbol{kr}} u_{\boldsymbol{k}}(\boldsymbol{r}) \tag{2.106}$$

where

$$u_{\boldsymbol{k}}(r) = u_{\boldsymbol{k}}(\boldsymbol{r} + \boldsymbol{R}). \tag{2.107}$$

Wave functions of the form of Eq. (2.106) are called Bloch states. In practice, we represent our physical system in reciprocal space and the wave vector $\boldsymbol{k}$ is restricted to the first Brillouin zone. The time-independent Schrödinger equation for the periodic part (2.107) reads

$$\hat{H}_{\boldsymbol{k}} u_{i,\boldsymbol{k}}(\boldsymbol{r}) = \left[\frac{1}{2}(-i\nabla + \boldsymbol{k})^2 + v(\boldsymbol{r}) \right] u_{i,\boldsymbol{k}}(\boldsymbol{r}) = \varepsilon_{i,\boldsymbol{k}} u_{i,\boldsymbol{k}}(\boldsymbol{r}) \tag{2.108}$$

where $u_{i,\boldsymbol{k}}$ represents the i-th eigenstate with wave vector $\boldsymbol{k}$. With this representation, we are able to diagonalize the Hamiltonian of an individual wave vector $\boldsymbol{k}$. The expectation value of a physical observable $\langle \hat{O} \rangle$ is calculated via

$$\langle \hat{O} \rangle = \frac{\Omega}{(2\pi)^3} \int_{BZ} d^3k \sum_i \langle \phi_{i,\boldsymbol{k}} | \hat{O} | \phi_{i,\boldsymbol{k}} \rangle. \tag{2.109}$$

The integral runs over all the $\boldsymbol{k}$ vectors in first Brillouin zone and Ω is the volume of the unit cell.

Now we have to find suitable basis functions that are able to represent the Bloch states. The Elk code is an all-electron full-potential linearised augmented-plane wave (LAPW) code. The basis that the Elk code applies is augmented plane waves plus local orbitals (APW+lo)basis. APW+lo basis set is a extension of LAPW method which provides greater flexibility in finding solution than the original APW method. The concept of APW+lo is to separate an atom of a crystal into two parts, namely the muffin tin (MT) part and the interstitial part as depicted in figure (2.2). MT part is the region that electrons of an atom is close to the nuclei. In this region, the basis functions are assumed to be atomic-like thus are expanded in spherical harmonics. In the LAPW method, the basis functions in the MT are linear combinations of radial functions and their derivatives with respect to the linearisation parameters. The basis function is then

$$\psi_{\text{MT}}(\boldsymbol{r}) = \sum_{lm} \left[A_{lm} v_l(\boldsymbol{r}) + B_{lm} v_l'(\boldsymbol{r}) \right] Y_{lm}(\boldsymbol{r}) \tag{2.110}$$

where index l and m are the azimuthal and magnetic quantum number and $v_l(\boldsymbol{r})$ and $Y_{lm}(\boldsymbol{r})$ are the corresponding radial and angular solution of the spherical harmonic

in the region of MT. For the interstitial part, the basis functions are assumed to behave like plane waves.

$$\psi_k(\boldsymbol{r}) = \Omega^{-\frac{1}{2}} \sum_{\boldsymbol{G}}^{N_{\boldsymbol{G}}} C_{\boldsymbol{G}} e^{i(\boldsymbol{G}+\boldsymbol{k})\cdot\boldsymbol{r}} \qquad (2.111)$$

where $\boldsymbol{G}$ is the reciprocal lattice vector and $N_{\boldsymbol{G}}$ is the maximum number of reciprocal lattice vectors being used for the calculation. The basis functions are required to be continuous everywhere thus the matching coefficients A_{lm}, B_{lm} and $C_{\boldsymbol{G}}$ has to satisfy the continuity requirement at the boundary of MT and interstitial regime.

In the case of APW+lo, extra local orbitals are introduced and the basis functions in the MT are written as

$$\psi_{lo}(\boldsymbol{r}) = \sum_{lm} \left[A_{lm} v_l(\boldsymbol{r}) + \left(\tilde{B}_{lm} v_l(\boldsymbol{r}) + \tilde{C}_{lm} v_l'(\boldsymbol{r}) \right) \right] Y_{lm}(\boldsymbol{r}). \qquad (2.112)$$

The extra terms with new matching coefficients, $\tilde{B}_{lm}$ and $\tilde{C}_{lm}$, are the local orbitals. Basically APW+lo is equivalent to LAPW thus it is not suitable for dealing with semicore states. There are a few differences between APW+lo and LAPW. The first one is that APW+lo uses $v_l(\boldsymbol{r})$ for the less restricted linear combination of $v_l'(\boldsymbol{r})$. Second, APW+lo would be faster for setting up matrix elements because the first derivative terms enters only for important azimuthal quantum numbers. Lastly APW+lo has less restriction on its derivative at the MT-boundaries and it only requires that the local orbital vanishes continuously at the MT-boundary.

So far, the basis functions are constructed in non-relativistic regime. For low lying core states of heavy atoms which have enormous kinetic energies thus one can not disregard the relativistic effects. In the Elk code, these core states in MT regime are evaluated via solving the Dirac equation.

Second Variational Treatment

The Elk code solves the KS equation via a so-called second variational treatment which is used widely to deal with the difficult spin-orbit interactions. Second variational treatment is a two-step possess. The first step is called first variational step. In this step, ELK diagonalizes the Kohn-Sham Hamiltonian without any non-scalar interaction which might couple different spin states. The external potential of this type, for example, can be simply the static electric field. The next step is the second variational step. In this step, the non-scalar interaction is introduced into the Hamiltonian. For example, in the case of spin-orbit interaction, the Hamiltonian is simply

$$\hat{H}_{\text{2nd}} = \varepsilon_i \delta_{ij} + \hat{H}_{SOC}. \qquad (2.113)$$

Up to this point, the wave functions are variational spinors. Throughout this thesis, all the calculations are carried out in the second-variational basis. Since a second-variational state is a linear combination of the first-variational basis, we have to ensure that the size of first-variational basis is sufficiently large for the second-variational step.
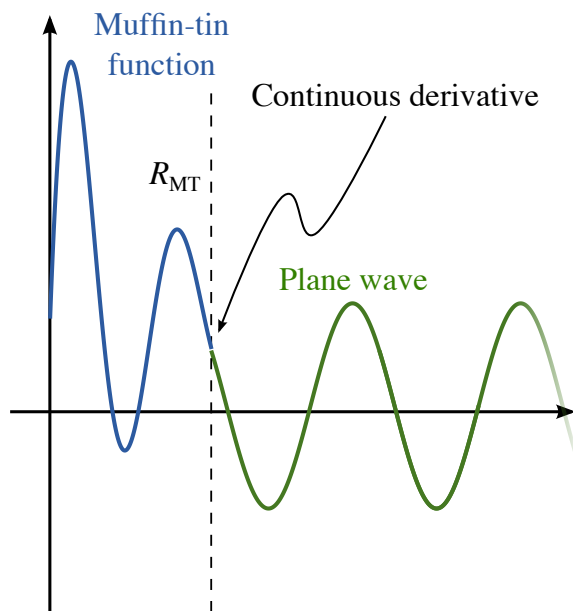
Figure 2.3
The requirement of the LAPW basis function at the MT boundary.
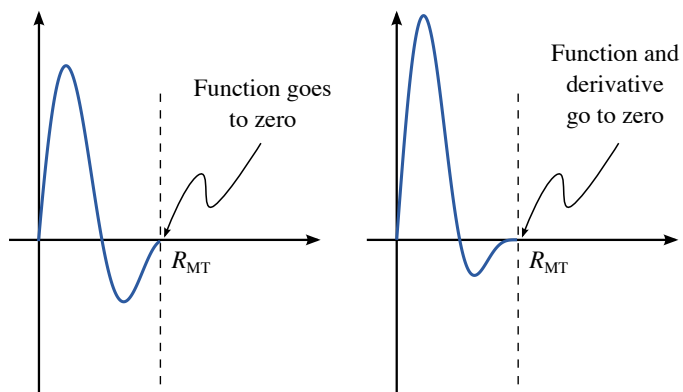
Figure 2.4
The local orbital function vanishes at the MT boundary.

3. Real-Time Evolution of TD-DFT

3.1 Real time scissor correction in TD-DFT

Real Time Scissor Correction in TD-DFT

C.-Y. Wang[1], P. Elliott[1], S. Sharma[2], and J. K. Dewhurst[1]

1 Max Planck Institute of Microstructure Physics, Weinberg 2, D-06120 Halle, Germany.
2 Max-Born Institute for Nonlinear Optics and Short Pulse Spectroscopy, Max-Born-Strasse 2A, D-12489 Berlin, Germany.

Abstract. We demonstrate how the scissor correction to the optical band gap, common in linear-response time-dependent density functional theory (TD-DFT), may be extended to the domain of real-time TD-DFT. This requires modifying both the eigenvalues and momentum matrix elements of the underlying basis set. It provides a simple and computationally economical approach for calculating accurate electron dynamics in solids. We demonstrate the importance of this correction for prototypical semiconductors, diamond and silicon, where the energy absorption in both the linear and non-linear regimes is examined. We also show that for a particular system, ZnSe, using the adiabatic local density approximation (ALDA) together with a scissor correction can be advantageous over other approximations, as the underlying quasi-particle band structure is more accurate.

1. Introduction

The electron dynamics induced by applying ultra-short and intense laser pulses has been of great interest recently [1–7]. In this regime (of fast timescales and large electromagnetic fields) systems responds in non-linear manner leading to several novel and interesting phenomena such as high harmonic generation [8] and dropleton formation [9]. Controlling these processes is an outstanding challenge for Physics and would be of great technological importance. In order to understand the underlying physics of this non-linear charge dynamics and to be able to predict future technology it is essential that we be able to accurately simulate intense light-matter interaction theoretically.

However, as the dynamics of electrons is inherently quantum mechanical in nature (especially in this regime), modeling and simulating these systems is a difficult problem. Moreover, the situation is further complicated for materials where many-body physics and collective excitations must also be correctly included. Hence, it is only in the last few years [3, 10–21] that *ab-initio* calculations have been performed for periodic systems.

Time dependent density functional theory (TD-DFT) is the natural candidate to use in this situation. By transforming the problem to the Kohn-Sham (KS) system of non-interacting fermions, realistic simulations become computationally tractable. The electron-electron interaction is then accounted by the exchange-correlation (XC) potential which must be approximated. The standard choice for this is the adiabatic approximation, which utilizes XC functionals from ground-state DFT. TD-DFT thus builds upon the enormous success which DFT has enjoyed in the past few decades [22–24] and has proved successful for both linear response calculations [24] and real-time dynamics [25–27] simulations.

However, using an adiabatic approximation also means we inherit all the problems from the underlying ground-state functional. The most well-known of these is the so-called band gap problem, whereby the KS band gap is typically much smaller than the quasi-particle gap [28, 29]. In TD-DFT, this error manifests itself as an underestimation of the optical absorption edge. This has a drastic effect on the predicted dynamics, for example the material will respond very differently if pumped with laser frequency greater or less than the gap. In the linear-response regime, a simple fix is to apply a scissor-operator which rigidly shifts the conduction band energies in order to correct the optical absorption gap [30]. However for real-time dynamics, this problem has been tackled by using more computationally demanding XC functionals like meta-GGAs, e.g mBJ [31], or Hybrids, e.g. HSE [32].

In this work we extend the concept of the scissor correction to the real-time domain; allowing us to more accurately simulate the dynamics of materials without any extra computational cost. By developing an easy-to-implement fix to the optical band gap problem, we can then utilize XC functionals which otherwise would be ruled out. For example, we will show that the underlying band structure of ZnSe is better described by LDA than by mBJ, but due to LDA underestimating the gap by 1.36 eV, it would be unsuitable for predicting real-time dynamics. Using simpler functionals combined with the real-time scissor correction will allow larger and more sophisticated calculations to be performed.

2. Background Theory

2.1. TD-DFT

Time-dependent density functional theory (TD-DFT) is an exact method for calculating the quantum-mechanical dynamics of interacting electrons. The Runge-Gross theorem [33] establishes the uniqueness of the mapping between density and potential, thereby making all observables functionals of the time-dependent density. The theorem also allows the formulation of the Kohn-Sham (KS) system, which consists of non-interacting fermions propagating in an effective potential such that it reproduces the density of the interacting electrons. The TD-KS equations read:

$$i\frac{\partial}{\partial t}\phi_j(\mathbf{r},t) = \left[\frac{1}{2}\left(-i\boldsymbol{\nabla} - \frac{1}{c}\mathbf{A}(t)\right)^2 + V_{KS}(\mathbf{r},t)\right]\phi_j(\mathbf{r},t),$$
(1)

where atomic units are used throughout, unless otherwise stated. The time-dependent density is

$$n(\mathbf{r},t) = \sum_{j=1}^{N}|\phi_j(\mathbf{r},t)|^2$$
(2)

where $\phi_j(\mathbf{r},t)$ are the Kohn-Sham orbitals, and N is the number of electrons (assuming the initial-state is the ground-state consisting of N fully occupied orbitals).

The Kohn-Sham effective potential is commonly decomposed into:

$$V_{KS}(\mathbf{r},t) = V_{\text{ext}}(\mathbf{r}) + V_{\text{H}}[n](\mathbf{r},t) + V_{\text{xc}}[n,\Psi_0,\Phi_0](\mathbf{r},t)$$
(3)

where $V_{\text{ext}}(\mathbf{r})$, is the external potential containing the electron-ion interaction, $V_{\text{H}}(\mathbf{r},t)$, the Hartree potential describing classical electrostatic interaction, and $V_{\text{xc}}(\mathbf{r},t)$, the exchange-correlation potential. An applied laser pulse is treated in the velocity gauge by the vector potential, $\mathbf{A}(t)$ such that

$$\mathbf{E}(t) = -\frac{1}{c}\frac{\partial\mathbf{A}(t)}{\partial t}.$$
(4)

This corresponds to making the dipole approximation for the electric field, $\mathbf{E}(t)$; the electric field is treated as a purely time dependent vector-field which is spatially constant.

The XC potential is formally a functional of the entire history of the density, as well as the initial interacting and non-interacting wave functions Ψ_0 and Φ_0. In a practical TD-DFT calculation, this must be approximated. Commonly a XC functional from ground-state DFT is used with the instantaneous density, this is known as adiabatic approximation.

2.2. Linear Response in TD-DFT

The optical absorption spectra, given by the imaginary part of the dielectric function, $\varepsilon(\omega)$, can be calculated from the conductivity tensor, $\sigma(\omega)$, using the relation:

$$\varepsilon(\omega) = 1 + \frac{4\pi i \sigma(\omega)}{\omega} \tag{5}$$

The conductivity is defined by the response of the current, $\mathbf{J}(\omega)$, to the applied electric field, $\mathbf{E}(\omega)$:

$$\mathbf{J}(\omega) = \sigma(\omega)\mathbf{E}(\omega) \tag{6}$$

In a real-time TD-DFT simulation, the TD-KS equations, Eq. (1), are propagated and the time-dependent current is calculated from the KS orbitals. The conductivity can then be found from the Fourier transform of $\mathbf{J}(t)$ and $\mathbf{E}(t)$. The average current per unit cell, $\mathbf{J}(t)$, is calculated via the momentum matrix:

$$\mathbf{J}(t) = \sum_j \sum_{\alpha\beta} c_{\alpha j}^*(t) c_{\beta j}(t) \mathbf{P}_{\alpha\beta} \tag{7}$$

where j labels the occupied TD-KS orbital, which can be expanded in the basis of GS KS states, i.e.

$$\phi_j(\mathbf{r}, t) = \sum_\alpha c_{\alpha j}(t) \varphi_\alpha(\mathbf{r}) \tag{8}$$

where

$$\hat{H}_{KS}^0 |\varphi_\alpha\rangle = \epsilon_\alpha |\varphi_\alpha\rangle \tag{9}$$

and H_{KS}^0 is the GS DFT KS Hamiltonian. The momentum matrix elements between these GS orbital can then be calculated:

$$\mathbf{P}_{\alpha\beta} = \langle \varphi_\alpha(\mathbf{r}) | -i\nabla | \varphi_\beta(\mathbf{r}) \rangle \tag{10}$$

A convenient choice for calculating the linear response of periodic systems is to use the vector potential

$$A(t) = -c\kappa\theta(t) \tag{11}$$

corresponding to an electric field of $E(t) = \kappa\delta(t)$ where $\theta(t)$ is heaviside step function. The Fourier transform of this electric field is simply a constant, meaning we

excite at all frequencies, and drastically simplify Eq. (6). The parameter κ can either be chosen sufficiently small or the response can expanded to first order as a function of κ.

Alternatively, the dielectric function can be calculated in the linear-response regime using:

$$\varepsilon^{-1}(\omega) = 1 + v\chi(\omega) \tag{12}$$

where v is the bare Coulomb interaction and $\chi(\omega)$ is the linear-response function of the interacting system. It is connected to the KS system via the Dyson-like equation:

$$\chi = \chi_0 + \chi_0(v + f_{\text{xc}})\chi \tag{13}$$

in compact notation. The XC kernel, f_{xc}, is the functional derivative of v_{xc} with respect to the density. The KS linear response is known from the first-order perturbation theory as

$$\chi_0(\mathbf{r}, \mathbf{r}', \omega) = \lim_{\eta \to 0} \sum_j \sum_k (n_k - n_j) \frac{\varphi_k^*(\mathbf{r})\varphi_j(\mathbf{r})\varphi_k(\mathbf{r}')\varphi_j^*(\mathbf{r}')}{\omega + (\epsilon_k - \epsilon_m) + i\eta} \tag{14}$$

For semi-conducting systems, the KS band gap, given by the energy difference between the highest occupied and lowest unoccupied states, is often much smaller than the quasi-particle band gap. When the absorption spectrum is calculated using Eqs. (12), (13), (14), this leads to an underestimation of the optical gap. To remedy this problem, the unoccupied conduction band energies can be rigidly shifted to higher energies by the so-called scissor operator [34, 35], often leading to reasonable spectra [30, 36].

2.3. The Time-Dependent Energy Functional

Although the Runge-Gross theorem states that all observables are unique functionals of the density, in many cases the exact functional dependence is not known. Thus, we require additional approximations for such observables. One such observable is the time dependent energy, for which a reasonable approximate form reads:

$$E[n](t) = \sum_{j=1}^N -\frac{1}{2} < \phi_j|\nabla^2|\phi_j > + \int V_{\text{ext}}(\mathbf{r}, t) n(\mathbf{r}, t) d^3r +$$
$$U[n(t)] + E_{\text{xc}}[n(t)] \tag{15}$$

where $U[n]$ is the Hartree electrostatic energy and $E_{\text{xc}}[n]$ is the XC energy corresponding to the ground-state XC potential used within the adiabatic approximation. It is known that this energy is conserved in the absence of external perturbations [37, 38] and will be exact in the adiabatic limit. By comparing this energy before and after an applied laser pulse, one can estimate the energy absorbed by the system.

2.4. Real-time Propagation

There are many propagation schemes [39] for the TD-KS equation (Eq. (1)), such as Crank-Nicolson, Split-Operator, Runge-Kutta, etc. In the ELK electronic structure code [40], the following algorithm is used:

(i) The TD-KS orbital is written in the basis of GS orbitals, as was seen in Eq. (8):

$$\phi_j(\mathbf{r}, t) = \sum_\alpha c_{\alpha j}(t)\varphi_\alpha(\mathbf{r}) \tag{16}$$

(ii) Potential $V_{KS}(\mathbf{r}, t)$ is calculated from $n(\mathbf{r}, t)$ (this determines $\hat{H}_{KS}(t)$).

(iii) The Hamiltonian is then diagonalized in the GS orbital basis

$$\sum_\gamma H^t_{\beta\gamma} a_{\gamma\alpha} = \tilde{\epsilon}_\alpha a_{\beta\alpha} \tag{17}$$

where

$$\begin{aligned}H^t_{\alpha\beta} &= <\varphi_\alpha \mid \hat{H}_{KS}(t) \mid \varphi_\beta> \\ &= \epsilon_\alpha \delta_{\alpha\beta} + <\varphi_\alpha \mid \delta\hat{V}_{KS}(t) \mid \varphi_\beta>\end{aligned} \tag{18}$$

and

$$\delta\hat{V}_{KS}(t) = \hat{H}_{KS}(t) - \hat{H}^0_{KS} \tag{19}$$

(iv) Each orbital $\phi_j(\mathbf{r}, t)$ is projected into this instantaneous eigenstate basis and time evolved to the next time step:

$$c_{\alpha j}(t + \Delta t) = \sum_{\beta\gamma} a^*_{\gamma\beta} c_{\gamma j}(t) a_{\alpha\beta} e^{-i\tilde{\epsilon}_\beta \Delta t} \tag{20}$$

Further details of this algorithm can be found in Ref. [41].

3. The Scissor Correction in Real-Time TD-DFT

The real-time (RT) scissor correction is done in two steps. First the conduction band GS orbital energies are shifted by Δ

$$\begin{cases} \epsilon_\alpha = \epsilon_\alpha & \epsilon_\alpha \leq \epsilon_F \\ \epsilon_\alpha = \epsilon_\alpha + \Delta & \epsilon_\alpha > \epsilon_F \end{cases} \tag{21}$$

where ϵ_F is the Fermi energy. These energies enter the time-propagation via Eq. (18). Secondly, the momentum matrices used to calculate the current and the coupling to the $\mathbf{A}$ field are scaled by a factor $(\epsilon_{\alpha\beta} + \Delta)/\epsilon_{\alpha\beta}$:

$$\tilde{\mathbf{P}}_{\alpha\beta} = \frac{\epsilon_{\alpha\beta} + \Delta}{\epsilon_{\alpha\beta}} \mathbf{P}_{\alpha\beta} \tag{22}$$

where ϵ_g is the Kohn-Sham band gap. Thus this scaling factor would directly affect the value of $\mathbf{J}(t)$ as in Eq. (7)

In Ref. [30], it was shown that the XC kernal of linear-response TDDFT can be separated into two terms. The first corrects the band gap, while the second is responsible for capturing the excitonic physics. If this approach is extended to the real-time case, then the effect of the first term can be reproduced using the scissor correction outlined above. Thus Δ should be chosen to correct the KS gap to the fundamental gap. This can be done using a one-time higher level DFT GKS calculation, e.g. using a meta-GGA/hybrid functional, or via many-body perturbation theory using the *GW* approximation (i.e. $\Delta = \epsilon_g^{GW} - \epsilon_g^{KS}$). Alternatively Δ may be set empirically using the experimental absorption spectra.

3.1. Computational details

All calculations were performing using the all-electron full-potential linearised-augmented-plane-wave (LAPW) elk code [40]. In all cases, the experimental lattice parameters [42] were used: 3.57 Å for diamond, 5.43 Å for silicon and 5.67 Å for zinc selenide. A shifted $\mathbf{k}$-point grid of at least $10 \times 10 \times 10$ was used. For real-time propagation, a time step of 0.0024 femtosecond was used. In order to acquire reasonable linear response spectra from real-time propagation, a total simulation time, T, of 27.8 femtoseconds was required. Following Ref. [25], a third-order polynomial in the form of

$$f(t) = 1 - 3\left(\frac{t}{T}\right)^2 + 2\left(\frac{t}{T}\right)^3 \tag{23}$$

is applied to current $\mathbf{J}(t)$ in order to eliminate high frequency oscillations in the Fourier transform. The real time scissor shifts, Δ, were set empirically to correct the optical absorption gap: 0.86 eV for Si, 1.42 eV for C, and 1.36 eV for ZnSe. Simlar values for Δ would be found by the direct band gap based on GW calculation [43–45].

4. Results and discussion

4.1. Linear regime

Figures 1(a) and 1(b) show the absorption spectra of diamond and silicon calculated using the adiabatic local density approximation (ALDA) with and without the scissor correction (labeled ALDA+Δ and ALDA). In order to calculate the dielectric function the unit-cell averaged current was calculated and the spectra extracted via Eqs. (5) and (6). This current (for diamond) is shown in Fig. 1(c). As expected the scissors corrected absorption spectra is exactly the same as the uncorrected spectra but rigidly shift to higher energy by amount Δ. When comparing this data to experiments we find that for silicon, the ALDA+Δ spectrum correctly reproduces the

absorption peak at 4.4 eV. The peak around 3 eV in experimental data is due to excitons and is highly underestimated in the TD-DFT results because the ALDA kernel which does not include electron and hole interactions misses the excitonic effects. For diamond the uncorrected spectra appears to be in better agreement with experimental data. However, this is highly misleading; in diamond the excitonic effects shift the spectra to lower energies by the same amount [46, 47] as the underestimation of the Kohn-Sham band gap. Thus the two effects cancel giving the appearance of a better agreement. Thus uncorrected ALDA leads to correct position of absorption peak for wrong reasons.

In order to demonstrate the importance of this correction in Fig. 2 we plot the absorbed energy as a function of time for diamond and silicon irradiated with laser pulses of two different frequencies: 1) a frequency below the true optical gap, but above the LDA gap (2.72 eV for silicon, 5.61 eV for diamond), and 2) a frequency slightly above the true direct gap (3.58 eV for silicon, 7.33 eV for diamond). For these calculations, we use the following vector potential:

$$\mathbf{A}(t) = \mathbf{A}_0 \frac{e^{-(t-t_0)^2/2\sigma_g^2}}{\sigma_g\sqrt{2\pi}} \sin(\omega(t - t_0)) \qquad (24)$$

which corresponds to a laser pulse of frequency ω, with a Gaussian envelope of width σ_g centered at time t_0. The incident intensity is controlled by the amplitude, A_0. In this case we choose amplitudes corresponding to peak intensities of 10^{11} W/cm^2 for silicon and 10^{12} W/cm^2 for diamond. The variance σ_g is chosen to give a FWHM of 6.29 femtosecond.

Since for these intensities the linear order term in the response function is dominating, we expect to see little-to-no absorption for frequencies below the band gap the transient behavior of the energy during the pulse was explored in Schultze *et al* [48]. However, we find in Figs 2(a) and 2(c) that ALDA vastly overestimates the absorbed energy. The scissor corrected calculation also shows a non-zero absorption for these frequencies due to the contribution of higher order effects even at these small intensities. Pumping the system with pulses above the direct band gap of the material, we see in Figs. 2(b) and 2(d), that both ALDA and ALDA+Δ now show absorption, however ALDA shows much larger absorption.

This behavior can be understood by the cartoon in Fig. 3, which shows a simplified representation of the underlying band structure of ALDA and ALDA+Δ. Consider what will happen if we were to pump with the frequency labeled ω in Fig. 3(a), which is less than the true gap. In this case we should not excite any electrons from the valence to the conduction band, and should not absorb any energy. If we now
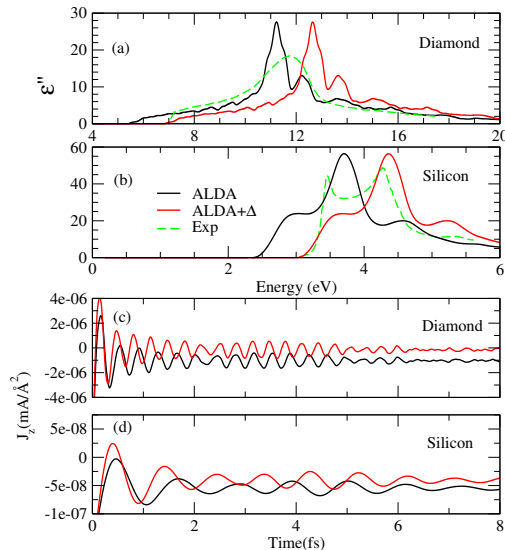
Figure 1. The spectrum calculated from real time TD-DFT simulations for the dielectric function ($\epsilon(\omega) = \epsilon'(\omega) + i\epsilon''(\omega)$) of diamond and silicon with ALDA and scissor corrected ALDA for (a) diamond and (b) silicon. The unit-cell averaged current in diamond and silicon induced by the perturbation is shown in (c) and (d).

compare how ALDA and LDA+Δ will behave for this scenario, we find very different results. With this frequency we can reach the LDA conduction band, hence ALDA will erroneously absorb energy, while LDA+Δ will behave correctly. If we instead pump with the frequency ω' illustrated in 3(b), we can now reach the respective conduction bands for both cases, meaning both will absorb. However, as ALDA will have a higher density of available states in which to excite, hence it overestimates the absorption in this case.

4.2. Nonlinear regime

We now go beyond the linear regime to study the response of semiconductors to strong laser pulses. This non-linear regime, where novel and interesting processes such as multi-photon absorption occur, is increasingly probed by experiment. Here the dependence on the laser pulse intensity is determined by underlying band structure, thus it is vitally important to correctly describe the correct positions of these bands, in order to perform accurate *ab-initio* simulations of such systems.

The dependence of the absorbed energy as a function of laser peak intensity is shown in Fig. 4 for silicon and diamond. The frequency of the laser is chosen to be half of the LDA gap ($\omega = 1.36$
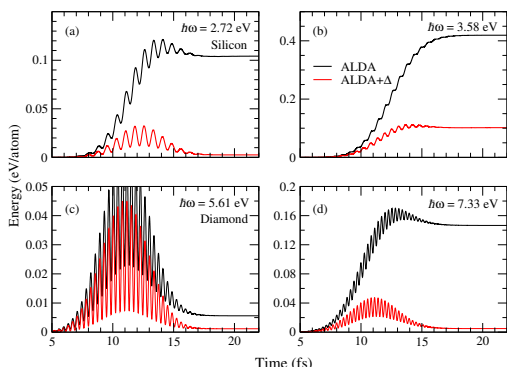
Figure 2. The energy absorbed by silicon (a),(b) and diamond (c),(d) due to applied laser pulses in linear response regime with frequencies below (a),(c) and above (b),(d) the respective optical gaps.
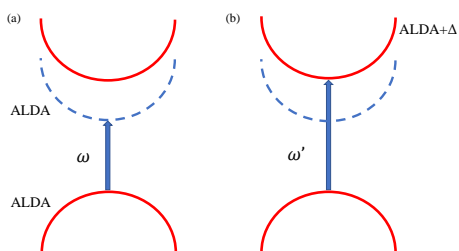

Figure 3. Schematic showing how LDA and scissor-corrected LDA band structure leads to overestimation of the ALDA absorbed energy.

eV for Si and $\omega = 2.80$ eV for Diamond), so that there is little linear response in both the ALDA and ALDA+Δ cases. As the laser intensity increases, the probability of absorbing multiple photons increases, signifying the onset of non-linear behavior. Here we find that ALDA predicts a much lower threshold for non-linear behavior for both Si and diamond. The scissor corrected ALDA behaves as expected, and is at least an order of magnitude higher than ALDA. Such a large difference between the two cases shows the importance of the scissor correction for obtaining the threshold for nonlinear effect. For this particular choice of frequency, diamond requires a much stronger laser pulse to reach the non-linear regime due to the difference in the percentage error of the LDA gap error and the difference in the conduction band structure.

4.3. Comparison to meta-GGA functionals

In this section, we compare our ALDA+Δ correction to an alternative approach to the band gap problem. The
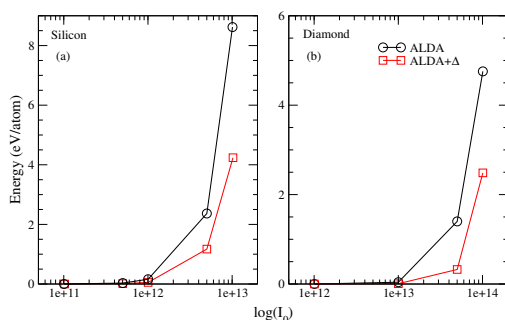
Figure 4. The energy absorbed by (a) silicon and (b) diamond after a short laser pulse as a function of the peak intensity (plotted on a log scale). The frequency of laser pulse is chosen to be half the respective LDA band gap.

modified Becke-Johnson (mBJ) potential [31] is known to provide KS band gaps closer to the quasi-particle band gap. Hence, it has been proposed as a solution to the optical gap problem in TD-DFT [49]. Indeed a recent study [50] has shown that the absorption spectra for Silicon calculated from a real-time TD-DFT calculation using the mBJ potential agrees well with experiment. However GS calculations have shown that while mBJ can predict reasonable bandgaps, the bandwidths are often underestimated [51, 52]. This can be seen in s,p band semiconductors such as MgO, as well as d-band materials such as ZnSe. In the following, we will focus on the semiconductor ZnSe, which has a direct gap of 2.82 eV [53], to see how this band-narrowing in the mBJ band structure affects the absorption spectrum. Note, we use mBJ$_{opt}$ to refer to the mBJ functional tuned to give $\epsilon_g^{KS} = \epsilon_g^{Exp}$

In Fig. 5 we compare the band structure of ZnSe from mBJ$_{opt}$ and scissor-corrected LDA calculations to the higher-level GW quasi-particle band structure from Ref. [45]. By design, both LDA+Δ and mBJ$_{opt}$ give the correct direct band gap at the Γ point. Following the bands throughout the Brillouin Zone, we see that mBJ$_{opt}$ has squeezed the width of both the valence and conduction bands. This can be best seen at the X point where the valence band at -4 eV (relative to the Fermi energy) is 1 eV higher than the GW band, while the lowest conduction band is 1 eV too low. The LDA+Δ bands are in much better agreement with the GW calculations.

The cumulative effect of the incorrect mBJ$_{opt}$ band structure can be seen in the optical absorption spectrum plotted in Fig. 6, where we performed real-time linear response calculations for both ALDA+Δ and mBJ$_{opt}$. We compare to the experimental results from Ref. [54], where three prominent peaks at 4.75 eV, 6.40 eV, and 8.25 eV can be resolved. For each of these peaks, the mBJ$_{opt}$ results are 0.5 eV too low.
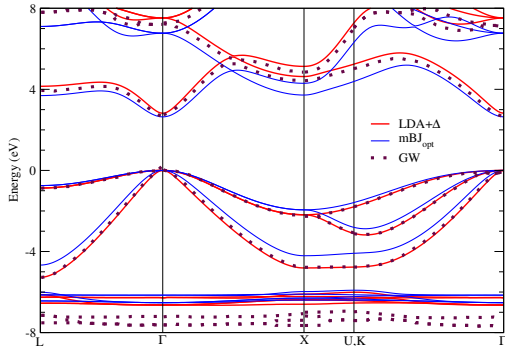
Figure 5. Band structures of ZnSe from calculations of scissor corrected LDA, modified Becke-Johnson potential, and GW MBPT from reference [45]
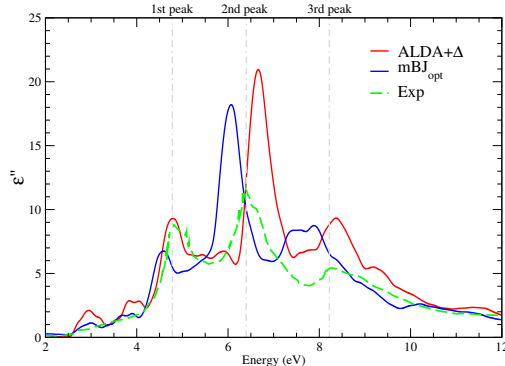

Figure 6. The $\epsilon''(\omega)$ of ZnSe from real-time linear response calculations using scissor corrected ALDA and the optimized modified Beche-Johnson potential mBJ$_{opt}$, compared to the experimental data from reference [54].

Figure 7. Energy absorbed by ZnSe following applied laser pulses of frequency 6.07 eV (upper panel) and 6.67 eV and peak intensity 10^{11} W/cm^2.

This is consistent with the bandwidth narrowing we observed in Fig. 5. In contrast, the position of these peaks predicted by ALDA+Δ is in better agreement with experimental. Both the first and third peaks are correct, while the second peak is 0.3 eV too high.

Finally, we compare the absorbed energy predicted by ALDA+Δ and mBJ$_{opt}$ for two laser pulses with frequencies 6.07 eV and 6.67 eV respectively. In the first case, mBJ$_{opt}$ predicts a more excited final state than ALDA+Δ, while the situation is reversed for the second pulse. This demonstrates how important the choice of functional is when simulating laser induced dynamics, as they can give even opposite results. In Fig. 6 we saw that ALDA+Δ gave a better description of the absorption spectrum of ZnSe, it follows that it will be a better choice when investigating real-time dynamics. Particularly if quantitative comparison with experimental work is desired.

While we focused on ZnSe, the problems mBJ has in describing the band structure of *d*-electrons are known for a number of materials [51]. For such cases, we have seen that this leads to errors in the TD-DFT dynamics and thus using ALDA+Δ will be a better choice, for these materials.

5. Summary

To summarize, in this paper we have implemented a computationally simple scheme to rectify the band gap problem in real-time TD-DFT simulations. We have demonstrated why such a fix is necessary. In particular, when pumping below the optical band gap, where uncorrected ALDA behaves qualitatively incorrectly. We have also investigated how the real-time scissor correction is essential for describing non-linear dynamics such as multi-photon absorption. This allows the full power of TD-DFT to be easily utilized

in the emerging field of ultra-fast, ultra-strong, laser pulses. We note that in the linear-response regime, XC kernels which can predict excitons, also require a scissor correction. Thus it is likely that the real-time scissor correction is a necessary development along with XC potentals which can correctly describe excitons in real time.

The real-time scissor correction presented here consists of two changes to the underlying basis set: 1) the eigenvalues above the Fermi level are shifted by Δ, and 2) the momentum matrix elements are

re-scaled. The value of Δ may be found *ab-inito*, from a one-time higher level calculation (e.g. mBJ or HSE or hybrid functionals within DFT or GW method). While we applied this procedure to all states, it may be easily modified to act on individual bands. This would be useful in cases where the DFT band structure is reasonable except for the positioning of particular bands such as deeper, localized, states, and is not necessarily restricted to insulating or semi-conducting systems. One might also apply a k-dependent scissor shift to correct the band structure at particular k-points. Another possible modification is to use a time-dependent scissor operator to help account for changes in the band structure during non-linear dynamics. This method may also be applied to similar methods to TDDFT, e.g. time-dependent current density functional theory, in cases where the optical band gap is also underestimated.

Lastly we demonstrated how the real-time scissor method is a more suitable choice for describing the dynamics of ZnSe compared to the meta-GGA mBJ functional. While both approaches correct the optical band gap as required, we found the mBJ optical absorption spectra to be worse than ALDA+Δ. This is due to errors in the underlying band structure, where mBJ is known to incorrectly narrow the bandwidth of some bands. Thus, it is better to use the real-time scissor correction to calculate the dynamics of ZnSe and similar materials.

6. Acknowledgements

[1] E Beaurepaire, J-C Merle, A Daunois, and J-Y. Bigot. Ultrafast spin dynamics in ferromagnetic nickel. *Phys. Rev. Lett*, 76:4250, 1996.

[2] A Schiffrin, T Paasch-Colberg, N Karpowicz, V Apalkov, D Gerster, S Mühlbrandt, M Korbman, J Reichert, M Schultze, S Holzner, J V Barth, R Kienberger, R Ernstorfer, V S Yakovlev, M I Stockman, and F Krausz. Optical-field-induced current in dielectrics. *Nature*, 493:70, 2013.

[3] K Yabana, T Sugiyama, Y Shinohara, T Otobe, and G F Bertsch. Time-dependent density functional theory for strong electromagnetic fields in crystalline solids. *Phys. Rev. B*, 85:045134, 2012.

[4] E Goulielmakis, Z-H Loh, A Wirth, R Santra, N Rohringer, V S Yakovlev, S Zherebtsov, T Pfeifer, A M Azzeer, M F Kling, S R Leone, and F Krausz. Real-time observation of valence electron motion. *Nature*, 466:739, 2010.

[5] C A Rozzi, S M Falke, N Spallanzani, A Rubio, E Molinari, D Brida, M Maiuri, G Cerullo, H Schramm, J Christoffers, and C Lienau. Quantum coherence controls the charge separation in a prototypical artificial light-harvesting system. *Nature Communication*, 4:1602, 2013.

[6] L Le Guyader, S El Moussaoui, M Buzzi, R V Chopdekar, L J Heyderman, A Tsukamoto, A Itoh, A Kirilyuk, Th Rasing, A V Kimel, and F Nolting. Demonstration of laser induced magnetization reversal in gdfeco nanostructures. *Applied Physics Letters*, 101:022410, 2012.

[7] A Eschenlohr, M Battiato, P Maldonado, N Pontius, T Kachel, K Holldack, R Mitzner, A Föhlisch, P M Oppeneer, and C Stamm. Ultrafast spin transport as key to femtosecond demagnetization. *Nature Materials*, 12:332, 2013.

[8] W Li, X Zhou, R Lock, S Patchkovskii, A Stolow, H C Kapteyn, and M M Murnane. Time-resolved dynamics in N_2O_4 probed using high harmonic generation. *Science*, 322:1207, 2008.

[9] A E Almand-Hunter, H Li, S T Cundiff, M Mootz, M Kira, and S W Koch. Quantum droplets of electrons and holes. *Nature*, 506:471, 2014.

[10] M Grüning and C Attaccalite. Second harmonic generation in h-BN and MoS_2 monolayers: Role of electron-hole interaction. *Phys. Rev. B*, 89:081102(R), 2014.

[11] D Karlsson, A Privitera, and C Verdozzi. Time-dependent density-functional theory meets dynamical mean-field theory: Real-time dynamics for the 3d hubbard model. *Phys. Rev. Lett.*, 106:116401, 2011.

[12] C Attaccalite, M Grüning, and A Marini. Real-time approach to the optical properties of solids and nanostructures: Time-dependent bethe-salpeter equation. *Phys. Rev. B*, 84:245110, 2011.

[13] M Stamenova, J Simoni, and S Sanvito. Role of spin-orbit interaction in the ultrafast demagnetization of small iron clusters. *Phys. Rev. B*, 94:014423, 2016.

[14] K Krieger, J K Dewhurst, P Elliott, S Sharma, and E K U Gross. Laser-induced demagnetization at ultrashort time scales: Predictions of tddft. *J. Chem. Theory Comput.*, 11:4870–4874, 2015.

[15] P Elliott, T Müller, J K Dewhurst, S Sharma, and E K U Gross. Ultrafast laser induced local magnetization dynamics in heusler compounds. *Scientific Reports*, 6:38911, 2016.

[16] K Krieger, P Elliott, T Müller, N Singh, J K Dewhurst, E K U Gross, and S Sharma. Ultrafast demagnetization in bulk versus thin films: an ab initio study. *Journal of Physics: Condensed Matter*, 29(22):224001, 2017.

[17] J K Dewhurst, P Elliott, S Shallcross, E K U Gross, and S Sharma. Laser-induced intersite spin transfer. *Nano Letters*, 18(3):1842–1848, 2018.

[18] P Elliott, M Stamenova, J Simoni, S Sharma, S Sanvito, and E K U Gross. Time-dependent density functional theory for spin dynamics. In W Andreoni and S Yip, editors, *Handbook of Materials Modeling : Methods: Theory and Modeling*, pages 1–26. Springer International Publishing, Cham, 2018.

[19] A R Attar, A Bhattacherjee, C D Pemmaraju, K Schnorr, K D Closser, D Prendergast, and S R Leone. Femtosecond x-ray spectroscopy of an electrocyclic ring-opening reaction. *Science*, 356:54–59, 2017.

[20] I Floss, C Lemell, G Wachter, V Smejkal, S A Sato, X-M Tong, K Yabana, and J Burgdörfer. *Ab initio* multiscale simulation of high-order harmonic generation in solids. *Phys. Rev. A*, 97:011401(R), 2018.

[21] J K Dewhurst, S Shallcross, E K U Gross, and S Sharma. Substrate-controlled ultrafast spin injection and demagnetization. *Phys. Rev. Applied*, 10:044065, 2018.

[22] M A L Marques and E K U Gross. Time-dependent density functional theory. *Annu. Rev. Phys. Chem*, 55:427, 2004.

[23] K Burke, J Werschnik, and E K U. Gross. Time-dependent density functional theory: Past, present, and future. *J. Chem.Phys*, 123:062206, 2005.

[24] M E Casida and M Huix-Rotllant. Progress in time-dependent density-functional theory. *Annu. Rev. Phys. Chem*, 63:287, 2012.

[25] K Yabana, T Nakatsukasa, J-I Iwata, and G F

Bertsch. Real-time, real-space implementation of the linear response time-dependent density-functional theory. *phys. stat. sol. (b)*, 243(5):1121, 2006.

[26] V Shokeen, M Sanchez Piaia, J-Y Bigot, T Müller, P Elliott, J K Dewhurst, S Sharma, and E K U Gross. Spin flips versus spin transport in nonthermal electrons excited by ultrashort optical pulses in transition metals. *Phys. Rev. Lett.*, 119:107203, 2017.

[27] J Chen, U Bovensiepen, A Eschenlohr, T Müller, P Elliott, E K U Gross, JK Dewhurst, and S Sharma. Unraveling the quantum nature of ultrafast spin injection at co/cu (001) interfaces. *arXiv:1803.03090*, 2018.

[28] L J Sham and M Schlüter. Density-functional theory of the band gap. *Phys. Rev. B*, 32:3883, 1985.

[29] X Zhu and S G Louie. Quasiparticle band structure of thirteen semiconductors and insulators. *Phys. Rev. B*, 43:14142, 1991.

[30] S Sharma, J K Dewhurst, and E K U Gross. Optical response of extended systems using time-dependent density functional theory. In Cristiana Di Valentin, Silvana Botti, and Matteo Cococcioni, editors, *First Principles Approaches to Spectroscopic Properties of Complex Materials*, pages 235–257. Springer, 2014.

[31] F Tran and P Blaha. Accurate band gaps of semiconductors and insulators with a semilocal exchange-correlation potential. *Phys. Rev. Lett.*, 102:226401, 2009.

[32] J Heyd, G E Scuseria, and M Ernzerhof. Hybrid functionals based on a screened coulomb potential. *J. Chem. Phys.*, 118:8207, 2003.

[33] E Runge and E K U Gross. Density-functional theory for time-dependent systems. *Phys. Rev. Lett.*, 52:997, 1984.

[34] Z H Levine and D C Allan. Linear optical response in silicon and germaniusn including self-energy effects. *Phys. Rev. Lett.*, 63:1719, 1989.

[35] F Nastos, B Olejnik, K Schwarz, and J E Sipe. Scissors implementation within length-gauge formulations of the frequency-dependent nonlinear optical response of semiconductors. *Phys. Rev. B*, 72:045223, 2005.

[36] F Kootstra, P L de Boeij, and J G Snijders. Application of time-dependent density-functional theory to the dielectric function of various nonmetallic crystals. *Phys. Rev. B*, 62:7071, 2000.

[37] G F Bertsch, J-I Iwata, A Rubio, and K Yabana. Real-space, real-time method for the dielectric function. *Phys. Rev. B*, 62:7998, 2000.

[38] M Mundt. *Orbital Functionals in Time-Dependent Density-Functional Theory*. PhD thesis, University of Bayreuth, 2007.

[39] A Castro, H Appel, C A Rozzi M Oliveira, X Andrade, F Lorenzen, M A L Marques, E K U Gross, and A Rubio. octopus: a tool for the application of time-dependent density functional theory. *phys. stat. sol. (b)*, 243(11):2465, 2006.

[40] J K Dewhurst *et al*. `http://elk.sourceforge.net`.

[41] J K Dewhurst, K Krieger, S Sharma, E K U Gross. An efficient algorithm for time propagation as applied to linearized augmented plane wave method. *Computer Physics Communications*, 209:92, 2016.

[42] R W G Wyckoff. *Crystal tructures*, volume 1. Interscience Publishers, 2 edition, 1963.

[43] M S Hybertsen and S G Louie. First-principles theory of quasiparticles: Calculation of band gaps in semiconductors and insulators. *Phys. Rev. Lett.*, 55:1418, 1985.

[44] R W Godby, M Schlüter, and L J Sham. Self-energy operators and exchange-correlation potentials in semiconductors. *Phys. Rev. B*, 37:10159, 1988.

[45] W Luo, S Ismail-Beigi, M L Cohen, and S G Louie. Quasiparticle band structure of ZnS and ZnSe. *Phys. Rev. B*, 66:195215, 2002.

[46] S Sharma, J K Dewhurst, A Sanna, and E K U Gross. Bootstrap approximation for the exchange-correlation kernel of time-dependent density-functional theory. *Phys. Rev. Lett.*, 107:186401, 2011.

[47] S Sharma, J K Dewhurst, S Shallcross, G K Madjarova, and E K U Gross. Excitons in organics using time-dependent density functional theory: PPV, Pentacene, and Picene. *Journal of Chemical Theory and Computation*, 11(4):1710–1714, 2015.

[48] M Schultze, E M Bothschafter, A Sommer, S Holzner, W Schweinberger, M Fiess, M Hofstetter, R Kienberger, V Apalkov, V S Yakovlev, M I Stockman, and F Krausz. Controlling dielectrics with the electric field of light. *Nature*, 493:75, 2013.

[49] S A Sato, K Yabana, Y Shinohara, T Otobe, K-M Lee, and G F Bertsch. Time-dependent density functional theory of high-intensity short-pulse laser irradiation on insulators. *Phys. Rev. B*, 92:205413, 2015.

[50] S A Sato, Y Taniguchi, Y Shinohara, and K Yabana. Nonlinear electronic excitations in crystalline solids using meta-generalized gradient approximation and hybrid functional in time-dependent density functional theory. *J. Chem. Phys.*, 143:224116, 2015.

[51] D J Singh. Electronic structure calculations with the Tran-Blaha modified Becke-Johnson density functional. *Phys. Rev. B*, 82:205102, 2010.

[52] D Waroquiers, A Lherbier, A Miglio, M Stankovski, S Poncé, M J T Oliveira, M Giantomassi, G-M Rignanese, and Xavier Gonze. Band widths and gaps from the tran-blaha functional: Comparison with many-body perturbation theory. *Phys. Rev. B*, 87:075121, 2013.

[53] H Venghaus. Valence-band parameters and g factors of cubic zinc selenide derived from free-exciton magnetoreflectance. *Phys. Rev. B*, 19:3071, 1979.

[54] J L Freeouf. Far-ultraviolet reflectance of II-VI compounds and correlation with the penn—phillips gap. *Phys. Rev. B*, 7:3810, 1973.

3.2   Appendix

Momentum Matrix in Scissor Correction

The real-time (RT) scissor correction is implemented in two steps. First the conduction band GS orbital energies are shifted by Δ

$$
\begin{cases}
\epsilon_j = \epsilon_j & \epsilon_j \leq \epsilon_F \\
\epsilon_j = \epsilon_j + \Delta & \epsilon_j > \epsilon_F
\end{cases}
\tag{3.1}
$$

where ϵ_F is the Fermi energy. The scissor correction modifies the eigenvalues while keeping the KS orbitals unchanged. From Eq. (3.1), we define the scissor operator as

$$
\hat{S} = \Delta \sum_{\epsilon_j > \epsilon_F} |\varphi_j\rangle\langle\varphi_j|
\tag{3.2}
$$

which shifts the eigenvalues of conducting states by Δ. The modified KS Hamiltonian $\hat{\tilde{H}}_s(t)$ to be propagated is given by

$$
\hat{\tilde{H}}_s = \hat{H}_s(t) + \hat{S}.
\tag{3.3}
$$

These modified energies enter the time-propagation through TD-KS equations. However, the imaginary part of the dielectric function calculated naively this way would be wrong. It is because the momentum matrix element for the scissor-corrected Hamiltonian should also be modified. The momentum operator for a scissor-corrected Hamiltonian $\hat{\tilde{H}}$ is given by

$$
\hat{\tilde{P}}_a = -i \left[\hat{r}_a, \hat{\tilde{H}}_s \right],
\tag{3.4}
$$

where $\hat{r}_a$ is the position operator in direction of a. The momentum matrix element connecting the valence state and the conducting state is $\langle\varphi_c|\hat{\tilde{P}}|\varphi_v\rangle$, where $|\varphi_c\rangle$ and $|\varphi_v\rangle$ are the conducting state and the valence state respectively. Making use of the relation of

$$
\langle\varphi_c|\hat{r}_a|\varphi_v\rangle = \frac{i}{\epsilon_v - \epsilon_c}\langle\varphi_c|\hat{P}_a|\varphi_v\rangle
\tag{3.5}
$$

to calculate the modified momentum matrix element with commutator relation of Eq. (3.4), we find

$$
\langle\varphi_c|\hat{\tilde{P}}_a|\varphi_v\rangle = \frac{\epsilon_c + \Delta - \epsilon_v}{\epsilon_c - \epsilon_v}\langle\varphi_c|\hat{P}_a|\varphi_v\rangle.
\tag{3.6}
$$

Therefore, the second step of scissor correction is that the momentum matrices used to calculate the current and the coupling to the $\boldsymbol{A}$ field are scaled by a factor $(\epsilon_{\alpha\beta} + \Delta)/\epsilon_{\alpha\beta}$. The modified momentum matrix element connecting unoccupied and occupied states, $\tilde{\boldsymbol{P}}_{\alpha\beta}$, is given by

$$
\tilde{\boldsymbol{P}}_{\alpha\beta} = \frac{\epsilon_{\alpha\beta} + \Delta}{\epsilon_{\alpha\beta}}\boldsymbol{P}_{\alpha\beta},
\tag{3.7}
$$

where $\epsilon_{\alpha\beta}$ is the energy difference between Kohn-Sham state α and β. One can also see the problem in the view of perturbation theory[50]. The imagery part of dielectric function of a scissor-corrected Hamiltonian would be[50]

$$\varepsilon_{ab}^{"}(\omega) = 4\pi^2 \int_{BZ} \frac{d^3k}{8\pi^3} \sum_{\alpha,\beta} f_{\alpha,\beta} \frac{P_{\alpha\beta}^a(\boldsymbol{k})P_{\beta\alpha}^b(\boldsymbol{k})}{(\epsilon_{\alpha\beta}(\boldsymbol{k})+\Delta)^2} \delta(\epsilon_{\alpha\beta}(\boldsymbol{k})+\Delta-\omega), \qquad (3.8)$$

where $f_{\alpha,\beta} = f_\alpha - f_\beta$ and f_α is the occupation factor taken to be one for occupied states and zero for unoccupied states. Since the scissor operator shifts peaks by Δ without modifying the orbitals, the momentum matrix elements are identical to the original Hamiltonian without scissor correction. We immediately find that the scissor-corrected dielectric function $\varepsilon^{"}(\omega)$ is downscaled by $\left(\frac{\epsilon_{\alpha\beta}}{\epsilon_{\alpha\beta}+\Delta}\right)^2$ and violates the f-sum rule. It is worth to mention that Levine and Allan[51] pointed out that the scissor correction is an additional self-energy term which leads to a Ward-identity replacement of momentum operator as Eq. (3.7). This scaling factor would directly affect the value of current density $\boldsymbol{J}(t)$. Only with both these corrections will the optical spectra calculated via real-time propagation match the rigidly shifted spectra calculated in the linear response regime.

4.   Born Effective Charges from Ehren-fest Dynamics

4.1   Born Effective Charges

The definition of the Born effective charge (BECh) is the coefficient of proportion-ality of the change of macroscopic polarization P_α^{mac} in the direction of α and the displacement $u_{\mu,\beta}$ of nucleus μ along direction β in the absence of electric field $\boldsymbol{E}$:

$$Z_{\mu,\alpha\beta}^* = \Omega \frac{\partial P_\alpha^{\mathrm{mac}}}{\partial u_{\mu,\beta}}\bigg|_{\boldsymbol{E}=0}, \tag{4.1}$$

As illustrated in Fig. 4.1, if a cation of an ionic crystal carrying the positive charge of Z_α^+ is displaced by u without perturbing the system, then the Born effective charge is simply Z_α^+. However, when the cation is displaced, it perturbs the system and drags the electrons away from their original positions inducing polarization of electrons. We thus separate the typical definition of Born effective charge tensor $Z_{\mu,\alpha\beta}^*$ into two parts:

$$Z_{\mu,\alpha\beta}^* = Z_\mu \delta_{\alpha\beta} + \Omega \frac{\partial P_\alpha}{\partial u_{\mu,\beta}}\bigg|_{\boldsymbol{E}=0}, \tag{4.2}$$

where $Z_\mu \delta_{\alpha\beta}$ and $\Omega \frac{\partial P_\alpha}{\partial u_{\mu,\beta}}\big|_{\boldsymbol{E}=0}$ are the contributions from nuclei and electrons, respec-tively. If we rigidly move the whole solid adiabatically, the macroscopic polarization
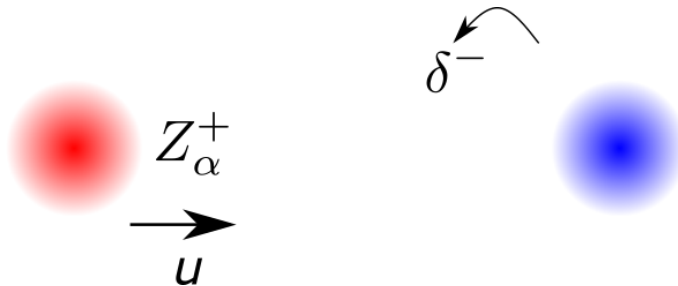
Figure 4.1
Illustration of the Born effective charge.

should not be generated, i.e. ,$\Delta \boldsymbol{P}^{\mathrm{mac}} = 0$. This leads to the acoustic sum rule[52]:

$$\sum_\mu Z^*_{\mu,\alpha\beta} = 0. \tag{4.3}$$

This is an important property that is preserved by the Born effective charges of insulators in general. The Born effective charge can be defined in an alternative way. Considering a system in the presence of a static electric field, the energy of the system which is a function of external electric field $\boldsymbol{E}$ is given by:

$$\mathcal{E}(\boldsymbol{E}) = \mathcal{E}_0 - \Omega \boldsymbol{P}^{\mathrm{mac}} \cdot \boldsymbol{E}. \tag{4.4}$$

Taking the derivative with respect to the electric field, we have

$$\frac{\partial \mathcal{E}}{\partial E_\alpha} = -\Omega P^{\mathrm{mac}}_\alpha, \tag{4.5}$$

where α labels the coordinate. Substituting the definition in Eq. (4.1), we find

$$Z^*_{\mu,\alpha\beta} = -\frac{\partial^2 \mathcal{E}}{\partial E_\alpha \partial u_{\mu,\beta}} = \frac{\partial F_{\mu,\beta}}{\partial E_\alpha}. \tag{4.6}$$

The second definition of BECh is equivalent to the change in the electrostatic force $F_{\mu,\beta}$ on a nucleus μ with respect to an external static electric field E_α. The BECh is important particularly for the studies of the LO-TO splitting. Such importance can be demonstrated by the dielectric permittivity. X. Gonze and C. Lee[53] showed that one has to include the response of the ions in the calculation of the low-frequency dielectric permittivity. The ionic contribution to the dielectric permittivity in the direction of $\boldsymbol{q}$ is given by

$$\epsilon^{\mathrm{ion}}_{\boldsymbol{q}}(\omega) = \frac{4\pi}{\Omega} \sum_m \frac{|\boldsymbol{Z}^*_m \cdot \boldsymbol{q}|^2}{\omega^2_m - \omega^2} \left(\sum_{\kappa\beta} [U_{m\boldsymbol{q}=0}(\kappa\beta)]^* \, U_{m\boldsymbol{q}=0}(\kappa\beta) \right), \tag{4.7}$$

where m labels the phonon mode, $U_{m\boldsymbol{q}}$ is the eigen-displacements of a dynamical matrix, κ is the label for atoms while β is the Cartesian coordinate. Eq. (4.7) shows that if the direction of Z^*_m is perpendicular to the direction of $\boldsymbol{q}$, this mode does not give contribution to the permittivity along $\boldsymbol{q}$. These modes that are in perpendicular direction are referred to as transverse modes. On the other hand, modes in the same direction of $\boldsymbol{q}$ that contribute to the permittivity are referred to as longitudinal modes. This gives rise to the distinction of LO mode and TO modes in solids.

4.2 Dynamical Born Effective Charges

Dynamical Born Effective Charges[54]
Chung-Yu Wang, S. Sharma, E. K. U. Gross, and J. K. Dewhurst
Published on *Phys. Rev. B 106, L180303 (2022)*

Dynamical Born effective charges

C.-Yu Wang [1,2] S. Sharma [3] E. K. U. Gross [2] and J. K. Dewhurst [1,*]

[1]*Max-Planck-Institut für Mikrostrukturphysik, Weinberg 2, D-06120 Halle, Germany*
[2]*Fritz Haber Center for Molecular Dynamics, Institute of Chemistry, The Hebrew University of Jerusalem, Jerusalem 91904, Israel*
[3]*Max-Born-Institute for Nonlinear Optics and Short Pulse Spectroscopy, Max-Born Strasse 2A, 12489 Berlin, Germany*

We extend the definition of the Born effective charge to the dynamical regime. This is equal to the Fourier transform of the total electronic current divided by the Fourier transform of the velocity of a particular nucleus. The usual static Born effective charges are recovered in the zero-frequency limit. We calculate these charges for a selection of materials using time-dependent density functional theory in an all-electron code where the nuclei move along a chosen trajectory. A rich response function emerges with prominent resonance peaks. The finite value for the Born effective charge of metals is also reproduced. The dynamical Born effective charges are thus a natural choice of observable for probing the fundamental nonadiabatic coupling of electrons and nuclei.

I. INTRODUCTION

The Born effective charge (BEC) is a useful and precisely defined quantity for both molecules and solids and one which can be both readily calculated and experimentally measured [1,2]. There are two equivalent definitions for the BEC: The first is the change in the electrostatic force $\mathbf{F}_\alpha$ on a nucleus α with respect to an external electric field $\mathbf{E}$,

$$Z^*_{\alpha ij} \equiv -\frac{\partial F_{\alpha i}}{\partial E_j}, \qquad (1)$$

where i and j label Cartesian directions. The second, equivalent definition of the BEC is the change in the electric polarization of the system with respect to an infinitesimal displacement of a nucleus,

$$Z^*_{\alpha ij} \equiv Z_\alpha \delta_{ij} + \frac{\partial P_i}{\partial u_{\alpha j}}, \qquad (2)$$

where Z_α is the nuclear charge, $\mathbf{P}$ is the electronic polarization, and $\mathbf{u}_\alpha$ is the displacement away from equilibrium. (We will follow the convention of taking the electronic charge e as $+1$ and the nuclear charges as negative.) For a finite system, the electronic polarization can be calculated using

$$\mathbf{P} = \int d^3r\, \rho(\mathbf{r})\mathbf{r}, \qquad (3)$$

where ρ is the electronic charge density. For charge-neutral systems, the total polarization (one which includes the contribution from the nuclear charges) is independent of the choice of origin. On the other hand, the polarization of charge-neutral systems with periodic boundary conditions cannot be uniquely determined from Eq. (3). Instead, only the change in $\mathbf{P}$ can be calculated as a function of some parameter such as the external electric field or an atomic displacement [3–8].

This parameter may be made time dependent and the change in polarization determined from the adiabatic limit of the integrated electronic current. Let $\lambda(t)$ be the parameter as a function of time t and suppose that $\mathbf{J}(t)$ is the induced current. Then the change in polarization is given by

$$\Delta\mathbf{P} = \int_0^T dt\, \mathbf{J}(t). \qquad (4)$$

The adiabaticity or "slowness" of the process is usually captured by representing the time dependence of the parameter by setting $\lambda(t) = f(t/T)$ with a function f which is bounded in the interval [0,1]. The adiabatic limit is then obtained by taking $T \to \infty$. It was shown by King-Smith and Vanderbilt [5] that the change in polarization is closely related to the Berry phase [9], and we will refer to their algorithm for calculating the static BEC as the "Berry phase method."

In its basic definition, the BEC is a static quantity evaluated from the adiabatic limit of the current. However, this definition can be easily and naturally extended to the nonadiabatic case in which the nucleus is moving at finite velocity along a prescribed path. The electronic current will respond accordingly and its frequency components can be determined. For what follows, we will restrict our attention to solids and also assume a noninteracting system of electrons in an effective Kohn-Sham [10,11] potential within the framework time-dependent density functional theory (TDDFT) [12].

Now choose $\lambda(t)$ to be the time-dependent displacement of nucleus α away from equilibrium $\mathbf{u}_\alpha(t)$, with $\mathbf{v}_\alpha(t) = \partial\mathbf{u}_\alpha(t)/\partial t$ as its velocity. The time-dependent total electronic current across a unit cell is given by

$$\mathbf{J}(t) = \frac{1}{N_k} \sum_{i\mathbf{k}}^{\mathrm{occ}} \int d^3r\, \mathrm{Im}[\varphi^*_{i\mathbf{k}}(\mathbf{r},t)\nabla\varphi_{i\mathbf{k}}(\mathbf{r},t)], \qquad (5)$$

where $\varphi_{i\mathbf{k}}$ is the ith Kohn-Sham state at a particular k point in a set of N_k points, the sum is over the occupied states, and the integral is over the unit cell. We define the *dynamical Born*

effective charge (dynBEC) as a natural extension of Eq. (2),

$$Z^*_{\alpha ij}(\omega) \equiv Z_\alpha \delta_{ij} + \frac{\partial J_i(\omega)}{\partial v_{\alpha j}(\omega)}, \qquad (6)$$

where

$$\mathbf{J}(\omega) \equiv \int_0^\infty dt\, \mathbf{J}(t) \exp[i(\omega + i\eta)t] \qquad (7)$$

is the Fourier transform of the current, $\mathbf{v}_\alpha(\omega)$ the Fourier transform of the velocity, and η is a positive infinitesimal. Note that $\Delta\mathbf{P} = \Delta\mathbf{J}(\omega \to 0)$ and that the acoustic sum rule [13],

$$\sum_\alpha Z^*_{\alpha ij}(\omega \to 0) = 0, \qquad (8)$$

is satisfied in the static limit owing to charge neutrality, although this is not true in general for all frequencies. This property is a useful indicator for establishing the quality of the numerical calculations.

The optical conductivity σ_{ij} can be calculated in the same manner from the current and the electric field,

$$\sigma_{ij}(\omega) = \frac{1}{\Omega} \frac{\partial J_i(\omega)}{\partial E_j(\omega)}, \qquad (9)$$

where Ω is the unit cell volume, which implies that $\mathbf{u}_\alpha(t)$ is the analog of the vector potential $\mathbf{A}(t)$ and $\mathbf{v}_\alpha(t)$ is the analog of the electric field $\mathbf{E}(t) = -(1/c)\partial\mathbf{A}(t)/\partial t$.

Recently, the frequency-dependent generalization of the BEC was defined independently by Binci *et al.* [14] and Dreyer *et al.* [15]. However, in these works, $Z^*(\omega)$ was evaluated either at phonon frequencies or in the zero-frequency limit. In our work, we explore this quantity over an energy range from zero up to ~100 eV.

II. IMPLEMENTATION

We implemented the dynBEC in the solid-state, all-electron code ELK [16] which uses linearized augmented plane waves (LAPWs) as a basis [17]. This basis depends parametrically on the nuclear coordinates, which complicates the time evolution of the combined electronic and nuclear systems. Let V_{ext} be the external potential consisting of the Coulomb potential of the bare nuclei. Rather than explicitly moving the nuclei, we instead modify the external potential with

$$V_{\text{ext}}(\mathbf{r}, t) = V_{\text{ext}}(\mathbf{r}) - \mathbf{u}_\alpha(t) \cdot \nabla_\alpha V_{\text{ext}}(\mathbf{r}), \qquad (10)$$

where ∇_α is the derivative with respect to the displacement $\mathbf{u}_\alpha$. This approach is only valid for small displacements of the nuclei and, in fact, our investigation into the BEC began as a means of evaluating the validity of this approximation. In practice, we also add the derivative of the Coulomb (i.e.,

Hartree) potential of the core electrons, which are not included in the TDDFT dynamics, under the assumption that the core electrons move rigidly with the nuclei and serve to screen the Coulomb potential of the nuclei. Note that, in principle, the contribution from the exchange-correlation potential of the core electrons should be included in the gradient of the potential in Eq. (10). However, owing to the nonlinearity of the exchange-correlation potential with respect to the density, it is not possible to uniquely extract that part of the potential which arises from the core electrons alone. We discovered, however, that this contribution to the gradient had a negligible effect on the results and chose instead to omit it.

The real-time dynamics were performed using a scheme in which the time-dependent Kohn-Sham orbitals are expanded in the eigenvectors of the instantaneous Hamiltonian and propagated using phase factors over a small time interval [18].

The dynBEC as defined in Eq. (6) is independent of the choice of path. This is because of the linearity of response functions in general: One can apply an atomic displacement either of a single frequency or multiple frequencies together. Both will yield the same response function because the frequency response decouples in the linear regime. The choice of frequencies and their amplitudes defines a particular path in time and, because we divide by the velocity in Eq. (6), the dynBEC is independent of this choice. The only proviso is that any path should contain a nonzero component from each frequency.

For convenience, we choose an *instantaneous displacement* at $t = 0$. The corresponding velocity is therefore a δ function in time whose Fourier transform is a constant. This removes the need to divide by $v_{\alpha j}(\omega)$ in Eq. (6) and thus eliminates a source of numerical error. It is important to note that the dynBEC is part of the general response function,

$$\chi(\mathbf{r}, \mathbf{r}', t - t') \equiv \frac{\delta\rho(\mathbf{r}, t)}{\delta V_{\text{ext}}(\mathbf{r}', t')}. \qquad (11)$$

In our case, we take δV_{ext} to be the change in external potential caused by the displacement of a nuclei given in Eq. (10). One may ask whether the Kohn-Sham system which reproduces the exact density also yields the exact total current, as required by Eq. (6). In general, the first-order response of the macroscopic current $\delta\mathbf{J}$ is exact even though the Kohn-Sham current density $\mathbf{j}(\mathbf{r})$ is not [19]. This is a consequence of the continuity equation applied to the long-range response of the density (see, also, Eqs. (1.20), (A2), and (A3) of Ref. [20]). Thus, TDDFT is sufficient for calculation of the dynBEC for periodic systems.

The full response function can be evaluated from the Kohn-Sham response function χ_s using the Dyson equation in frequency space [21],

$$\chi(\mathbf{r}, \mathbf{r}', \omega) = \chi_s(\mathbf{r}, \mathbf{r}', \omega) + \int d^3r_1\, d^3r_2\, \chi_s(\mathbf{r}, \mathbf{r}_1, \omega)\left[\frac{1}{|\mathbf{r}_1 - \mathbf{r}_2|} + f_{\text{xc}}(\mathbf{r}_1, \mathbf{r}_2, \omega)\right]\chi(\mathbf{r}_2, \mathbf{r}', \omega), \qquad (12)$$

where f_{xc} is the exchange-correlation kernel. We can write the change in total electronic current corresponding to the Kohn-Sham response function explicitly as follows [6,15,22–24]:

$$\frac{\partial\mathbf{J}_s(\omega)}{\partial v_{\alpha j}(\omega)} = \frac{i}{\omega} \sum_{\mathbf{k}} \sum_i^{\text{occ}} \sum_j^{\text{unocc}} \left[\frac{\langle\varphi_{i\mathbf{k}}|\hat{\mathbf{p}}|\varphi_{j\mathbf{k}}\rangle\langle\varphi_{j\mathbf{k}}|\partial\hat{V}_{\text{ext}}/\partial u_{\alpha j}|\varphi_{i\mathbf{k}}\rangle}{\varepsilon_{j\mathbf{k}} - \varepsilon_{i\mathbf{k}} + \omega + i\eta} + \text{c.c.}(\omega \to -\omega)\right]. \qquad (13)$$
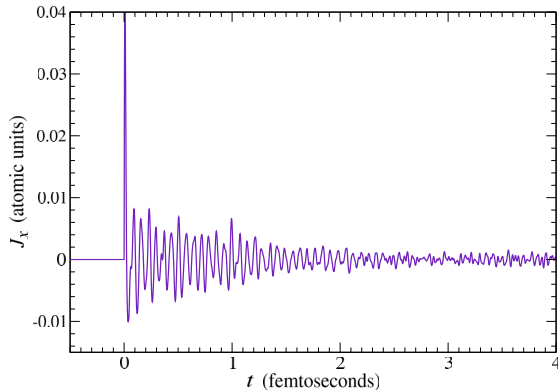
FIG. 1. Time-dependent electronic current across a single unit cell of LiF after a small, instantaneous displacement of the Li nucleus in the x direction at $t = 0$. The total simulation time was 19.4 femtoseconds.

This formula does not, however, include the self-consistent change in the Kohn-Sham potential arising from the change in density. To incorporate this effect, the full Kohn-Sham response function χ_s should be calculated and then used in Eq. (12) along with f_{xc}. Our approach of performing a real-time TDDFT is equivalent to this, but numerically more convenient. This is because solving the Dyson equation with sufficient spatial resolution for the derivative of the Coulomb potential in Eq. (10) would be prohibitively expensive for an all-electron method.

III. RESULTS

The code was used to find the dynBEC of the ionic polar insulators LiH, LiF, and LiCl, the covalently bonded BN in both the cubic and hexagonal phases, the nonpolar insulator diamond, and the fcc metal Al. The materials were chosen to demonstrate some distinct characteristics of the dynBEC and, because their constituent atoms are fairly light, lessen the computational expense. In Fig. 1, we plot the current generated by instantaneously displacing the Li nucleus at $t = 0$ in LiF. This is typical of the behavior of the current obtained for all the materials and nuclei, namely, a large initial spike in current followed by rapid and varied oscillations. In the
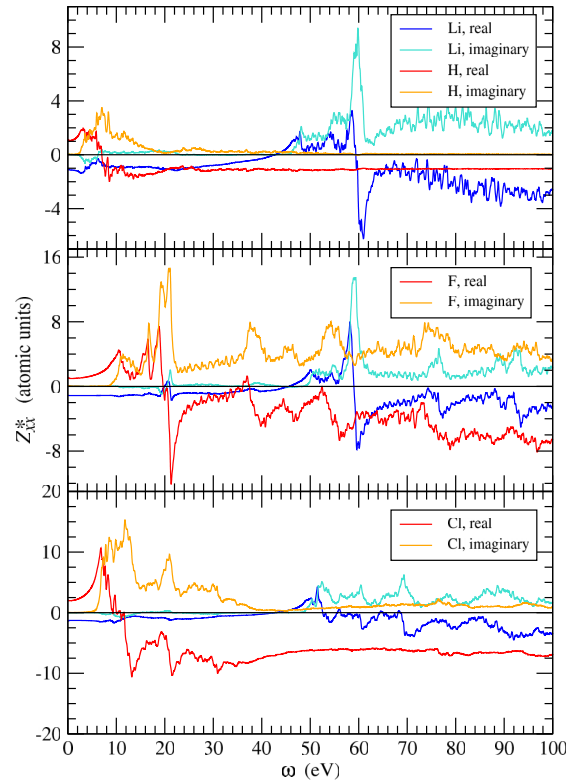

FIG. 2. Dynamical Born effective charges of LiH (top), LiF (center), and LiCl (bottom).

case of Li, the amplitude of the oscillations decreased until around 3 femtoseconds and then reached a "steady state." Total simulation time for all our calculations was 800 atomic units of time, or 19.4 femtoseconds. Each time step for the simulations was 1.2 attoseconds. This current was then numerically Fourier transformed with η in Eq. (7) taken to be 0.136 eV (except in the case of Al, where various values were tested). The static BEC results for all the materials are collated in Table I.

The dynBEC of the ionic compounds LiH, LiF, and LiCl is plotted in Fig. 2. This is a complex quantity and so the

TABLE I. Static Born effective charges of various materials calculated from the $\omega \to 0$ of the dynBEC compared to those calculated with the Berry phase method and experiment. The units of charge are e, i.e., the electronic charge. The value in parentheses is the average of the two absolute values.

		Experiment	Berry [5,16]	$Z^*(\omega \to 0)$		
LiH		0.991 [26,27]	1.04	Li: -1.03	H: 1.13	(1.08)
LiF		1.045 [27,28]	1.05	Li: -1.11	F: 1.12	(1.11)
LiCl		1.231 [27,28]	1.18	Li: -1.35	Cl: 2.06	(1.70)
cubic BN		1.98 [29,30]	1.89	B: -1.57	N: 1.97	(1.77)
hexagonal BN	x		2.72	B: -2.28	N: 3.05	(2.67)
	z		0.75	B: -0.44	N: 1.07	(0.76)
Al				-2.09		
diamond				-0.15		
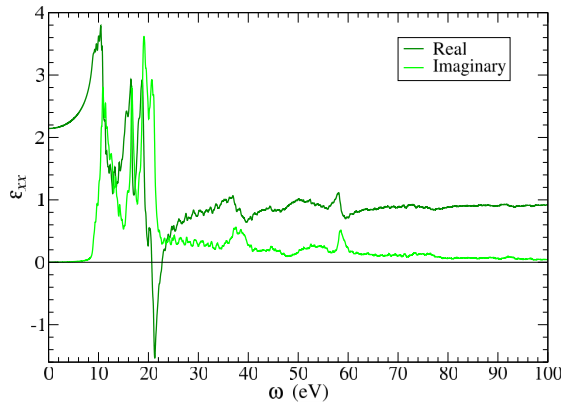
FIG. 3. Dielectric function of LiF calculated within the RPA.

FIG. 4. Dynamical Born effective charges of cubic BN.

real and imaginary parts are plotted separately. In the limit as $\omega \to 0$, the real part of the dynBEC tends to the regular static BEC, although the acoustic sum rule, given by Eq. (8), is not perfectly satisfied. This may be due to the incompleteness of the LAPW basis, particulary when expanding the change in wave function owing to an atomic displacement simulated with Eq. (10). The error can be reduced by increasing the size of the basis used for the time evolution of the Kohn-Sham orbitals, but ultimately becomes numerically unfeasible. The best case is that of LiF (Li: -1.11, F: 1.12) and the worst is LiCl (Li: -1.35, Cl: 2.06). However, the sum rule itself can be used to partially correct this error by taking an average of absolute values for our two atom systems.[1] The resulting charges are then in good agreement with the Berry phase method and experiment. An exception is that of LiCl for which the BEC of Li is in relatively good agreement with that of the Berry phase method, however the value for Cl is too large. This gives an average value of 1.70, which is over 40% greater than it should be. Unfortunately, we were unable to converge this calculation any further.

The dynBEC of the covalently bonded boron nitride in both the cubic and hexagonal phases is shown in Figs. 4 and 5. The zero-frequency limit gave good agreement for the static BEC with that of the Berry phase method and, for the cubic case, experiment. Notably, the BEC for the x and z directions of hBN are significantly different and yet the two methods are in excellent agreement for both. Diamond, which is also covalently bonded but not a polar semiconductor, should give a BEC of zero. Our result for the zero-frequency limit of the dynBEC is -0.15. This slight discrepancy may again be due to the limitation of the LAPW basis.

The metallic case is the most interesting as far as the static limit is concerned. Until recently, it was assumed that the BEC for metals was undefined. However, Dreyer *et al.* [15]

showed that this is not the case and demonstrated that there is a nonadiabatic version of the BEC for metals and related it to the Drude weight. The dynBEC of Al for small frequencies is plotted in the inset of Fig. 7. One can see that the value taken for η affects the $\omega \to 0$ limit. There are noticeable oscillations in the plots calculated with small values of η. For comparison, the dielectric function ϵ_{xx}, calculated within the random phase approximation (RPA), is plotted in Fig. 8 with and without the intraband term [25]. Using the same k-point set as that for the dynBEC ($42 \times 42 \times 42$), the oscillations in ϵ_{xx} mirror those in the dynBEC. A much denser set ($72 \times 72 \times 72$) removes the oscillations in the dielectric function, indicating that they are merely an artifact of a finite k-point grid. These oscillations can be suppressed either by increasing the number of k points or increasing the value of η. We find that taking $\eta = 0.544$ eV smooths the curve sufficiently without distorting the data. Using this value for η, our prediction for the nonadiabatic

FIG. 5. Dynamical Born effective charges of hexagonal BN for the x and z directions.

---

[1]The static BEC determined from the Berry phase method could be used to further correct numerical inaccuracies in the dynBEC by adding a real constant to $Z^*(\omega)$ so that the two methods are in agreement at $\omega = 0$. The imaginary part of the dynBEC could then be calculated using a Kramers-Kronig transformation.
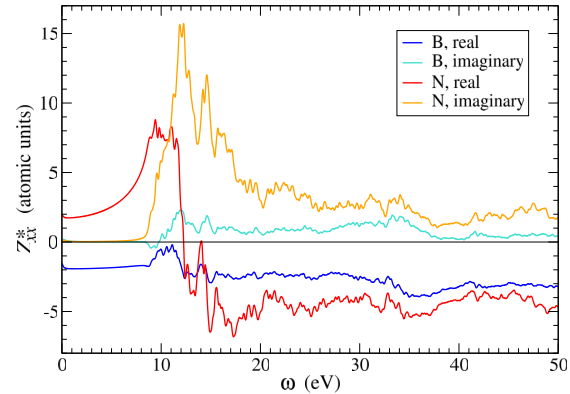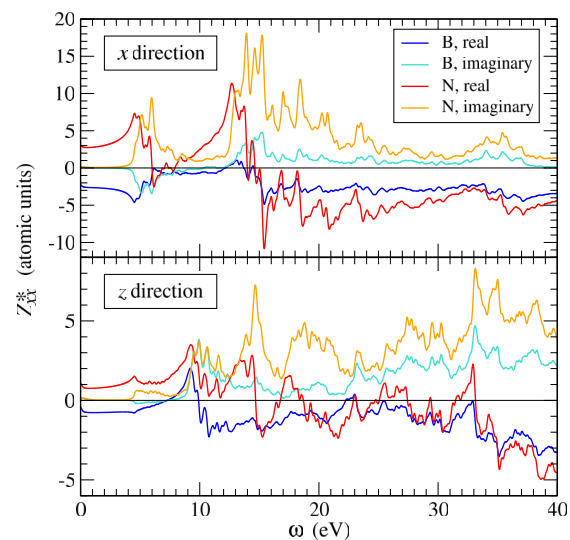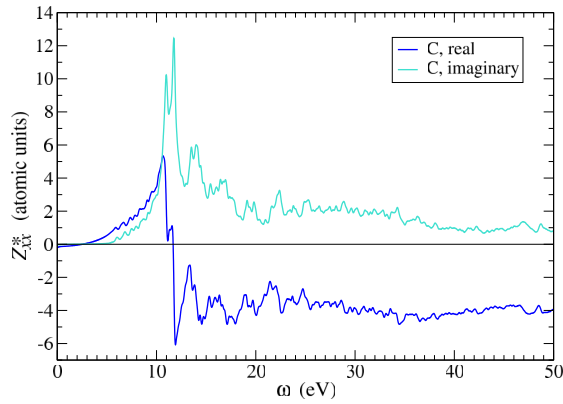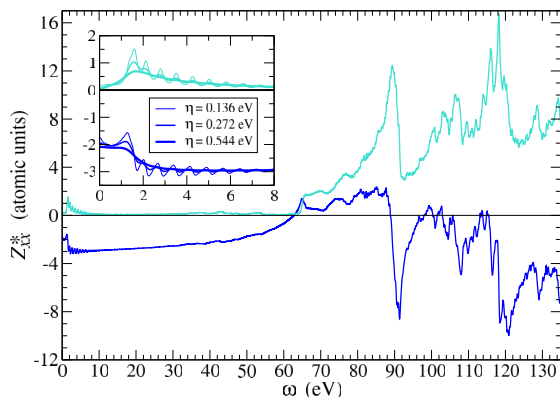
FIG. 6. Dynamical Born effective charges of diamond.

BEC is -2.09, which is in excellent agreement with the value of -2.0 determined by Dreyer *et al.*

At finite frequencies, the dynBEC spectral functions of each atom are very different. In the case of LiX, the imaginary part of the dynBEC for Li is zero until about 50 eV, whereas the onset for H, F, and Cl is much lower, ranging from 3 to 8 eV. There are also several prominent resonant peaks. In LiH and LiF, a clear resonance in the Li part of the spectrum can be seen around 60 eV. At this point, the real part crosses the zero axis and the imaginary part has a sharp peak. This peak corresponds to a transition between the Li $1s$ and $2p$ orbitals. It is almost completely absent in LiCl because the $2p$ state is considerably more hybridized. Aside from the conspicuous resonances, the Li dynBEC is noticeably dissimilar for the three compounds throughout the entire range of frequencies, despite the fact that the materials have the same crystal structure and same type of bonding. This suggests that the dynBEC is highly sensitive to the chemical environment of the selected atom.

There are also axis crossings of the real part of the dynBEC for H, F, and Cl. The corresponding peaks in the imaginary parts are not as well defined as those for Li. The most pronounced is that of F with a resonance around 20 eV.

FIG. 7. Dynamical Born effective charge of Al. The inset shows the low-frequency behavior of the dynBEC for three different values of η used in Eq. (7).
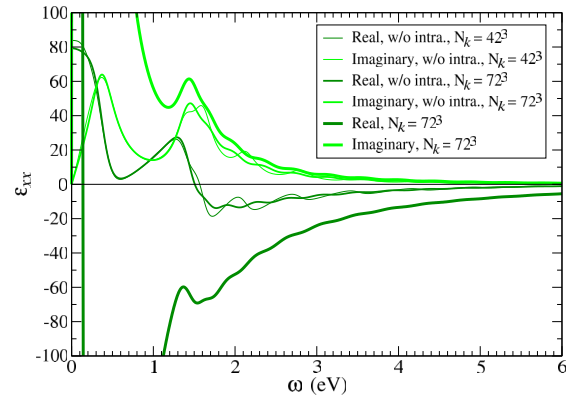
FIG. 8. Dielectric function of Al calculated within the RPA. The plot contains ϵ_{xx} with and without the intraband "Drude" term. Also included is the dielectric function calculated on the same k-point grid as that used for the dynBEC calculation.

Comparing the dynBEC of LiF to its dielectric function in Fig. 3 reveals similarity in the positions of the most prominent peaks, particularly for lower energies (<20 eV) and for the fluorine part. This is not surprising because peak positions are largely dictated by the denominator in the noninteracting response function given by Eq. (13). What is different are the relative weights of the peaks owing to the difference in the matrix elements in the numerator. Furthermore, the dynBEC retains its relative amplitude even for high energies where ϵ_{xx} has tapered off. The reason is that δV_{ext} acts more strongly on orbitals bound closely to the nuclei than does a spatially constant external electric field. Thus, higher-energy excitations will have higher weights for the dynBEC.

Turning to the finite-frequency dynBEC of the covalently bonded materials BN and diamond as shown in Figs. 4–6, we observe similarly intricate spectra. The peaks are generally broader, indicating increased hybridization between the atomic orbitals. Also noteworthy is the similarity of the dynBEC spectra of cBN and diamond at finite frequency, even though the static BECs are very different for these materials. Of particular significance is the distinction between the dynBEC for the x and z directions of hexagonal BN. Thus, not only does the dynBEC discriminate between different atoms, but also different directions.

Lastly, for the case of Al in Fig. 7, the spectrum is fairly featureless until 64 eV when there is a crossing of the axis by the real part and an onset of the imaginary part. After this, there are several prominent peaks in the spectrum, particularly at about 90 and 118 eV. Compared to the dielectric function in Fig. 8 in which ϵ_{xx} diverges because of the intraband term, the dynBEC is finite at $\omega = 0$. Thus, if the dynBEC can be measured experimentally, it should more suited than the dielectric function to resolve low-frequency features in the response function of metals.

IV. SUMMARY

We have extended the definition of the Born effective charge to a dynamical, frequency-dependent variant. This was

calculated using an instantaneous displacement of a nucleus and then performing a Fourier transformation of the resulting electronic current computed with TDDFT. The dynBEC is a natural extension to the regular static BEC and we anticipate that it may be measurable with neutron diffraction techniques [31]. Unlike the dielectric function, the dynBEC discriminates between atoms in the solid and thus is intimately connected to nonadiabatic coupling between nuclei and electrons. In effect, it quantifies the amount of electronic charge "dragged" along with a nucleus, when that nucleus is moving back and forth at a given frequency.

The primary utility of having an accurate experimental measurement of the dynBEC would be to determine any error in the theoretical prediction. Such a deviation would be due almost entirely to the approximation of the TDDFT kernel f_{xc} used in Eq. (12). For instance, the closely related dielectric function suffers from significant error for excitonic materials [32]. In these cases, the resonant excitonic peaks are not captured by the usual adiabatic approximations to f_{xc} and considerable theoretical effort has been expended in producing functionals which do work [33,34]. Are there similar limitations to using the adiabatic functionals for the prediction of the dynBEC? Comparison to experiment should be able to answer this and ultimately aid in the development of TDDFT functionals for the case of combined electron and nuclear dynamics [35]. Another potential use would be to improve first-principles calculations of ion stopping in condensed matter, particularly in the energy range of up to a few-hundred electron volts [36,37]. In this regime, so-called nuclear stopping dominates in which the ions' kinetic energy is primarily transferred to the nuclei. The dynBEC could quantify how much of this energy is subsequently absorbed by excitation of electronic currents. Lastly, molecular dynamics calculations within the adiabatic approximation but driven by a laser pulse given by a vector potential $\mathbf{A}(t)$ could utilize the dynBEC for determining the contribution to the force on each atom by the laser. The electric field is given by $\mathbf{E}(t) = -(1/c)d\mathbf{A}/dt$ and the force on atom α would be modified by $\mathbf{F}_\alpha(t) \rightarrow \mathbf{F}_\alpha(t) - Z_\alpha^* \mathbf{E}(t)$. The choice of the matrix Z_α^* as the effective charge which couples to the electric field arises from Eq. (1). However, with the dynamical BEC, one could match Z_α^* to the laser frequency, i.e., choose $Z_\alpha^*(\omega_{laser})$ instead of $Z_\alpha^*(0)$, which should be the better choice in this situation.

[1] M. Born and K. Huang, *Dynamical Theory of Crystal Lattices*, International Series of Monographs on Physics (Clarendon Press, Oxford, 1954).

[2] J. D. Axe, Phys. Rev. **157**, 429 (1967).

[3] S. Baroni, P. Giannozzi, and A. Testa, Phys. Rev. Lett. **58**, 1861 (1987).

[4] X. Gonze, D. C. Allan, and M. P. Teter, Phys. Rev. Lett. **68**, 3603 (1992).

[5] R. D. King-Smith and D. Vanderbilt, Phys. Rev. B **47**, 1651 (1993).

[6] R. Resta, Rev. Mod. Phys. **66**, 899 (1994).

[7] X. Gonze and C. Lee, Phys. Rev. B **55**, 10355 (1997).

[8] R. Resta and D. Vanderbilt, Theory of polarization: A modern approach, in *Physics of Ferroelectrics: A Modern Perspective*, edited by C. H. Ahn, J.-M. Triscone, and K. M. Rabe (Springer, Berlin, Heidelberg, 2007), pp. 31–68.

[9] M. V. Berry, Proc. R. Soc. London A **392**, 45 (1984).

[10] P. Hohenberg and W. Kohn, Phys. Rev. **136**, B864 (1964).

[11] W. Kohn and L. J. Sham, Phys. Rev. **140**, A1133 (1965).

[12] E. Runge and E. K. U. Gross, Phys. Rev. Lett. **52**, 997 (1984).

[13] R. M. Pick, M. H. Cohen, and R. M. Martin, Phys. Rev. B **1**, 910 (1970).

[14] L. Binci, P. Barone, and F. Mauri, Phys. Rev. B **103**, 134304 (2021).

[15] C. E. Dreyer, S. Coh, and M. Stengel, Phys. Rev. Lett. **128**, 095901 (2022).

[16] The Elk Code, http://elk.sourceforge.net/.

[17] D. Singh and L. Nordstrom, *Planewaves, Pseudopotentials, and the LAPW Method* (Springer, New York, 2006).

[18] J. Dewhurst, K. Krieger, S. Sharma, and E. Gross, Comput. Phys. Commun. **209**, 92 (2016).

[19] R. D'Agosta and G. Vignale, Phys. Rev. B **71**, 245103 (2005).

[20] S. L. Adler, Phys. Rev. **126**, 413 (1962).

[21] M. Petersilka, U. J. Gossmann, and E. K. U. Gross, Phys. Rev. Lett. **76**, 1212 (1996).

[22] F. Kootstra, P. L. de Boeij, and J. G. Snijders, J. Chem. Phys. **112**, 6517 (2000).

[23] F. Kootstra, P. L. de Boeij, and J. G. Snijders, Phys. Rev. B **62**, 7071 (2000).

[24] P. Romaniello and P. L. de Boeij, Phys. Rev. B **71**, 155108 (2005).

[25] M. Cazzaniga, L. Caramella, N. Manini, and G. Onida, Phys. Rev. B **82**, 035104 (2010).

[26] M. Brodsky and E. Burstein, J. Phys. Chem. Solids **28**, 1655 (1967).

[27] A. Shukla, Phys. Rev. B **61**, 13277 (2000).

[28] M. J. Sangster, R. M. Atwood, and U. Schroder, J. Phys. C **11**, 1523 (1978).

[29] J. A. Sanjurjo, E. López-Cruz, P. Vogl, and M. Cardona, Phys. Rev. B **28**, 4579 (1983).

[30] K. Shimada, T. Sota, and K. Suzuki, J. Appl. Phys. **84**, 4951 (1998).

[31] S. W. Lovesey, *Theory of Neutron Scattering from Condensed Matter* (Clarendon Press, Oxford, 1984).

[32] G. Onida, L. Reining, and A. Rubio, Rev. Mod. Phys. **74**, 601 (2002).

[33] S. Sharma, J. K. Dewhurst, A. Sanna, and E. K. U. Gross, Phys. Rev. Lett. **107**, 186401 (2011).

[34] Y.-M. Byun and C. A. Ullrich, Phys. Rev. B **95**, 205136 (2017).

[35] X. Li, J. C. Tully, H. B. Schlegel, and M. J. Frisch, J. Chem. Phys. **123**, 084106 (2005).

[36] P. Sigmund, Bull. Russ. Acad. Sci.: Phys. **72**, 569 (2008).

[37] M. Caro, A. A. Correa, E. Artacho, and A. Caro, Sci. Rep. **7**, 2618 (2017).

4.3   Appendix

Kramers-Kronig relation in dynamical Born effective charges

The Kramers-Kronig (K-K) relation is an important property because it reflects the causality through the analyticity of the linear response function on the upper half of the complex plane. It is also a useful relation in practice, for one can calculate the real part directly from the imaginary part of the response function and vice versa. Given a response function $\chi = \chi' + i\chi''$, the Kramers-Kronig relation of this response function is

$$
\begin{aligned}
\chi'(\omega) &= \frac{2}{\pi}\mathfrak{P}\int_0^\infty \frac{\omega'\chi''(\omega')}{\omega'^2 - \omega^2}d\omega' \\
\chi''(\omega) &= \frac{-2\omega}{\pi}\mathfrak{P}\int_o^\infty \frac{\chi'(\omega')}{\omega'^2 - \omega^2}d\omega',
\end{aligned}
\tag{4.8}
$$

where $\mathfrak{P}$ represents the principle value. We apply the K-K relation to verify that the dynamical Born effective charge (dynBECh) function computed from our method are indeed the response function. It is an important examination for real-time evolution. Displayed in Fig. 4.2, the response functioned label K-K is evaluated by K-K relation with the dynamical Born effective charge function of the Nitrogen in c-BN from our real-time approach. Both of the imaginary part and the real part of the dynamical Born effective charge function preserve the K-K relation thus indicating that the dynamical Born effective charge satisfies the analyticity property of a linear response function.
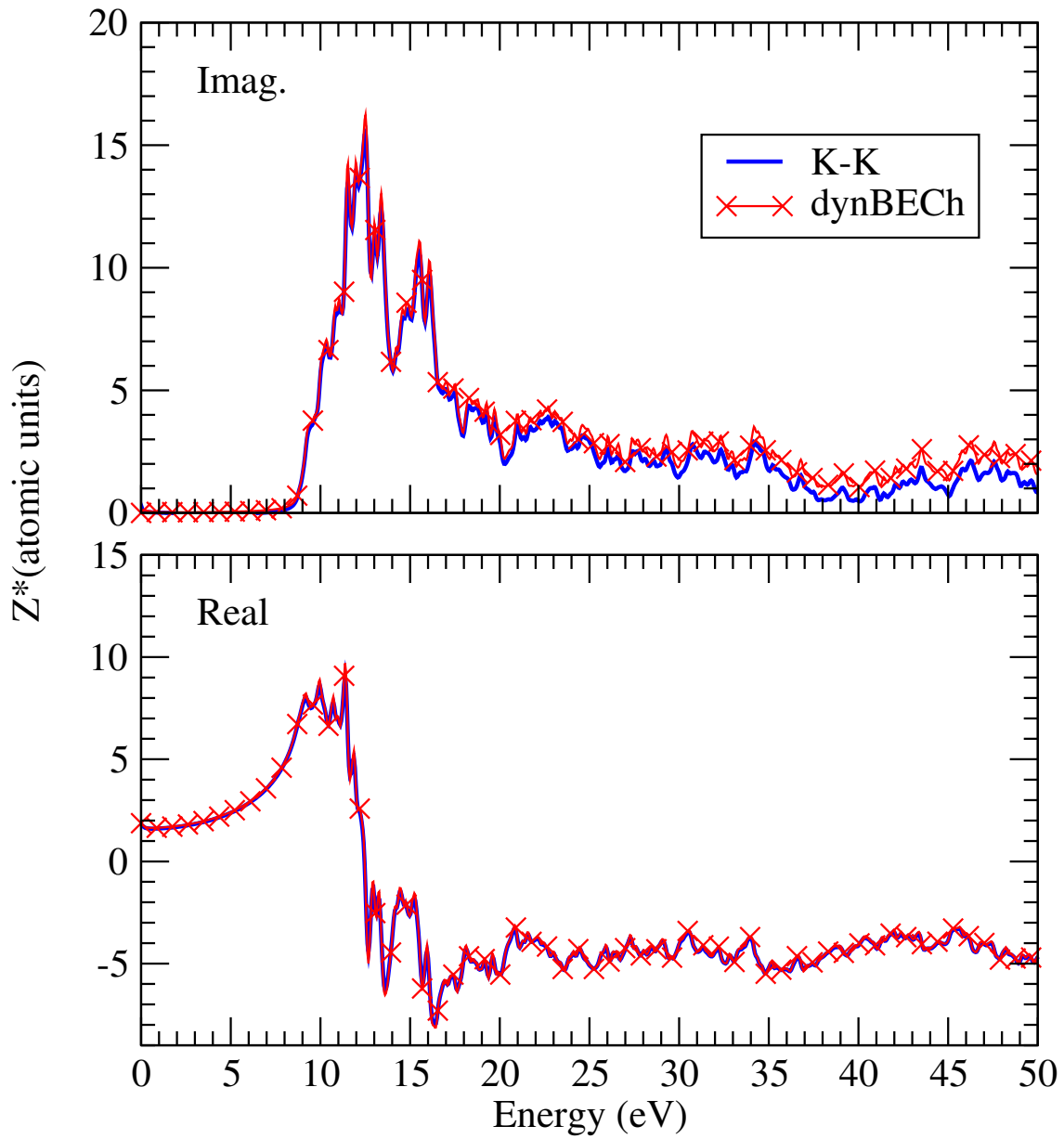
Figure 4.2
Kramers-Kronig relation of dynBECh of Nitrogen atom of c-BN.

5. Coupled Bogoliubov Equations for Electrons and Phonons

5.1 Coupled Bogoliubov equations for electrons and phonons

Coupled Bogoliubov equations for electrons and phonons[55]
Chung-Yu Wang, S. Sharma, T. Müller, E. K. U. Gross, and J. K. Dewhurst
Published on *Phys. Rev. B 105, 174509 (2022)*

Coupled Bogoliubov equations for electrons and phonons

C.-Yu Wang [1,2] S. Sharma [3] T. Müller,[1] E. K. U. Gross,[2] and J. K. Dewhurst [1,*]

[1]*Max-Planck-Institut für Mikrostrukturphysik, Weinberg 2, D-06120 Halle, Germany*
[2]*Fritz Haber Center for Molecular Dynamics, Institute of Chemistry, The Hebrew University of Jerusalem, Jerusalem 91904, Israel*
[3]*Max-Born-Institute for Non-linear Optics and Short Pulse Spectroscopy, Max-Born Strasse 2A, 12489 Berlin, Germany*

With the aim of including small amplitude quantum nuclear dynamics in solid-state calculations, we derive a set of equations by applying Wick's theorem to the square of the Fröhlich Hamiltonian. These are noninteracting fermionic and bosonic Hamiltonians with terms up to quadratic order in the field operators. They depend on one another's density matrices and are therefore to be solved self-consistently. A Bogoliubov transformation is required to diagonalize both the fermionic and bosonic Hamiltonians since they represent noninteracting quantum field theories with an indefinite number of particles. The Bogoliubov transform for phonons is non-Hermitian in the general case, and the corresponding time evolution is nonunitary. Several sufficient conditions for ensuring that the bosonic eigenvalues are real are provided. The method was implemented in an all-electron code and shown to correctly predict the renormalization of the Kohn-Sham band gap of diamond and silicon due to the electron-phonon interaction. The theory also verifies that niobium and MgB_2 are phonon-mediated superconductors and predicts the existence and magnitude of their superconducting gaps. Lastly, we confirm that copper is *not* a superconductor even at zero temperature.

I. INTRODUCTION

The adiabatic approximation is among the most fundamental ingredients of modern condensed-matter theory and quantum chemistry. It rests on the intuitive picture that the electrons, being much lighter than the nuclei, can instantaneously adjust to the nuclear positions. A two-step approach of first evaluating the Born-Oppenheimer (BO) potential energy surface [1–4] with electronic-structure methods and then solving the nuclear Schrödinger equation in terms of vibrational degrees of freedom is a standard procedure in the *ab initio* treatment of molecules and solids. The adiabatic approximation is crucial here because it leads to separate equations for the electronic and nuclear degrees of freedom, respectively. It is this separation that allows us to treat the electronic and nuclear many-body problems with very different methodologies. The adiabatic approximation not only makes computations feasible, it is deeply ingrained in the way we visualize the atomic and electronic structure of molecules and solids.

Yet some of the most fascinating phenomena in condensed matter physics and quantum chemistry live outside the realm of the adiabatic approximation. Prime examples are phonon-mediated superconductivity [5] or the process of vision [6]. The theoretical treatment of nonadiabatic phenomena is notoriously difficult because one is basically forced to go back to the full electron-nuclear Schrödinger equation.

In molecules, nonadiabaticity is mainly associated with transitions between different BO potential energy surfaces: If

a traveling nuclear wave packet reaches a conical intersection, i.e., a point where it is nearly or fully degenerate with another BO surface, then this can trigger the nuclear wave packet to split, leading to a significant population in both surfaces. Continuing its journey, the wave packet may split again when it encounters avoided crossings with other BO surfaces and, when returning, it may interfere with parts of itself. This rolling-around of nuclear amplitudes on BO surfaces is the essence of most photochemical and photophysical processes [7,8]. Sometimes the nuclear wave packet returns to where it started from, thus completing an optical cycle as found in the process of vision [6] or photosynthesis [9]. All these effects go along with large-amplitude nuclear motion which cannot easily be captured in terms of phonon modes. Here the natural strategy is to represent the nuclear wave packets in terms of classical trajectories in one way or another.

In solids, however, the nuclei tend to stay close to their equilibrium positions (unless the temperature gets close to the melting point). Nuclear motion is then well described in terms of phonon modes, and nonadiabaticity shows up as the electron-phonon interaction. Prime examples of nonadiabatic effects in this regime are phonon-mediated superconductivity [5], the renormalization of the band gap in insulators and semiconductors [10], as well as a phonon-induced modification of the electron dispersion in metals near the Fermi surface [11].

In the dynamics of strongly driven electrons and, likewise, in electron transport, electron-phonon scattering is an important damping mechanism. After exciting a metal with a strong laser pulse, the initial nonthermal distribution first reaches a purely electronic equilibrium within some tens of femtoseconds, and on the timescale of picoseconds, electron-phonon

scattering leads to a thermalization of the complete system of electronic and lattice degrees of freedom [12]. Similarly, magnon-phonon scattering is one of the mechanisms responsible for the damping of ultrafast spin-dynamics effects such as optical inter-site spin transfer [13]. In all these examples, dissipation, i.e., the transfer of energy from the electronic to the nuclear subsystem, is the relevant mechanism. Another important aspect is the influence of phonons on exciton dynamics. In some cases, the migration of excitons (which is essential for producing a photo-current in photovoltaic devices) is enabled through nonadiabatic electron-nuclear coupling, while for clamped nuclei the migration of excitons may be blocked [14–16].

The goal of this paper is to develop a single *ab initio* method able to predict all of the above nonadiabatic phenomena associated with small-amplitude nuclear motion in solids. The essence of our proposal is solve two coupled Bogoliubov equations alongside each other, one describing the electrons, the other treating the phononic degrees of freedom. Bogoliubov equations represent systems of noninteracting particles in terms of state vectors which are not eigenfunctions of the particle-number operator. This choice is deliberate and important. For the electronic subsystem, Bogliubov equations provide the natural framework to calculate the superconducting order parameter. Treating the phononic subsystem by a Bogoliubov equation as well is a less obvious choice but it is essential. Phonons can be generated from both the electron-phonon interaction (virtual phonons) or by an external influence such as a laser pulse (real phonons). Hence the number of phonons cannot be a conserved quantity. The two Bogoliubov equations are coupled through effective potentials which depend on the electronic and phononic normal and anomalous density matrices and on the electron-phonon coupling matrix. The two equations are solved self-consistently (in the stationary case) or propagated in time alongside each other. The influence goes both ways: The phonons, described by the bosonic Bogoliubov equation, renormalize the electronic band structure and/or make the system superconducting. Likewise, the electronic degrees of freedom renormalize the phonon spectrum, giving rise, for example, to a Kohn anomaly [17] or to modifications of the phonon spectrum due to the presence of superconductivity [18]. An important virtue of this method is that both real and virtual phonons arise from the same noninteracting state, which itself has been properly time evolved. This puts strong constraints on the phonon density matrices.

A necessary step in this paper is the construction of approximations for effective potentials as functionals of the normal and anomalous density matrices and the electron-phonon vertex,

$$\Gamma_{ij\mathbf{k}}^{\alpha\mathbf{q}} = \sum_{ap} \frac{\mathbf{e}_{ap}^{\alpha\mathbf{q}}}{\sqrt{2M_a \nu_{\alpha\mathbf{q}}}} \langle \varphi_{i\mathbf{k}+\mathbf{q}} | \partial \hat{V}_s / \partial u_{ap}^{\mathbf{q}} | \varphi_{j\mathbf{k}} \rangle, \qquad (1)$$

where i and j label Kohn-Sham [19] orbitals with momentum $\mathbf{k} + \mathbf{q}$ and $\mathbf{k}$, respectively; $\hat{V}_s$ is the Kohn-Sham potential operator; $u_{ap}^{\mathbf{q}}$ is a displacement of atom a in Cartesian direction p with phase $e^{i\mathbf{q}\cdot\mathbf{r}}$; M_a is the mass of the atom; $\mathbf{e}_{ap}^{\alpha\mathbf{q}}$ is the eigenvector of phonon mode $(\alpha, \mathbf{q})$; and $\nu_{\alpha\mathbf{q}}$ is the phonon

frequency. The construction makes use of the fact that, unlike the electron- only many-body problem, the coupled electron-nuclear system has a small parameter, the electron-nuclear mass ratio m/M, where m is the electron mass and M is a nuclear reference mass. In terms of this dimensionless parameter, the harmonic phonon frequencies are of order $(m/M)^{1/2}$. Anharmonic effects in the phonon frequencies show up in order $(m/M)^{3/4}$ and the lowest energy correction produced by the electron-phonon interaction is of order $(m/M)^{1/2}$. By virtue of Migdal's theorem, we know that the next order is smaller by another factor of $(m/M)^{1/2}$, and is therefore usually negligible. Our construction of the approximate functionals is based on the same principle: We consistently include all contributions to order $(m/M)^{1/2}$ and, in line with Migdal's theorem, neglect all higher-order contributions to the potentials.

In Sec. II, we describe how this is achieved in practice: The idea is to apply Wick's theorem to the square of the Fröhlich Hamiltonian [20]. This yields fermionic and bosonic Bogoliubov equations as well as explicit forms for their potentials. In Sec. III, we work out the algebraic structure of these Bogoliubov equations. Special attention will be given to the non-Hermitian nature of the bosonic Hamiltonian. The results of this section are quite general and apply equally to the equations describing the coupled motion of electrons and magnons, electrons and photons, or any other bosonic species coupled to the electronic system. In Sec. IV, we provide some details about the implementation for solids. Finally, in Sec. V, we will demonstrate the efficacy of the proposed method by computing the renormalized Kohn-Sham band gaps of diamond and silicon and also the superconducting gaps of niobium and MgB_2; as well as verifying that copper is *not* a superconductor at zero temperature. In doing so, we introduce two potential observables which provide detailed information on where in the reciprocal space electron-phonon interactions are the strongest. A major long-term aim of this paper is to perform a parameter-free, *ab initio* time evolution of the superconducting state for any solid. This would normally be prohibitively expensive with Green's function methods (although, see Karlsson *et al.* [21]). Time evolving the noninteracting bosonic state alongside the electronic state is, however, a practical method for such a simulation because all equations are first order in time and merely require a simple time-step integration. Such calculations would enable study of effects such as photoinduced superconductivity on short timescales by shaped laser pulses [22–25].

II. MEAN-FIELD THEORY OF A SQUARED HAMILTONIAN

Our aim is to replace an interacting Hamiltonian with a pair of noninteracting Hamiltonians, coupled only indirectly by their density matrices. In general, such Hamiltonians can be diagonalized using Bogoliubov transforms. Solutions to the Bogoliubov equations can then be used to obtain various observables needed for a unified description of the phenomena mention above such as band-gap renormalization and superconductivity.

We begin with a generalized Fröhlich Hamiltonian for solids,

$$\hat{H}_{\mathrm{F}} = \sum_{i\mathbf{k}} \epsilon_{i\mathbf{k}} \hat{a}_{i\mathbf{k}}^{\dagger} \hat{a}_{i\mathbf{k}} + \sum_{\alpha\mathbf{q}} \nu_{\alpha\mathbf{q}} \hat{d}_{\alpha\mathbf{q}}^{\dagger} \hat{d}_{\alpha\mathbf{q}}$$
$$+ \sum_{ij\mathbf{k},\alpha\mathbf{q}} \Gamma_{ij\mathbf{k}}^{\alpha\mathbf{q}} \hat{a}_{i\mathbf{k}+\mathbf{q}}^{\dagger} \hat{a}_{j\mathbf{k}} (\hat{d}_{\alpha\mathbf{q}} + \hat{d}_{\alpha-\mathbf{q}}^{\dagger}), \qquad (2)$$

where $\epsilon_{i\mathbf{k}}$ is taken to be the ith eigenvalue of a noninteracting system (typically Kohn-Sham [19]) at k-point $\mathbf{k}$; $\nu_{\alpha\mathbf{q}}$ is the αth phonon frequency at q-point $\mathbf{q}$; and $\Gamma_{ij\mathbf{k}}^{\alpha\mathbf{q}}$ are the electron-phonon coupling matrix elements from Eq. (1).

The Hamiltonian in Eq. (2) contains an interaction term (i.e., beyond quadratic order in the operators) and thus cannot be solved exactly. Instead we employ Wick's theorem [26], which rewrites $\hat{H}_{\mathrm{F}}$ as a sum of normal-ordered products arranged from uncontracted terms to fully contracted products. Our approximation is then to keep all terms up to quadratic order. Applying this strategy directly to $\hat{H}_{\mathrm{F}}$ results in two problems. The first is that a nontrivial solution would require that $\langle \hat{d}_{\alpha\mathbf{q}} + \hat{d}_{\alpha-\mathbf{q}}^{\dagger} \rangle \neq 0$, which would imply that the atoms have displaced. However, the superconducting transition is not brought about by an atomic displacement. For example, a solid with one atom per unit cell, such as bcc niobium, cannot undergo an atomic displacement across the transition and remain lattice periodic. The second problem is that there is no anomalous term of the form $\langle \hat{a}^{\dagger}\hat{a}^{\dagger} \rangle$ in the Wick expansion of $\hat{H}_{\mathrm{F}}$. These issues preclude the use of this approximation for superconductivity calculations.

We now make the observation that any operator raised to a power has the same eigenvectors as the original. In particular, if $\hat{H}_{\mathrm{F}} |\Psi_i\rangle = E_i |\Psi_i\rangle$ then

$$\hat{H}_{\mathrm{F}}^2 |\Psi_i\rangle = E_i^2 |\Psi_i\rangle, \qquad (3)$$

which can be used to determine the ground state of $\hat{H}_{\mathrm{F}}$ with the proviso that the sign of each E_i be determined independently. Wick's theorem applied to $\hat{H}_{\mathrm{F}}^2$ overcomes both aforementioned problems, namely that nontrivial solutions do not require atomic displacements and there is now an anomalous term in the Wick expansion.

The first term in the Wick expansion of $\hat{H}_{\mathrm{F}}^2$ is the direct term from the noninteracting part of the electronic Hamiltonian:

$$2\left[\frac{n_s}{N_k} \sum_{j\mathbf{k}'} \epsilon_{j\mathbf{k}'} \overline{\hat{a}_{j\mathbf{k}'}^{\dagger} \hat{a}}_{j\mathbf{k}'} + \frac{1}{N_q} \sum_{\alpha\mathbf{q}} \nu_{\alpha\mathbf{q}} \overline{\hat{d}_{\alpha\mathbf{q}}^{\dagger} \hat{d}}_{\alpha\mathbf{q}} \right] \sum_{i\mathbf{k}} \epsilon_{i\mathbf{k}} \hat{a}_{i\mathbf{k}}^{\dagger} \hat{a}_{i\mathbf{k}}$$
$$= 2\,\delta E_0 \sum_{i\mathbf{k}} \epsilon_{i\mathbf{k}} \hat{a}_{i\mathbf{k}}^{\dagger} \hat{a}_{i\mathbf{k}}, \qquad (4)$$

where $n_s = 1$ and $n_s = 2$ for spin-polarized and spin-unpolarized calculations, respectively, and the change in the noninteracting energy per unit cell is given by

$$\delta E_0 = \frac{n_s}{N_k} \sum_{i\mathbf{k}} \epsilon_{i\mathbf{k}} \, \delta\gamma_{ij}^{\mathbf{k}} + \frac{1}{N_q} \sum_{\alpha\mathbf{q}} \nu_{\alpha\mathbf{q}} \langle \hat{d}_{\alpha\mathbf{q}}^{\dagger} \hat{d}_{\alpha\mathbf{q}} \rangle. \qquad (5)$$

Here the change in electronic density matrix is given by

$$\delta\gamma_{ij}^{\mathbf{k}} = \gamma_{ij}^{\mathbf{k}} - \Theta(\epsilon_{i\mathbf{k}} - \epsilon_{\mathrm{F}})\delta_{ij}, \qquad (6)$$

with

$$\gamma_{ij}^{\mathbf{k}} = \langle \hat{a}_{i\mathbf{k}}^{\dagger} \hat{a}_{j\mathbf{k}} \rangle. \qquad (7)$$

Taking $\overline{\hat{a}_{i\mathbf{k}}^{\dagger} \hat{a}}_{j\mathbf{k}}$ to mean the change in the density matrix in Eq. (6), rather than the density matrix itself, is equivalent to first placing the Hamiltonian in particle-hole form. A consequence of this is that $\delta E_0 \geqslant 0$. Note that the equivalent exchange terms, such as

$$\frac{1}{N_k} \sum_{i\mathbf{k},j\mathbf{k}'} \epsilon_{i\mathbf{k}} \epsilon_{j\mathbf{k}'} \overline{\hat{a}_{j\mathbf{k}'}^{\dagger} \hat{a}_{j\mathbf{k}'} \hat{a}_{i\mathbf{k}}^{\dagger} \hat{a}}_{i\mathbf{k}}, \qquad (8)$$

tend to zero in the limit of an infinite k-point set. Before proceeding further, we will assume that the system is time-reversal symmetric; thus, if $\varphi_{i\mathbf{k}}(\mathbf{r})$ is an electronic orbital, then so is $\varphi_{i-\mathbf{k}}^*(\mathbf{r})$. This leads to the relationships

$$\Gamma_{ij\mathbf{k}}^{\alpha\mathbf{q}} = \Gamma_{ji-\mathbf{k}-\mathbf{q}}^{\alpha\mathbf{q}}, \quad \Gamma_{ij\mathbf{k}}^{*\alpha\mathbf{q}} = \Gamma_{ji\mathbf{k}+\mathbf{q}}^{\alpha-\mathbf{q}}, \quad \gamma_{ij}^{\mathbf{k}} = \gamma_{ji}^{-\mathbf{k}}. \quad (9)$$

The result of only keeping terms up to quadratic order is a Hamiltonian for which the fermions are decoupled from the bosons:

$$\hat{H} = \hat{H}_{\mathrm{f}} + \hat{H}_{\mathrm{b}}, \qquad (10)$$

where

$$\hat{H}_{\mathrm{f}} = \sum_{ij,\mathbf{k}} A_{ij}^{\mathbf{k}} \hat{a}_{i\mathbf{k}}^{\dagger} \hat{a}_{j\mathbf{k}} + \tfrac{1}{2} B_{ij}^{\mathbf{k}} \hat{a}_{i\mathbf{k}}^{\dagger} \hat{a}_{j-\mathbf{k}}^{\dagger} - \tfrac{1}{2} B_{ij}^{*\mathbf{k}} \hat{a}_{i\mathbf{k}} \hat{a}_{j-\mathbf{k}} \qquad (11)$$

and

$$\hat{H}_{\mathrm{b}} = \sum_{\alpha\alpha',\mathbf{q}} D_{\alpha\alpha'}^{\mathbf{q}} \hat{d}_{\alpha\mathbf{q}}^{\dagger} \hat{d}_{\alpha'\mathbf{q}} + \tfrac{1}{2} E_{\alpha\alpha'}^{\mathbf{q}} \hat{d}_{\alpha\mathbf{q}}^{\dagger} \hat{d}_{\alpha'-\mathbf{q}}^{\dagger} + \tfrac{1}{2} E_{\alpha\alpha'}^{*\mathbf{q}} \hat{d}_{\alpha\mathbf{q}} \hat{d}_{\alpha'-\mathbf{q}}$$
$$+ \sum_{\alpha} F_{\alpha}^{\mathbf{q}=0} (\hat{d}_{\alpha\mathbf{q}=0}^{\dagger} + \hat{d}_{\alpha\mathbf{q}=0}). \qquad (12)$$

The matrices A and B are given explicitly as

$$A_{ij}^{\mathbf{k}} = \epsilon_{i\mathbf{k}}\delta_{ij} - \epsilon_{\mathrm{F}} + \sum_{\alpha} \Gamma_{ij\mathbf{k}}^{\alpha\mathbf{q}=0} \langle \hat{d}_{\alpha\mathbf{q}=0} + \hat{d}_{\alpha\mathbf{q}=0}^{\dagger} \rangle$$
$$- \frac{2}{N_q\,\delta E_0} \sum_{i'j'} \sum_{\alpha\alpha'\mathbf{q}} \Gamma_{i'j\mathbf{k}}^{\alpha\mathbf{q}} \Gamma_{j'i\mathbf{k}}^{*\alpha'\mathbf{q}} \delta\gamma_{i'j'}^{\mathbf{k}+\mathbf{q}} [\langle \hat{d}_{\alpha\mathbf{q}}\hat{d}_{\alpha'-\mathbf{q}} \rangle$$
$$+ \langle \hat{d}_{\alpha'\mathbf{q}}^{\dagger}\hat{d}_{\alpha\mathbf{q}} \rangle + \langle \hat{d}_{\alpha-\mathbf{q}}^{\dagger}\hat{d}_{\alpha'-\mathbf{q}} \rangle + \langle \hat{d}_{\alpha-\mathbf{q}}^{\dagger}\hat{d}_{\alpha'\mathbf{q}}^{\dagger} \rangle], \qquad (13)$$

$$B_{ij}^{\mathbf{k}} = -\frac{2}{N_q\,\delta E_0} \sum_{i'j'} \sum_{\alpha\alpha'} \Gamma_{j'j\mathbf{k}}^{\alpha\mathbf{q}} \Gamma_{i'i\mathbf{k}}^{*\alpha'\mathbf{q}} \langle \hat{a}_{i'\mathbf{k}+\mathbf{q}}\hat{a}_{j'-\mathbf{k}-\mathbf{q}} \rangle$$
$$\times [\langle \hat{d}_{\alpha\mathbf{q}}\hat{d}_{\alpha'-\mathbf{q}} \rangle + \langle \hat{d}_{\alpha'\mathbf{q}}^{\dagger}\hat{d}_{\alpha\mathbf{q}} \rangle + \langle \hat{d}_{\alpha-\mathbf{q}}^{\dagger}\hat{d}_{\alpha'-\mathbf{q}} \rangle + \langle \hat{d}_{\alpha-\mathbf{q}}^{\dagger}\hat{d}_{\alpha'\mathbf{q}}^{\dagger} \rangle]. \qquad (14)$$

The matrix D is related to E by

$$D_{\alpha\alpha'}^{\mathbf{q}} = \nu_{\alpha\mathbf{q}}\delta_{\alpha\alpha'} + E_{\alpha\alpha'}^{\mathbf{q}}, \qquad (15)$$

with E arising from either the normal or anomalous electronic density matrices:

$$E_{\alpha\alpha'}^{\mathbf{q}} = -\frac{n_s}{N_k\,\delta E_0} \sum_{ij,i'j'\mathbf{k}} \Gamma_{ji\mathbf{k}}^{*\alpha\mathbf{q}} \Gamma_{i'j'\mathbf{k}}^{\alpha'\mathbf{q}} \delta\gamma_{i'j}^{\mathbf{k}+\mathbf{q}} \delta\gamma_{ij'}^{\mathbf{k}} \qquad \text{(normal)},$$
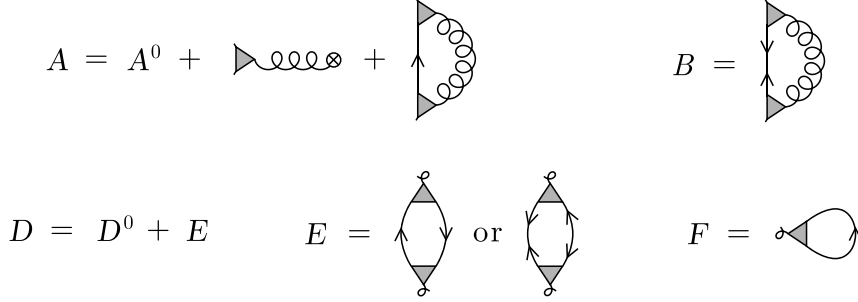$$\qquad (16)$$

FIG. 1. Schematic representation of the matrices A, B, D, E, and F corresponding to the contractions in Eqs. (13)–(18), respectively. The components are the electron-phonon vertex $\Gamma =$; the change in electronic density matrix $\delta\gamma =$; the anomalous density matrix $\langle \hat{a}\,\hat{a} \rangle =$; the phonon densities $\langle \hat{d}\,\hat{d}\rangle + \langle \hat{d}^\dagger \hat{d}\rangle + \langle \hat{d}^\dagger \hat{d}\rangle + \langle \hat{d}^\dagger \hat{d}^\dagger \rangle =$, and $\langle \hat{d} + \hat{d}^\dagger \rangle =$.

$$E^{\mathbf{q}}_{\alpha\alpha'} = \frac{n_s}{N_k\,\delta E_0} \sum_{ij,i'j'\mathbf{k}} \Gamma^{*\alpha\mathbf{q}}_{ji\mathbf{k}}\,\Gamma^{\alpha'\mathbf{q}}_{i'j'\mathbf{k}}\, \langle \hat{a}_{j\mathbf{k}+\mathbf{q}}\hat{a}_{i'-\mathbf{k}-\mathbf{q}}\rangle \langle \hat{a}^\dagger_{i\mathbf{k}}\hat{a}^\dagger_{j'-\mathbf{k}}\rangle$$

(anomalous).   (17)

Finally, the vector F is given by

$$F^{\mathbf{q}=0}_{\alpha} = \frac{n_s}{N_k} \sum_{ij\,\mathbf{k}} \Gamma^{\alpha\mathbf{q}=0}_{ij\mathbf{k}}\,\delta\gamma^{\mathbf{k}}_{ij}.$$ (18)

These terms are expressed diagramatically in Fig. 1, where instead of the propagators found in Feynman diagrams, there are electron and phonon density matrices connecting the vertices.

III. ALGEBRAIC FORM OF THE ELECTRON AND PHONON BOGOLIUBOV EQUATIONS

In the following, the k- and q-point dependencies of the fermionic and bosonic Hamiltonians are removed and we focus on their algebraic structure instead. All matrices are assumed to be finite in size.

A. Bogoliubov equation for electrons

The most general noninteracting fermionic Hamiltonian of interest here has the form

$$\hat{H}_{\mathrm{f}} = \sum_{i,j=1}^{n_{\mathrm{f}}} A_{ij}\hat{a}^\dagger_i \hat{a}_j + \tfrac{1}{2}B_{ij}\hat{a}^\dagger_i \hat{a}^\dagger_j - \tfrac{1}{2}B^*_{ij}\hat{a}_i\hat{a}_j,$$ (19)

where A is a Hermitian matrix; B is antisymmetric and corresponds to the matrix elements of the superconducting pairing potential $\Delta(\mathbf{r}, \mathbf{r}')$. The sum runs to the number of fermionic basis vectors n_{f}. The matrix A includes a chemical potential term $A_{ij} \to A_{ij} + \mu\delta_{ij}$ which is used to fix the total electronic number to N_{e}. The Hermitian eigenvalue problem

$$\begin{pmatrix} A & B \\ B^\dagger & -A^* \end{pmatrix}\begin{pmatrix} \vec{U}_j \\ \vec{V}_j \end{pmatrix} = \varepsilon_j \begin{pmatrix} \vec{U}_j \\ \vec{V}_j \end{pmatrix}$$ (20)

yields $2n_{\mathrm{f}}$ solutions. However, if ε_j and $(\vec{U}_j, \vec{V}_j)$ are an eigenpair, then so are $-\varepsilon_j$ and $(\vec{V}^*_j, \vec{U}^*_j)$. Now we select n_{f} eigenpairs with each corresponding to either a positive or negative eigenvalue but with its conjugate partner not in the set. This choice will not affect the eventual ground state. Let

U and V be the $n_{\mathrm{f}} \times n_{\mathrm{f}}$ matrices with these solutions arranged columnwise. Orthogonality of the vectors is then expressed as

$$\begin{pmatrix} U & V^* \\ V & U^* \end{pmatrix}^\dagger \begin{pmatrix} U & V^* \\ V & U^* \end{pmatrix} = I,$$ (21)

which implies $U^\dagger U + V^\dagger V = I$ and $U^\dagger V^* + V^\dagger U^* = 0$. Completeness further implies $UU^\dagger + V^*V^t = I$ and $UV^\dagger + V^*U^t = 0$. The Hamiltonian Eq. (19) can now be diagonalized with the aid of U and V via a Bogoliubov transformation [27]:,

$$\hat{\alpha}^\dagger_j = \sum_{i=1}^{n_{\mathrm{f}}} U_{ij}\hat{a}^\dagger_i + V_{ij}\hat{a}_i,$$

$$\hat{\alpha}_j = \sum_{i=1}^{n_{\mathrm{f}}} U^*_{ij}\hat{a}_i + V^*_{ij}\hat{a}^\dagger_i,$$ (22)

in other words,

$$\hat{H}_{\mathrm{f}} = \sum_{i=1}^{n_{\mathrm{f}}} \varepsilon_i \hat{\alpha}^\dagger_i \hat{\alpha}_i + W_0,$$ (23)

where $W_0 = -\mathrm{tr}(V\varepsilon V^\dagger)$. The fermionic algebra is also preserved for $\hat{\alpha}$:

$$\{\hat{\alpha}_i, \hat{\alpha}^\dagger_j\} = \delta_{ij}, \quad \{\hat{\alpha}_i, \hat{\alpha}_j\} = 0, \quad \{\hat{\alpha}^\dagger_i, \hat{\alpha}^\dagger_j\} = 0.$$ (24)

1. Noninteracting ground state

Given A and B, the matrices U, V, and ε are fixed by the Bogoliubov Eq, (20). What remains is to construct from these the eigenstates of Eq. (19) in the Fock space. To do so, one first needs to find a normalized vacuum state which is annihilated by all the $\hat{\alpha}_j$. Here it is (denoted $|\bar{0}\rangle$ so as to distinguish it from the normal vacuum state $|0\rangle$),

$$|\bar{0}\rangle \equiv \prod_{j=1}^{n_{\mathrm{f}}} \hat{U}_j \prod_{k=1}^{n_{\mathrm{f}}} \hat{a}^\dagger_k |0\rangle + \prod_{j=1}^{n_{\mathrm{f}}} \hat{V}^\dagger_j |0\rangle,$$ (25)

where $\hat{U}_j \equiv \sum_i U^*_{ij}\hat{a}_i$ and $\hat{V}^\dagger_j \equiv \sum_i V^*_{ij}\hat{a}^\dagger_i$. It is readily verified that $\hat{\alpha}_j|\bar{0}\rangle = 0$ for all j; the vacuum has the correct normalization $\langle\bar{0}|\bar{0}\rangle = 1$; and the vacuum energy $\langle\bar{0}|H_{\mathrm{f}}|\bar{0}\rangle = W_0$. The noninteracting many-body ground state can be constructed in analogy with the usual fermionic situation. Let M be the

number of $\varepsilon_j < 0$, then the ground state

$$|\Phi_0\rangle = \prod_{j=1}^{M} \hat{\alpha}_j^\dagger |\bar{0}\rangle, \tag{26}$$

so

$$\hat{H}_{\text{f}} |\Phi_0\rangle = E_0 |\Phi_0\rangle, \tag{27}$$

where $E_0 = \sum_{j=1}^{M} \varepsilon_j + W_0$.

2. Normal and anomalous densities

To determine the densities, both normal and anomalous, one first has to find the expectation values of pairs of $\hat{a}$ and $\hat{a}^\dagger$. These, in turn, are linear combinations of expectation values of pairs of $\hat{\alpha}$ and $\hat{\alpha}^\dagger$. Using the anticommutation relations Eqs. (24) and remembering that $\hat{\alpha}|\bar{0}\rangle = 0$, we get

$$\langle\Phi_0|\hat{\alpha}_i^\dagger \hat{\alpha}_j|\Phi_0\rangle = \begin{cases} \delta_{ij} & i, j \leqslant M \\ 0 & i, j > M \end{cases}$$

$$\langle\Phi_0|\hat{\alpha}_i \hat{\alpha}_j^\dagger|\Phi_0\rangle = \begin{cases} 0 & i, j \leqslant M \\ \delta_{ij} & i, j > M \end{cases} \tag{28}$$

and

$$\langle\Phi_0|\hat{\alpha}_i^\dagger \hat{\alpha}_j^\dagger|\Phi_0\rangle = 0, \quad \langle\Phi_0|\hat{\alpha}_i \hat{\alpha}_j|\Phi_0\rangle = 0. \tag{29}$$

Equations (22), (28), and (29) give the normal and anomalous density matrices:

$$\langle\Phi_0|\hat{a}_i^\dagger \hat{a}_j|\Phi_0\rangle = \sum_{k=1}^{M} U_{ik}^* U_{jk} + \sum_{k=M+1}^{n_{\text{f}}} V_{ik} V_{jk}^* \tag{30}$$

and

$$\langle\Phi_0|\hat{a}_i^\dagger \hat{a}_j^\dagger|\Phi_0\rangle = \sum_{k=1}^{M} U_{ik}^* V_{jk} + \sum_{k=M+1}^{n_{\text{f}}} V_{ik} U_{jk}^*. \tag{31}$$

3. Time evolution

What remains is to determine how the fermionic state evolves with time in the time-dependent version of the method. The form of the ground-state equations dictates that of the time-dependent equations. Thus, if we assume that the matrices A and B are now functions of time, then the time-dependent generalization of Eq. (20) is

$$i\frac{\partial}{\partial t}\begin{pmatrix} \vec{U}_j \\ \vec{V}_j \end{pmatrix} = \begin{pmatrix} A(t) & B(t) \\ B^\dagger(t) & -A^*(t) \end{pmatrix}\begin{pmatrix} \vec{U}_j \\ \vec{V}_j \end{pmatrix}, \tag{32}$$

with the time-dependent state given by $|\Phi(t)\rangle = \prod_{i=1}^{M} \hat{\alpha}_i^\dagger(t)|\bar{0}\rangle$. It is easy to show that this state satisfies

$$i\frac{\partial|\Phi(t)\rangle}{\partial t}$$
$$= \left(\sum_{ij} A_{ij}(t)\hat{a}_i^\dagger \hat{a}_j + \frac{1}{2}B_{ij}(t)\hat{a}_i^\dagger \hat{a}_j^\dagger - \frac{1}{2}B_{ij}^*(t)\hat{a}_i \hat{a}_j\right)|\Phi(t)\rangle, \tag{33}$$

with $|\Phi(t=0)\rangle = |\Phi_0\rangle$. Note that the number of occupied orbitals M remains constant with time. Here we have assumed that the system has evolved from its ground state.

B. Bogoliubov equation for phonons

The most general noninteracting bosonic Hamiltonian of relevance here has the form

$$\hat{H}_{\text{b}} = \sum_{ij} D_{ij}\hat{d}_i^\dagger \hat{d}_j + \frac{1}{2}E_{ij}\hat{d}_i^\dagger \hat{d}_j^\dagger + \frac{1}{2}E_{ij}^*\hat{d}_i \hat{d}_j$$
$$+ \sum_i F_i\hat{d}_i^\dagger + F_i^*\hat{d}_i, \tag{34}$$

where D is Hermitian and contains the kinetic energy operator; E is a complex symmetric matrix and F is a complex vector. Note that $\hat{H}_{\text{b}}$ contains the anomalous terms $\hat{d}_i^\dagger \hat{d}_j^\dagger$ and $\hat{d}_i \hat{d}_j$. In analogy with the fermionic case, this Hamiltonian can be diagonalized,

$$\hat{H}_{\text{b}} = \sum_{i=1}^{n_{\text{b}}} \omega_i \hat{\gamma}_i^\dagger \hat{\gamma}_i + \Omega_0, \tag{35}$$

with the Bogoliubov-type transformation

$$\hat{\gamma}_j = \sum_{i=1}^{n_{\text{b}}} W_{ij}^*\hat{d}_i + X_{ij}^*\hat{d}_i^\dagger + y_j^*,$$

$$\hat{\gamma}_j^\dagger = \sum_{i=1}^{n_{\text{b}}} W_{ij}\hat{d}_i^\dagger + X_{ij}\hat{d}_i + y_j, \tag{36}$$

where W and X are complex matrices and y is a complex vector. The index j runs from 1 to twice the number of bosonic modes. Requiring that $\hat{\gamma}$ and $\hat{\gamma}^\dagger$ obey bosonic algebra (the complex numbers y_j obviously commute with themselves and the operators, maintaining the algebra) yields

$$W^\dagger W - X^\dagger X = I, \tag{37}$$

$$W^\dagger X^* - X^\dagger W^* = 0. \tag{38}$$

After some manipulation, we arrive at the Bogoliubov equations for phonons:

$$\begin{pmatrix} D & -E \\ E^* & -D^* \end{pmatrix}\begin{pmatrix} \vec{W}_j \\ \vec{X}_j \end{pmatrix} = \omega_j\begin{pmatrix} \vec{W}_j \\ \vec{X}_j \end{pmatrix}. \tag{39}$$

The above equation cannot be reduced to a symmetric eigenvalue problem because the conditions Eqs. (37) and (38) correspond to the indefinite inner product $\eta = \text{diag}(1, \ldots, 1, -1, \ldots, -1)$. Such matrix Hamiltonians can still possess real eigenvalues [28–31] and this particular aspect is explored in Appendix A.

Once these equations are solved, the vector y is determined from

$$y = \omega^{-1}(W^t - X^t)F, \tag{40}$$

where $\omega = \text{diag}(\omega_1, \ldots, \omega_{n_{\text{b}}})$. The constant term in Eq. (35) given by

$$\Omega_0 = -\text{tr}(X\omega X^\dagger) - y^\dagger \omega y. \tag{41}$$

1. Existence and nature of the vacuum state

We now show that the state which is annihilated by all the $\hat{\gamma}_i$ exists. Let

$$\hat{w}_j := \sum_{i=1}^{n_b} W_{ij}^* \hat{d}_i \quad \hat{x}_j^\dagger := \sum_{i=1}^{n_b} X_{ij}^* \hat{d}_i^\dagger, \tag{42}$$

then

$$[\hat{w}_j, \hat{x}_j^\dagger] = \sum_{i=1}^{n_b} W_{ij}^* X_{ij}^* =: \tau_j. \tag{43}$$

Now consider the eigenvalue equation:

$$(\hat{w}_j + \hat{x}_j^\dagger)|\bar{0}_j\rangle = -y_j^*|\bar{0}_j\rangle. \tag{44}$$

Using the ansatz

$$|\bar{0}_j\rangle = \sum_{n=0}^{\infty} \frac{\kappa_n^j}{n!} (\hat{x}_j^\dagger)^n |0\rangle, \tag{45}$$

we obtain a recurrence relation

$$\kappa_n^j = \left[-y_j^* \kappa_{n-1}^j - (n-1)\kappa_{n-2}^j\right]/\tau_j \tag{46}$$

with $y_j^* \kappa_0^j = -\kappa_1^j \tau_j$ and κ_0^j chosen so $\langle\bar{0}_j|\bar{0}_j\rangle = 1$. Note that if $\kappa_n^j = 1$ for all n then Eq. (45) is a coherent state. The vacuum

state

$$|\bar{0}\rangle = \zeta \hat{S} \bigotimes_{j=1}^{n_b} |\bar{0}_j\rangle, \tag{47}$$

where ζ is a normalization constant and $\hat{S}$ is the symmetrizing operator, is annihilated by all $\hat{\gamma}_j$ and, because $\omega_j > 0$ for all j, is also the bosonic ground state, which is the lowest energy Fock space eigenstate of Eq. (34), as required.

2. Phononic observables and time evolution

To make the theory useful, observables which are products of the original $\hat{d}_i$ and $\hat{d}_i^\dagger$ operators have to be computed. After some straightforward algebra one finds that linear operators may be evaluated using

$$Y_i := \langle\bar{0}|\hat{d}_i|\bar{0}\rangle = \langle\bar{0}|\hat{d}_i^\dagger|\bar{0}\rangle^* = \sum_{j=1}^{n_b} X_{ij}^* y_j - W_{ij} y_j^*. \tag{48}$$

Observables which are quadratic are more complicated:

$$\langle\bar{0}|\hat{d}_i^\dagger\hat{d}_j|\bar{0}\rangle = Y_i^* Y_j + (XX^\dagger)_{ij}, \quad \langle\bar{0}|\hat{d}_i\hat{d}_j^\dagger|\bar{0}\rangle = Y_i Y_j^* + (WW^\dagger)_{ij},$$

$$\langle\bar{0}|\hat{d}_i^\dagger\hat{d}_j^\dagger|\bar{0}\rangle = Y_i^* Y_j^* - (XW^\dagger)_{ij}, \quad \langle\bar{0}|\hat{d}_i\hat{d}_j|\bar{0}\rangle = Y_i Y_j - (WX^\dagger)_{ij}. \tag{49}$$

The extension to the time-dependent case follows the same procedure as that for fermions, namely, that the matrices and vector D, E, and F in Eq. (34) become time-dependent as, consequently, do $\hat{\gamma}_i^\dagger$ and $|\bar{0}\rangle$ after solving the equation of motion:

$$i\frac{\partial}{\partial t}\begin{pmatrix}\vec{W}_j \\ \vec{X}_j\end{pmatrix} = \begin{pmatrix} D(t) & -E(t) \\ E^*(t) & -D^*(t) \end{pmatrix}\begin{pmatrix}\vec{W}_j \\ \vec{X}_j\end{pmatrix}. \tag{50}$$

This time evolution is not unitary but rather pseudounitary [32] and will not preserve ordinary vector lengths, in general, but will preserve the indefinite inner product. The vector y can be determined analogously from

$$i\frac{\partial y}{\partial t} = (W^t(t) - X^t(t))F(t). \tag{51}$$

Evolving Eqs. (50) and (51) in time is equivalent to doing the same for the second-quantized Hamiltonian and the Fock space state vector:

$$i\frac{\partial|\Phi(t)\rangle}{\partial t} = \left(\sum_{ij} D_{ij}(t)\hat{d}_i^\dagger\hat{d}_j + \tfrac{1}{2}E_{ij}(t)\hat{d}_i^\dagger\hat{d}_j^\dagger + \tfrac{1}{2}E_{ij}^*(t)\hat{d}_i\hat{d}_j + \sum_i F_i(t)\hat{d}_i^\dagger + F_i^*(t)\hat{d}_i\right)|\Phi(t)\rangle. \tag{52}$$

IV. IMPLEMENTATION FOR SOLIDS

Having established the electron and phonon Bogoliubov equations to be solved as well as expectation values of operator products, we can write the terms A, B, D, E, and F as functions of the quantities $(U_\mathbf{k}, V_\mathbf{k})$ and $(W_\mathbf{q}, X_\mathbf{q})$.

The normal electronic density matrix can be written

$$\gamma_{ij}^\mathbf{k} = \langle\hat{a}_{i\mathbf{k}}^\dagger\hat{a}_{j\mathbf{k}}\rangle = (V_\mathbf{k}V_\mathbf{k}^\dagger)_{ij}, \tag{53}$$

where we have used Eq. (30) and retained only the positive eigenvalues (as is our choice). All the terms in the H_f and H_b are determined in a similar manner:

$$A_{ij}^\mathbf{k} = \epsilon_{i\mathbf{k}}\delta_{ij} - \epsilon_F + 2\sum_\alpha \Gamma_{ij\mathbf{k}}^{\alpha\mathbf{q}=0}\operatorname{Re}(Y_\alpha^{\mathbf{q}=0})$$

$$- \frac{2}{N_q\,\delta E_0}\sum_{i'j'}\sum_{\alpha\alpha'\mathbf{q}}\Gamma_{i'j\mathbf{k}}^{\alpha\mathbf{q}}\Gamma_{j'i\mathbf{k}}^{*\alpha'\mathbf{q}}\,\delta\gamma_{i'j'}^{\mathbf{k}+\mathbf{q}}$$

$$\times [X_{-\mathbf{q}}X_{-\mathbf{q}}^\dagger - W_\mathbf{q}X_{-\mathbf{q}}^\dagger]_{\alpha\alpha'}, \tag{54}$$

$$B_{ij}^{\mathbf{k}} = -\frac{2}{N_q \, \delta E_0} \sum_{i'j'} \sum_{\alpha\alpha'\mathbf{q}} \Gamma_{j'j\mathbf{k}}^{\alpha\mathbf{q}} \, \Gamma_{i'i\mathbf{k}}^{*\alpha'\mathbf{q}} \, (U_{\mathbf{k}+\mathbf{q}} V_{-\mathbf{k}-\mathbf{q}}^\dagger)_{i'j'}$$

$$\times \, [X_{-\mathbf{q}} X_{-\mathbf{q}}^\dagger - W_{\mathbf{q}} X_{-\mathbf{q}}^\dagger]_{\alpha\alpha'}, \tag{55}$$

$$E_{\alpha\alpha'}^{\mathbf{q}} = -\frac{n_s}{N_k \, \delta E_0} \sum_{ij,i'j'\mathbf{k}} \Gamma_{ji\mathbf{k}}^{*\alpha\mathbf{q}} \, \Gamma_{i'j'\mathbf{k}}^{\alpha'\mathbf{q}} \, \delta\gamma_{i'j}^{\mathbf{k}+\mathbf{q}} \, \delta\gamma_{ij'}^{\mathbf{k}} \qquad \text{(normal)}, \tag{56}$$

$$E_{\alpha\alpha'}^{\mathbf{q}} = \frac{n_s}{N_k \, \delta E_0} \sum_{ij,i'j'\mathbf{k}} \Gamma_{ji\mathbf{k}}^{*\alpha\mathbf{q}} \, \Gamma_{i'j'\mathbf{k}}^{\alpha'\mathbf{q}} \, (U_{\mathbf{k}+\mathbf{q}} V_{-\mathbf{k}-\mathbf{q}}^\dagger)_{ji'} (U_{\mathbf{k}} V_{-\mathbf{k}}^\dagger)_{ij'}^*$$

$$\text{(anomalous)}, \tag{57}$$

$$D_{\alpha\alpha'}^{\mathbf{q}} = \nu_{\alpha\mathbf{q}}\delta_{\alpha\alpha'} + E_{\alpha\alpha'}^{\mathbf{q}}, \tag{58}$$

$$F_\alpha^{\mathbf{q}=0} = \frac{n_s}{N_k} \sum_{ij\mathbf{k}} \Gamma_{ij\mathbf{k}}^{\alpha\mathbf{q}=0} \, \delta\gamma_{ij}^{\mathbf{k}}. \tag{59}$$

Owing to time-reversal symmetry, the electron and phonon equations to be solved are

$$\begin{pmatrix} A_{\mathbf{k}} & B_{\mathbf{k}} \\ B_{\mathbf{k}}^\dagger & -A_{\mathbf{k}} \end{pmatrix} \begin{pmatrix} \vec{U}_{j\mathbf{k}} \\ \vec{V}_{j-\mathbf{k}} \end{pmatrix} = \varepsilon_{j\mathbf{k}} \begin{pmatrix} \vec{U}_{j\mathbf{k}} \\ \vec{V}_{j-\mathbf{k}} \end{pmatrix},$$

$$\begin{pmatrix} D_{\mathbf{q}} & -E_{\mathbf{q}} \\ E_{\mathbf{q}} & -D_{\mathbf{q}} \end{pmatrix} \begin{pmatrix} \vec{W}_{j\mathbf{q}} \\ \vec{X}_{j-\mathbf{q}} \end{pmatrix} = \omega_{j\mathbf{q}} \begin{pmatrix} \vec{W}_{j\mathbf{q}} \\ \vec{X}_{j-\mathbf{q}} \end{pmatrix}, \tag{60}$$

where $A_{\mathbf{k}}$, $D_{\mathbf{q}}$ and $E_{\mathbf{q}}$ are Hermitian and $B_{\mathbf{k}}$ is symmetric.

The above equations were implemented in the all-electron ELK code [33] which is a density functional theory (DFT) Kohn-Sham code and uses augmented plane waves as its basis. Phonon dispersions and the electron-phonon coupling matrix elements were determined using density functional perturbation theory (DFPT) [34]. The local density approximation (LDA) was used as the exchange-correlation functional throughout. The important issue of stability of the self-consistent procedure is addressed in Appendix B.

Anomalous correlation entropy

Before proceeding to the results, we first define a potentially useful quantity: the anomalous correlation entropy (ACE). Let $v_i \equiv |\vec{V}_i|^2$ be the norm squared of the V part of the vector $(\vec{U}_i, \vec{V}_i)$, and note that $0 \leqslant v_i \leqslant 1$. For a normal state (i.e., not superconducting) v_i is either 0 or 1. This suggests that we can define the fermionic ACE (FACE) as

$$\text{FACE} = -\sum_i v_i \ln(v_i) + (1 - v_i)\ln(1 - v_i), \tag{61}$$

which is a single, dimensionless quantity equal to zero for the normal state and greater than zero for the superconducting state. This is very similar to the correlation entropy of the one-reduced density matrix [35]. It is also possible to compute the FACE over a restricted sum of states, for example, those of a particular k point or simply for each individual state.

The bosonic ACE (BACE) is the analog for phonons. Here the X part of the vector $(\vec{W}_i, \vec{X}_i)$ is squared: $x_i \equiv |\vec{X}_i|^2$, which is positive and unbounded, and the formula for bosonic entropy
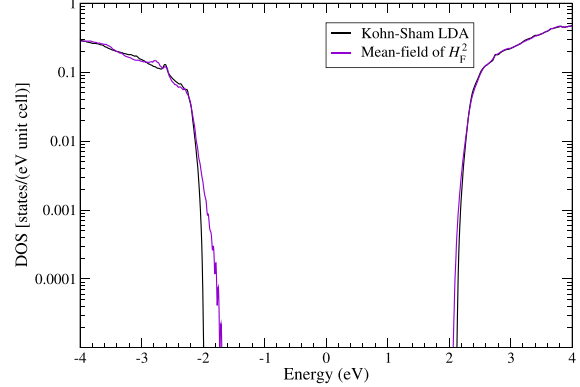

FIG. 2. Electronic density of states of diamond for both the conventional LDA Kohn-Sham system and the electron-phonon Bogoliubov equations derived from the mean field of $\hat{H}_F^2$.

is employed:

$$\text{BACE} = -\sum_i x_i \ln(x_i) - (1 + x_i)\ln(1 + x_i). \tag{62}$$

The BACE (and its q-point resolved variant) is useful for determining the strength of *virtual* phonon modes responsible for causing correlations in the electronic system.

V. RESULTS

A. Band-gap renormalization

1. Diamond

It has been known for some time that the band gap of diamond is significantly renormalized by the electron-phonon interaction [36–54]. We calculated the phonon dispersion and electron-phonon coupling matrix elements using DFPT with q-point and k-point grids both taken to be $16 \times 16 \times 16$. Calculations were performed using the experimentally determined lattice parameter. The electronic part electron-phonon system was solved in the basis of occupied orbitals plus 16 empty orbitals. Self-consistency was achieved in about 300 iterations. The density of states (DOS) is plotted in Fig. 2 for both the noninteracting (LDA) calculation and the electron-phonon calculation. Our calculated change in the fundamental (indirect) gap is -394 meV (from the Γ point to $(\frac{3}{8}, \frac{3}{8}, 0)$) and the change in the optical (direct) gap is -429 meV (Γ point). Table I lists band-gap renormalization energies from both experiment and theory. Previous theoretical results range from -462 meV to -321 meV for the fundamental gap and -670 meV to -409 meV for the optical gap. Experimental values range from -410 meV to -340 meV and -320 meV to -450 meV for the fundamental and optical gaps, respectively. This lack of consensus for the value both gap renormalization energies makes it difficult to judge the quality of our results. Both of the gaps determined using the current method lie within the range of both previous theory and experiment. Our indirect gap is closest to the experimental result of Monserrat *et al.* [40], which claims to be a more accurate extrapolation of the temperature-dependent

TABLE I. Band gap renormalization of diamond.

Reference	Fundamental gap renormalization (meV)	Optical gap renormalization (meV)
Experiment		
Logothetidis *et al.* [37]		−320, −450
Cardona [38]	−340	
Cardona [39]	−364, −370	
Monserrat *et al.* [40]	−410	
Theory		
Giustino *et al.* [41]		−615
Cannuccia and Marini [42]		−670
Monserrat and Needs [43]	−334	
Monserrat *et al.* [40]	−462	
Antonius *et al.* [44]		−404, −628
Poncé *et al.* [45]		−409
Lloyd-Williams and Monserrat [46]	−343	−430
Antonius *et al.* [47]		−320, −439
Poncé *et al.* [48]	−330	−416
Zacharias and Giustino [49]	−345	−450
Monserrat [50]	−344	
Monserrat [51]		∼ − 410, ∼ −642
Karsai *et al.* [52]	−320, −337	−326, −586
Miglio *et al.* [53]	−330	−416
Zhang *et al.* [54]	−437	
Current paper	−394	−429

thermal gap than previous estimates. Likewise, our optical gap is closest to the experimental value of Logothetidis *et al.* [37], determined from analyzing the second derivative of the dielectric function.

A significant observation is that most of the renormalization occurs at the valence band maximum with very little change to the conduction band DOS. This was also the conclusion reached by Engel *et al.* for the band gap renormalization of ice [55]. Precise resolution of this tail is critical for an accurate determination of the change in band gap. This, in turn, demands a sufficiently dense k-point set. The large variance among the theoretical results may be a consequence of some calculations being inadequately converged with respect to the number of k points.

Slices of the BACE across the Brillouin zone are plotted in Fig. 3 and are determined from Eq. (62), where the q point is fixed and the sum is only over the phonon branches. The values exhibit considerable variation, ranging from about 0.06 to 1.51. There are several hot spots throughout the zone where the virtual phonons which contribute to the renormalization of the electronic band gap are most prevalent. Those of highest intensity occur in the plane at $\mathbf{q} = \frac{1}{8}(1, 1, 1)$. We note that, like the k-point set, the strong variation of the BACE across the zone indicates that a large number of q points may be required to properly converge the renormalized gap.

2. Silicon

As a second example of band-gap renormalization, we applied the method to silicon. For this case, an 8×8×8 q-point grid along with a shifted 16×16×16 k-point grid was used. Our calculated gaps were quite similar to one another:

−36 meV and [from the Γ point to $(0, \frac{9}{16}, \frac{9}{16})$] for the fundamental and −35 meV (Γ point) for the optical. These are in reasonable to good agreement with previous calculations and experiment (see Table II). The gap renormalization is over an order of magnitude smaller than that of diamond, indicating that the method works for a wide range of values.

The LDA and electron-phonon renormalized DOS is plotted in Fig. 4. Although the change in the gap is much smaller than that of diamond, the same characteristic that most of the effect arises from the highest occupied states is observed. The DOS of the conduction band is completely unchanged.

B. Superconductivity

Prediction of the superconducting state provides a stringent test for our method because of the very small energy scale of the superconducting gap compared to typical bandwidths. Accurate determination of the gap requires a large sampling of k points very close to the Fermi surface. In our calculations, a small shift was applied to the regular k-point grid, the effect of which is to reduce the number of equivalent points and thus distribute the eigenvalues more evenly around the Fermi energy. In addition, a small energy window was applied to the matrix elements of B in Eq. (55). All matrix elements corresponding to states with eigenvalues outside this window were set to zero. This is to ensure that only states very close to the Fermi energy can contribute to the anomalous density. The window was taken to be 0.001 Ha ($\sim$27.2 meV) for all cases below. We found that the superconducting gap was fairly insensitive to this choice so long as there was a sufficient number of k points whose eigenvalues lay within this window. In both plots below, the points have been mirrored around zero to effectively increase the k-point sampling.
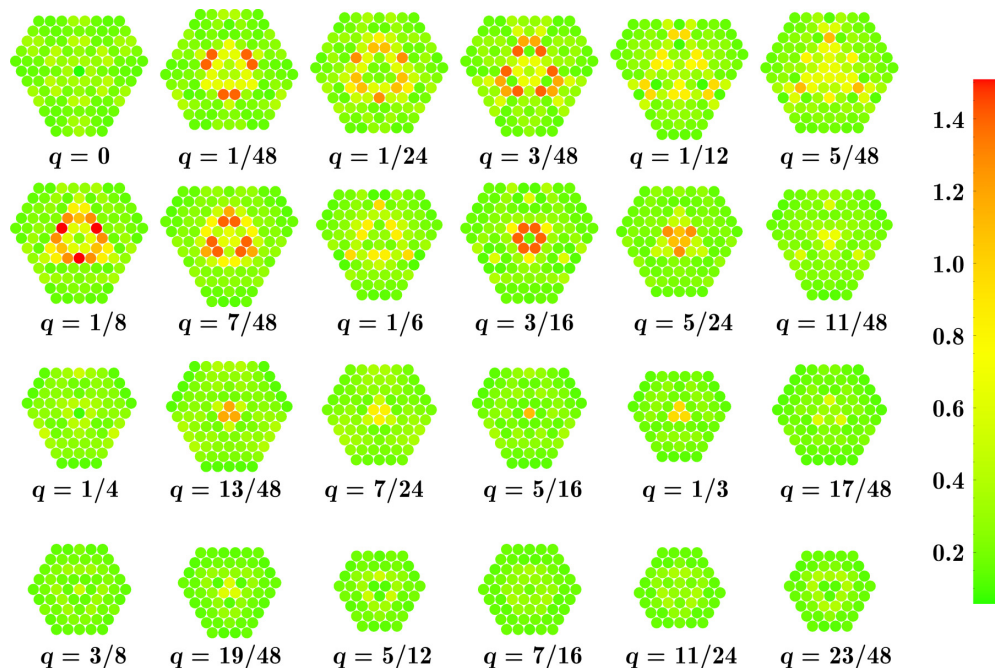
FIG. 3. Bosonic anomalous correlation entropy for diamond plotted across half the Brillouin zone. The vector at the center of each plane is given by $q(1, 1, 1)$ in reciprocal lattice coordinates. The value of the dimensionless BACE ranges from about 0.06 to 1.51.

It is important to mention that the anomalous Coulomb interaction is *not* included in these calculations, which generally results in superconducting gaps that are overestimated. We will compare our FACE to equivalent data calculated using the well-tested superconducting density functional theory (SCDFT) [58–62], where the effect of the Coulomb interaction has been deliberately omitted. The SCDFT code has the advantage of being able to upsample the k-point grid via interpolation to better resolve the su-

perconducting gap. By convention, the superconducting gap should be measured from zero in the figures below. Note that the Fermi energy was continuously adjusted during the calculation to maintain the correct total charge.

1. Niobium

The phonon dispersion and electron-phonon matrix elements for bcc Nb were calculated on a $8 \times 8 \times 8$ q-point set and a $40 \times 40 \times 40$ k-point set shifted by $(\frac{1}{4}, \frac{1}{2}, \frac{5}{8})$ of the smallest

TABLE II. Band gap renormalization of silicon.

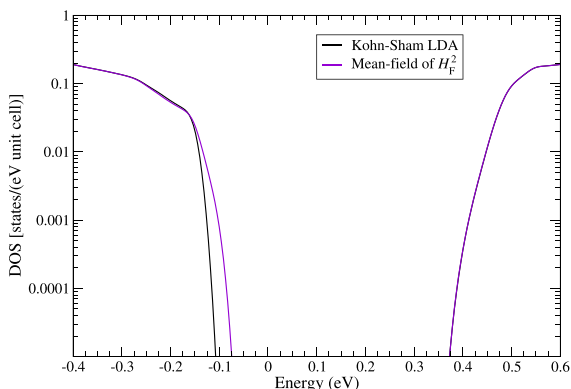| Reference	Fundamental gap renormalization (meV)	Optical gap renormalization (meV)
Experiment		
Lautenschlager [56]		−25
Cardona [38]	−50	
Pässler [57]	−72	
Cardona [39]	−60, −64	
Theory		
Monserrat *et al.* [43]	−60	
Poncé *et al.* [48]	−56	−42
Monserrat [50]	−58	
Monserrat [51]		−28
Zacharias and Giustino [49]	−57	−44
Karsai *et al.* [52]	−65	
Miglio *et al.* [53]	−56	−42
Zhang *et al.* [54]	−75	
Current paper	−36	−35

FIG. 4. Electronic density of states of silicon for both the conventional LDA Kohn-Sham system and the electron-phonon Bogoliubov equations derived from the mean-field of $\hat{H}_F^2$.

division. The total FACE converged in about 500 iterations. An energy-resolved histogram of the FACE for each state and k-point is presented in Fig. 5. This is compared to equivalent data calculated using SCDFT. One can see immediately that the FACE is nonzero in a region around the Fermi energy and that there is also a gap present. Owing to the scattered nature
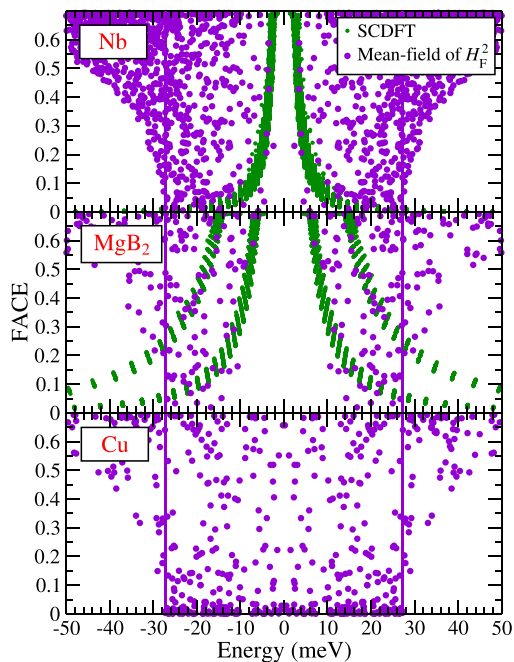

FIG. 5. State and k-point resolved FACE histogram of niobium, MgB_2, and copper calculated with SCDFT and the electron-phonon Bogoliubov equations derived from the mean-field of $\hat{H}_F^2$. The vertical lines indicate the energy cutoff used when evaluating the matrix B in Eq. (55). In both plots, the points have been mirrored around zero to effectively increase the k-point sampling.

of the points in the histogram, the precise value of the gap itself is difficult to ascertain. The minimum gap based on a single point is 2.4 meV. SCDFT (without Coulomb) gives a value of 2.5 meV, although this does not correspond to the single point with smallest gap but rather the midpoint of the main cluster of points taken at maximum FACE value. There is good agreement between our mean-field theory and SCDFT for the inner boundary of the FACE over the complete range of energies. One of the more recent experiments puts the value of the Nb superconducting gap at 1.49 meV [63]. The SCDFT gap with the Coulomb interaction included yields a gap of between 1.54 and 1.79 meV [60], indicating the magnitude of this effect. Including the anomalous Coulomb interaction in our calculations should also reduce our gap to about this value.

2. MgB_2

The superconducting state of MgB_2 is much more difficult to converge with respect to the number of k points than Nb. This is because its Fermi surface contains two-dimensional cylinderlike structures [64] which require particularly careful sampling. We used a k-point grid of $36 \times 36 \times 24$ shifted by $(\frac{1}{4}, \frac{1}{2}, \frac{5}{8})$ of the smallest division. The q-point set was taken to be $12 \times 12 \times 6$. The DFPT calculation generated about 140 GB of electron-phonon coupling data, putting it at the limit of our computational resources. This limitation and the form of the Fermi surface meant the resolution of the gap was not as good as for Nb. Convergence of the total FACE was achieved in about 500 iterations and took over 700 CPU hours, which was the most of all our calculations.

The state and k-point resolved FACE energy histogram can be see in Fig. 5. Distinct from the case of Nb is the appearance of two superconducting gaps in the plot. This is because the MgB_2 Fermi surface arises from two sets of bands with σ and π character [64]. Despite the noise, we estimate the π band gap from the single FACE point closest to zero, as 5.9 meV. This agrees well with the SCDFT value of 6.5 meV. On the whole, the inner boundary of the π band FACE is in good agreement with that of SCDFT.

It is nearly impossible to reliably extract a value for the second gap because of the sparsity of sampled points. SCDFT yields a value of about 15 meV. Nevertheless, an inner boundary of the σ gap can be discerned and follows that obtained from SCDFT. Better resolution of the σ gap of MgB_2 clearly requires a much denser k-point grid; this could be accomplished by an upsampling of the grid, as done in the SCDFT code.

3. Copper

Copper does not exhibit superconducting properties even at vanishingly small temperatures but rather possesses a residual resistance. Our method should therefore predict a superconducting gap of zero for this metal. The phonon dispersion and matrix elements were calculated for fcc Cu using a $8 \times 8 \times 8$ q-point grid and a $40 \times 40 \times 40$ k-point grid. The total FACE was considerably smaller than that for Nb and MgB_2, and converged in about 800 iterations. The state and k-point resolved FACE energy histogram can be seen in Fig. 5 and the absence of a gap is immediately apparent. This is an important test for

the Bogoliubov equations because it demonstrates that they did not produce a false positive for superconductivity, i.e., they correctly predict that fcc Cu should *not* be a superconductor even at a zero temperature.

VI. SUMMARY

We have defined noninteracting Hamiltonians for fermions and bosons which are coupled only via their respective density matrices. Both are solved using Bogoliubov equations: the fermionic are Hermitian and the bosonic are Hermitian only with respect to an indefinite metric. Sufficient conditions which guarantee real eigenvalues for the bosonic system were found. Explicit forms of the potential matrix elements A, B, D, E, and F which constitute the equations were found using mean-field potentials derived from Wick's theorem applied to the square of the Fröhlich Hamiltonian. Electron and phonon density matrices were determined by solving the equations together and self-consistently. We found that this approach correctly reproduced the renormalization of the band gaps in diamond and silicon. The superconducting gaps of bcc Nb and MgB_2 were shown to reproduce those of SCDFT, and fcc Cu was found to be nonsuperconducting, in accordance with experiment.

Based on these results, we are confident that this is a practical method for parameter-free simulations of the time evolution of the superconducting state. Furthermore, these equations and the application of Wick's theorem to the square of a Hamiltonian could be used for other theories with bosonic fields. One such example is quantum electrodynamics (QED), for which the method may be useful for studying strong field dynamics which include pair creation effects, or for cavity QED with discrete photon modes.

APPENDIX A: MATHEMATICAL PROPERTIES OF THE BOSONIC BOGOLIUBOV EQUATIONS

In this Appendix, we prove that under certain conditions the matrix Eq. (39) always possesses n_b solutions which satisfy Eqs. (37) and (38). This requires the observation that if the vector $v \equiv (w, x)$ with eigenvalue ω is a solution to Eq. (39), then so is $\bar{v} \equiv (x, w)$ with eigenvalue $-\omega$. To simplify the arguments, we consider only the special case where the matrices D and E are real symmetric and the vector F is also real. In

this case, the bosonic Hamiltonian can be written as

$$\hat{H}_b = \sum_{ij} D_{ij} \hat{d}_i^\dagger \hat{d}_j + \tfrac{1}{2} E_{ij}(\hat{d}_i^\dagger \hat{d}_j^\dagger + \hat{d}_i \hat{d}_j) + \sum_i F_i(\hat{d}_i^\dagger + \hat{d}_i).$$

$$(A1)$$

Theorem 1. Let

$$H = \begin{pmatrix} D & -E \\ E & -D \end{pmatrix},$$

where D and E are real symmetric $n_b \times n_b$ matrices. Suppose H has only real, nondegenerate eigenvalues and every eigenvector v satisfies $v^t \eta v \neq 0$. Then

(1) The eigenvectors of H may be chosen real.

(2) The eigenvalue Eq. (39) has exactly n_b solutions which satisfy the conditions Eqs. (37) and (38).

Proof. The proof that the eigenvectors may be chosen real is straightforward, so we now prove the second statement. Let v_1 and v_2 be two real eigenvectors of H with corresponding real eigenvalues ω_1 and ω_2. Now $Hv_1 = \omega_1 v_1 \Rightarrow \eta H v_1 = \omega_1 \eta v_1$ and because ηH is symmetric we have $v_1^t \eta H = \omega_1 v_1^t \eta$ and thus $v_1^t \eta H v_2 = \omega_1 v_1^t \eta v_2$. We also have that $Hv_2 = \omega_2 v_2$ and so $v_1^t \eta H v_2 = \omega_2 v_1^t \eta v_2$. Subtracting and using the fact that $\omega_1 \neq \omega_2$ yields $v_1^t \eta v_2 = 0$. This is equivalent to the off-diagonal part of condition Eq. (37). Consider an eigenvector $v = (w, x)$ of H. Now $v^t \eta v \neq 0$, thus if $v^t \eta v < 0$ then choose the other eigenvector $\bar{v}$ for which $\bar{v}^t \eta \bar{v} > 0$. Such an eigenvector can be rescaled arbitrarily to ensure $v^t \eta v = 1$. This corresponds to the diagonal part of Eq. (37) but is valid for only half of the total number of eigenvectors since rescaling cannot change the sign of $v^t \eta v$. These remaining vectors are discarded. Condition Eq. (38) is trivially satisfied for the diagonal. For any two vectors v_i and v_j, suppose $v_j \neq \bar{v}_i$ then $\bar{v}_j = v_k$ for some other k. The off-diagonal part of condition Eq. (37) is satisfied for all vectors, thus $v_i^t \eta v_k = v_i^t \eta \bar{v}_j = 0$. If $v_j = \bar{v}_i$, then one of these vectors will have been discarded.

The theorem is easily extended to the case where H has degenerate eigenvalues. There is no guarantee that the eigenvalues of H are real since the matrix is not Hermitian. We therefore need additional restrictions on the matrices D and E to ensure this; the following conditions are sufficient but not necessary. We use the notation $P \succ 0$ to mean that the symmetric matrix P is positive definite, and that $P \succ Q$ implies $P - Q \succ 0$.

Theorem 2. Let $D \succ 0$, and suppose that E is a symmetric matrix. If any of the following are true then H has real eigenvalues:

(1) $D \succ ED^{-1}E$.

(2) The largest eigenvalue of $(ED^{-1})^2$ is less than 1.

(3) $z^\dagger Dz > |z^\dagger Ez|$ for all $z \in \mathbb{C}^{n_b}$.

(4) $E \succ 0$ and $D \succ E$.

(5) $E \succ 0$ and $D^p \succ E^p$, where $p \geq 1$.

(6) $D^2 \succ E^2$.

Furthermore, if all eigenvalues are nonzero, then all eigenvectors satisfy $v^t \eta v \neq 0$.

Proof. Let ω and v be an eigenvalue and eigenvector of H. The matrix

$$\eta H = \begin{pmatrix} D & -E \\ -E & D \end{pmatrix}$$

is symmetric, therefore both sides of $v^\dagger \eta H v = \omega v^\dagger \eta v$ are real. The only requirement for ω to be real is that $v^\dagger \eta H v$ be nonzero, which is ensured so long as $\eta H \succ 0$. This follows from either of the conditions (i) or (ii) (see, for example, Ref. [66]). Condition (iii) follows from Theorem 2.1 in Ref. [67] and (iv) follows immediately. The Löwner-Heinz theorem [68] reduces condition (v) to (iv). Finally, suppose $D^2 \succ E^2$, where E may not be positive definite. E is symmetric, therefore $E^2 \succ 0$, which means that there exists a symmetric matrix $e \succ 0$ such that $e^2 = E^2$. The Löwner-Heinz theorem implies that $D \succ e$, therefore $z^\dagger D z > z^\dagger e z$ for all complex vectors $z \in \mathbb{C}^{n_b}$. E and e can be simultaneously diagonalized and for each eigenvalue λ of E there is a corresponding positive eigenvalue $|\lambda|$ of e. In this eigenvector basis, it is easy to see that $z^\dagger e z \geq |z^\dagger E z|$ for all z, which in turn gives condition (iii), thereby proving (vi). In fact, all of the above conditions imply [67] that $\eta H \succ 0$. Thus, if all eigenvalues $\omega \neq 0$, then $v^t \eta v \neq 0$.

Corollary 2.1. Let $D_0 \succ 0$ and $E \succeq 0$ (positive semidefinite), then $D = D_0 + E$ yields real eigenvalues for H.

Theorem 3. Let D be an arbitrary real symmetric matrix and let f be a real function such that $|f(x)| < |x|$ for all $x \in \mathbb{R}$, then by setting $E = f(D)$ (in the usual function of matrices sense [69]), H has real eigenvalues and every eigenvector v satisfies $v^t \eta v \neq 0$.

Proof. We first note that

$$H^2 = \begin{pmatrix} D^2 - E^2 & [E, D] \\ [E, D] & D^2 - E^2 \end{pmatrix}.$$

It is obvious for any $E = f(D)$ that $[E, D] = 0$ and $D^2 \succ E^2$. Therefore, all the eigenvalues of H^2 are real and positive. We conclude that the eigenvalues of H are real and nonzero, thus $v^t \eta v \neq 0$ follows from Theorem 2.

Theorem 4. Let D be a real symmetric matrix which has no zero eigenvalues and which commutes with all the matrices in a group representation $S = \{S_i\}$. Further suppose that any degenerate eigenvalues of D correspond only to irreducible representations of S (i.e., there are no accidental degeneracies). If E is a real symmetric matrix which also commutes with all the matrices in S, then there exists a $\xi > 0$ such that if $E \to \xi E$ then $H(\xi)$ has real eigenvalues.

Proof. From the properties of the determinant applied to blocked matrices, the eigenvalues of H^2 are also the eigenvalues of $Q := D^2 - E^2 + [E, D]$. Since $[D, S_i] = [E, S_i] = 0$

for all i, then D^2, E^2, $[E, D]$ and thus $Q(\xi)$ also commute with S_i. Schur's lemma applies equally well to non-Hermitian matrices, therefore the degeneracies of $Q(\xi)$ are not lost as ξ increases. We also note that the roots of a polynomial depend continuously on its coefficients and hence the eigenvalues of $Q(\xi)$ depend continuously on ξ. From the conjugate root theorem, if $Q(\xi)$ has a complex eigenvalue then it must also have its complex conjugate as an eigenvalue. For sufficiently small $\xi > 0$, the eigenvalues of D^2 cannot become complex because this would require lifting of a degeneracy. Also, because of continuity and because D^2 has strictly positive eigenvalues, a sufficiently small $\xi > 0$ will keep them positive. Hence the eigenvalues of $H(\xi)$ are real.

APPENDIX B: STABILITY OF THE BOGOLIUBOV EQUATIONS

We discovered from our initial implementation of the Bogoliubov equations that the self-consistent procedure was highly unstable and difficult or impossible to converge. The reasons for this are twofold: First, in each of the Eqs. (54)–(58), there is a division by δE_0. If this number becomes very small, then the terms in the Hamiltonian become large. In the next iteration, δE_0 is then large and the terms are small. Consequently, δE_0 becomes small again. This oscillatory behavior can be tamed by mixing the input and output density matrices with a small mixing parameter. A second and more severe source of instability is the indefinite metric required for solving the bosonic Bogoliubov Eq. (39). Typically, the right eigenvectors of a non-Hermitian matrix returned by a numerical linear algebra package such as LAPACK [70] are normalized to 1 using the regular Euclidean norm. However, an eigenvector which is a solution to Eq. (39) should have pseudonorm $|\vec{W}_i|^2 - |\vec{X}_i|^2 = 1$. If β_i is the pseudonorm of the vector $(\vec{W}_i, \vec{X}_i)$ with Euclidean norm 1, then we have to scale it by $1/\sqrt{\beta_i}$ to normalize it correctly. This is an obvious source of instability because β_i can be arbitrarily close to zero. Such instability can be cured by making the observation that the effect of electron-phonon coupling on the phonon system is usually so small that $\beta_i \simeq |\vec{W}_i|^2 \simeq 1$. Thus, we instead scale the vector by $[1 - (1 - \beta_i)^p]/\sqrt{\beta_i}$, where p is usually taken to be 2, although we find that the converged results are independent of this choice. This scaling approaches the original for β_i close to 1 but is equal to 0 for $\beta_i \to 0$. The combination of the modified scaling and slow mixing allow the calculations to achieve self-consistency.

[1] M. Born and R. Oppenheimer, Ann. Phys. **389**, 457 (1927).

[2] M. Born and K. Huang, *Dynamical Theory of Crystal Lattices* (Oxford University Press, London, 1956).

[3] W. Kutzelnigg, Mol. Phys. **90**, 909 (1997).

[4] W. Kutzelnigg, Mol. Phys. **105**, 2627 (2007).

[5] J. Bardeen, L. N. Cooper, and J. R. Schrieffer, Phys. Rev. **108**, 1175 (1957).

[6] D. Polli, P. Altoè, O. Weingart, K. M. Spillane, C. Manzoni, D. Brida, G. Tomasello, G. Orlandi, P. Kukura, R. A. Mathies, M. Garavelli, and G. Cerullo, Nature (London) **467**, 440 (2010).

[7] A. H. Zewail, J. Phys. Chem. A **104**, 5660 (2000).

[8] I. Schapiro, P. El-Khoury, and M. Olivucci, in *Handbook of Computational Chemistry* (Springer Netherlands, Amsterdam, 2012), p. 1359.

[9] G. D. Scholes, G. R. Fleming, A. Olaya-Castro, and R. van Grondelle, Nat. Chem. **3**, 763 (2011).

[10] M. Cardona and M. L. W. Thewalt, Rev. Mod. Phys. **77**, 1173 (2005).

[11] R. Requist, C. R. Proetto, and E. K. U. Gross, Phys. Rev. B **99**, 165136 (2019).

[12] W. S. Fann, R. Storz, H. W. K. Tom, and J. Bokor, Phys. Rev. B **46**, 13592 (1992).

[13] J. K. Dewhurst, P. Elliott, S. Shallcross, E. K. U. Gross, and S. Sharma, Nano Lett. **18**, 1842 (2018).

[14] C. A. Rozzi, S. A. Falke, N. Spallanzani, A. Rubio, E. Molinari, D. Brida, M. Maiuri, G. Cerullo, H. Schramm, J. Christoffers, and C. Lienau, Nat. Commun. **4**, 1602 (2013).

[15] S. M. Falke, C. A. Rozzi, D. Brida, M. Maiuri, M. Amato, E. Sommer, A. De Sio, A. Rubio, G. Cerullo, E. Molinari, and C. Lienau, Science **344**, 1001 (2014).

[16] T. R. Nelson, A. J. White, J. A. Bjorgaard, A. E. Sifain, Y. Zhang, B. Nebgen, S. Fernandez-Alberti, D. Mozyrsky, A. E. Roitberg, and S. Tretiak, Chem. Rev. **120**, 2215 (2020).

[17] W. Kohn, Phys. Rev. Lett. **2**, 393 (1959).

[18] R. J. McQueeney, Y. Petrov, T. Egami, M. Yethiraj, G. Shirane, and Y. Endoh, Phys. Rev. Lett. **82**, 628 (1999).

[19] W. Kohn and L. J. Sham, Phys. Rev. **140**, A1133 (1965).

[20] H. Fröhlich, Adv. Phys. **3**, 325 (1954).

[21] D. Karlsson, R. van Leeuwen, Y. Pavlyukh, E. Perfetto, and G. Stefanucci, Phys. Rev. Lett. **127**, 036402 (2021).

[22] A. Cavalleri, Contemp. Phys. **59**, 31 (2018).

[23] S. J. Zhang, Z. X. Wang, H. Xiang, X. Yao, Q. M. Liu, L. Y. Shi, T. Lin, T. Dong, D. Wu, and N. L. Wang, Phys. Rev. X **10**, 011056 (2020).

[24] M. Buzzi, D. Nicoletti, M. Fechner, N. Tancogne-Dejean, M. A. Sentef, A. Georges, T. Biesner, E. Uykur, M. Dressel, A. Henderson, T. Siegrist, J. A. Schlueter, K. Miyagawa, K. Kanoda, M.-S. Nam, A. Ardavan, J. Coulthard, J. Tindall, F. Schlawin, D. Jaksch *et al.*, Phys. Rev. X **10**, 031028 (2020).

[25] M. Budden, T. Gebert, M. Buzzi, G. Jotzu, E. Wang, T. Matsuyama, G. Meier, Y. Laplace, D. Pontiroli, M. Riccò, F. Schlawin, D. Jaksch, and A. Cavalleri, Nat. Phys. **17**, 611 (2021).

[26] F. Scheck, *Quantum Physics* (Springer, Berlin, 2007), pp. 317–320.

[27] N. N. Bogoliubov, J. Phys. (Moscow) **11**, 23 (1947).

[28] E. C. G. Sudarshan, Phys. Rev. **123**, 2183 (1961).

[29] A. Mostafazadeh, J. Math. Phys. **43**, 205 (2002).

[30] C. F. M. Faria and A. Fring, Laser Phys. **17**, 424 (2007).

[31] L. Zhang, J. Ren, J. S. Wang, and B. Li, J. Phys.: Condens. Matter **23**, 305402 (2011).

[32] A. Mostafazadeh, J. Math. Phys. **45**, 932 (2004).

[33] The Elk Code, http://elk.sourceforge.net/.

[34] S. Baroni, P. Giannozzi, and A. Testa, Phys. Rev. Lett. **58**, 1861 (1987).

[35] D. M. Collins, Z. Naturforsch. A **48**, 68 (1993).

[36] S. Zollner, M. Cardona, and S. Gopalan, Phys. Rev. B **45**, 3376 (1992).

[37] S. Logothetidis, J. Petalas, H. M. Polatoglou, and D. Fuchs, Phys. Rev. B **46**, 4483 (1992).

[38] M. Cardona, Physica Status Solidi (a) **188**, 1209 (2001).

[39] M. Cardona, Solid State Commun. **133**, 3 (2005).

[40] B. Monserrat, G. J. Conduit, and R. J. Needs, Phys. Rev. B **90**, 184302 (2014).

[41] F. Giustino, S. G. Louie, and M. L. Cohen, Phys. Rev. Lett. **105**, 265501 (2010).

[42] E. Cannuccia and A. Marini, Eur. Phys. J. B **85**, 320 (2012).

[43] B. Monserrat and R. J. Needs, Phys. Rev. B **89**, 214304 (2014).

[44] G. Antonius, S. Poncé, P. Boulanger, M. Côté, and X. Gonze, Phys. Rev. Lett. **112**, 215501 (2014).

[45] S. Poncé, G. Antonius, P. Boulanger, E. Cannuccia, A. Marini, M. Côté, and X. Gonze, Comput. Mater. Sci. **83**, 341 (2014).

[46] J. H. Lloyd-Williams and B. Monserrat, Phys. Rev. B **92**, 184301 (2015).

[47] G. Antonius, S. Poncé, E. Lantagne-Hurtubise, G. Auclair, X. Gonze, and M. Côté, Phys. Rev. B **92**, 085137 (2015).

[48] S. Poncé, Y. Gillet, J. Laflamme Janssen, A. Marini, M. Verstraete, and X. Gonze, J. Chem. Phys. **143**, 102813 (2015).

[49] M. Zacharias and F. Giustino, Phys. Rev. B **94**, 075125 (2016).

[50] B. Monserrat, Phys. Rev. B **93**, 014302 (2016).

[51] B. Monserrat, Phys. Rev. B **93**, 100301(R) (2016).

[52] F. Karsai, M. Engel, E. Flage-Larsen, and G. Kresse, New J. Phys. **20**, 123008 (2018).

[53] A. Miglio, V. Brousseau-Couture, E. Godbout, G. Antonius, Y.-H. Chan, S. G. Louie, M. Côté, M. Giantomassi, and X. Gonze, npj Comput. Mater. **6**, 167 (2020).

[54] Y. Zhang, Z. Wang, J. Xi, and J. Yang, J. Phys.: Condens. Matter **32**, 475503 (2020).

[55] E. A. Engel, B. Monserrat, and R. J. Needs, J. Chem. Phys. **143**, 244708 (2015).

[56] P. Lautenschlager, M. Garriga, L. Vina, and M. Cardona, Phys. Rev. B **36**, 4821 (1987).

[57] R. Pässler, Phys. Rev. B **66**, 085201 (2002).

[58] L. N. Oliveira, E. K. U. Gross, and W. Kohn, Phys. Rev. Lett. **60**, 2430 (1988).

[59] M. Lüders, M. A. L. Marques, N. N. Lathiotakis, A. Floris, G. Profeta, L. Fast, A. Continenza, S. Massidda, and E. K. U. Gross, Phys. Rev. B **72**, 024545 (2005).

[60] M. A. L. Marques, M. Lüders, N. N. Lathiotakis, G. Profeta, A. Floris, L. Fast, A. Continenza, E. K. U. Gross, and S. Massidda, Phys. Rev. B **72**, 024546 (2005).

[61] A. Sanna, C. Pellegrini, and E. K. U. Gross, Phys. Rev. Lett. **125**, 057001 (2020).

[62] A. Sanna (Private Communication).

[63] A. V. Pronin, M. Dressel, A. Pimenov, A. Loidl, I. V. Roshchin, and L. H. Greene, Phys. Rev. B **57**, 14416 (1998).

[64] I. I. Mazin and V. P. Antropov, Physica C **385**, 49 (2003).

[65] J. H. P. Colpa, Physica A **93**, 327 (1978).

[66] R. A. Horn and C. R. Johnson, *Matrix Analysis* (Cambridge University Press, Cambridge, 1990) Chap. 7, p. 473.

[67] C. H. Fitzgerald and R. A. Horn, J. London Math. Soc. **s2-15**, 419 (1977).

[68] X. Zhan, *Matrix Inequalities* (Springer-Verlag, Berlin, 2002), Chap. 1, p. 2.

[69] R. F. Rinehart, Amer. Math. Monthly **62**, 395 (1955).

[70] E. Anderson, Z. Bai, C. Bischof, S. Blackford, J. Demmel, J. Dongarra, J. Du Croz, A. Greenbaum, S. Hammarling, A. McKenney, and D. Sorensen, *LAPACK Users' Guide*, 3rd ed. (Society for Industrial and Applied Mathematics, Philadelphia, PA, 1999).

6.   Conclusions and Outlook

In this thesis, the laser-induced dynamics of electrons and nuclei in solids has been studied from an *ab-initio* perspective. The described processes involve a strong initial excitation of the electrons by a short laser pulse followed by the non-adiabatic dynamics of the coupled electron-nuclear system. This means that there are two distinct types of interactions to be dealt with: the light-matter interaction and the electron-nuclear interaction beyond the Born-Oppenheimer approximation. In this PhD work, we first applied the real-time TD-DFT method to study the electron dynamics in the presence of strong laser pulses. In the second section of the thesis, the coupled electron-nuclear dynamics has been characterized by a dynamical generalization of the Born effective charges. Those are obtained from the electronic response to the (time-dependent) displacement of a classical nuclear point charge. In the last (and main) part of the thesis, we have developed a fully quantum mechanical treatment (i.e. there are no classical trajectories) for the non-adiabatic electron-nuclear dynamics in solids in terms of an electronic and a phononic Bogoliubov equation. These two Bogoliubov equations are coupled and have to be solved in a self-consistent way.

The real-time TD-DFT approach is the method of choice to investigate the light-induced electron dynamics in solids. It is easily implemented and it scales favorably with the number of electrons compared with wave-function or Green-function methods. In this thesis, an implementation of real-time TD-DFT in the Elk code has been used. Like in all DFT methods, the quality of the results obtained depends on the approximation employed for the XC functional. The adiabatic LDA (ALDA) functional significantly underestimates the absorption edges in the calculated optical spectra due to the well-known Kohn-Sham band gap problem in DFT. On the other hand, having an accurate band gap is crucial for the description of light-matter interactions. One of the goals of this thesis was to find easy-to-use and efficient correction scheme. We propose as real-time TD-DFT version of the so-called scissor correction. Within this scissor correction, the band gaps of insulators and semi-conductors are rigidly shifted to match their experimental values. We first show that this procedure greatly improves the calculated absorption energies after a short laser pulse in both the linear and nonlinear regimes. This outcome was to be expected (by construction). A result less obvious -but very reassuring- was revealed by comparing the optical spectrum calculated with the scissor-corrected ALDA with the one calculated with the modified Becke-Johnson (mBJ) potential (a functional

which also yields improved band gaps). We find that the scissor-corrected ALDA produces optical spectra in better agreement with experiment. While both methods show an improved band gap, the mBJ potential, when used in the time propagation, distorts other parts of the spectrum, in particular, it falsely narrows the width of some bands in the band structures for a number of materials with *d*-orbitals such as ZnSe. Since, on the other hand, the Kohn-Sham band gaps obtained from standard ground-state KS calculations with the mBJ potential are quite accurate, one can first perform a mBJ calculation to obtain a reasonable band gap efficiently and then use this band gap in the scissor-corrected LDA real-time TD-DFT. It is important to note that excitonic effects are not captured by this procedure. This problem has not been further pursued in this thesis. To deal with it, one may follow a recent suggestion by Sun et al.[56] who adapted the well- known long-range corrected exchange-correlation kernel to be used within the real-time propagation.

In the second major section of the thesis, the effects of nuclear motion are studied via a mixed quantum-classical approach. Our goal was to generalize the concept of Born effective charges to the time domain. For this purpose, we chose the nuclear trajectory to be generated by a sudden displacement of a nucleus at the initial time. We then obtained the linear response of the electronic system triggered by this particular motion of a classical point nucleus. In this way we were able to extend the concept of Born effective charges to the dynamical regime in a very natural way and calculate it with using the RT-TD-DFT approach. Here the change of the macroscopic polarization was calculated by integrating the macroscopic electronic currents induced by the nuclear displacement. Straightforwardly, the dynamical Born effective charge is then obtained as the Fourier transform of the macroscopic current divided by the Fourier transform of the velocity of the displaced nucleus. We find significant resonance peaks at rather high energies (up to hundred electron volts) in the dynamical Born effective charge spectra of the selected materials in our study. Quite different from the dielectric function, the spectrum of the dynamical Born effective charges depends individually on the atoms in the lattice. The static limit of the dynamical Born effective charges (which represents the traditional static Born effective charges) as obtained in our calculations, turned out to be in good agreement with experimental results and with Berry phase calculations. For Cl in LiCl, results are less accurate, possibly due to limitations of the LAPW basis. In the past, the Born effective charges in metals had been considered ill-defined until a recent publication by Dreyer et al.[23] who take the Drude weight in to account. We find the static limit of our calculated dynamical Born effective charges of Aluminium in good agreement with the (static) calculation of Dreyer et al. The profile of the dynamical Born effective charge is able to quantify the amount of the energy absorbed by excitation of electronic currents. Therefore, it could potentially improve the ab-initio calculations of ion-stopping in the energy range of a few hundred electron volts[57, 58]. Futhermore, we can couple the dynamical Born effective charge with frequency dependent electric fields to modify the calculation of the force acting on an atom in molecular dynamics calculations. Generally speaking, the dynamical Born effective charge is a natural choice to investigate the non-adiabatic electron-nuclear

coupling of an individual atom. It tells us the amount and the direction of electronic charges moving along with the motion of a nucleus at a given frequency.

Finally, in the third and main part of the thesis, we develop a methodology able to study the non-adiabatic electron-nuclear dynamics for solids fully quantum mechanically. Starting from the Fröhlich Hamiltonian and using the fact that the eigenvalues of the square of the Hamiltonian are the original eigenvalues squared, i.e. $\hat{H}^2|\psi\rangle = \lambda^2|\psi\rangle$, we made a mean-field approximation for the square of the Fröhlich Hamiltonian. By the virtue of lattice periodicity and the application of Wick's theorem, we deduced a set of two coupled Bogoliubov equations, one for the electrons (which may be superconducting) and one for the phonons. The phononic Bogoliubov equation is non-hermitian in general, so the eigenvalues are not necessary real-valued. We therefore discuss some sufficient conditions to ensure that the the eigenvalues of the bosonic Bogoliubov equation are real-valued. Furthermore, the bosonic Bogoliubov equations are pseudo-unitary; thus, the corresponding eigenvectors preserve the pseudo-norm. This property may cause numerical instabilities which we were able to handle by a mixing scheme. To analyze the numerical results, we introduced two quantities, FACE and BACE, to characterize the electronic and phononic excitations. BACE is particularly important for insulators because FACE is zero in general for common insulators. Our results for diamond and silicon are in good agreement with previous studies of the (phonon-induced) band gap renormalization. With the same set of equations, we also calculated the superconducting gap and found it in good agreement with SC-DFT calculations. For Nb, the superconducting gap is 2.4 meV based on the minimum of the single point of FACE. The π gap of MgB$_2$ is estimated to be 5.9 meV and, due to the cylinder structure, the resolution of the σ band is insufficient, requiring a much denser $\boldsymbol{k}$-point grid. To demonstrate that our theory does not produce false positives of superconducting gaps, we also did a calculation for copper finding no superconducting gap, in agreement with the experimental facts.

Our ground-state calculations correctly describe different phenomena caused by the electron-phonon interaction. Remarkably, the superconducting gaps and the band gap renormalization of insulators are both correctly obtained from the same set of equations. These results are a crucial first step towards a practical scheme describing the time evolution of superconducting states. The coupled Bogoliubov equations have been formulated for the time-dependent case in this thesis by allowing the mean-field potentials A, B, D, E and F to be time-dependent. We can determine the time evolution of the electronic and phononic states by propagating the coupled time-dependent Bogoliubov equations alongside each other. In this way, electrons and nuclei are being treated on equal footing. Similar to the static case, these equations are coupled through the (now time-dependent) electronic and phononic density matrices which enter the mean-field potentials in the equations. The mean-field potentials are local in time, a fact which makes the equations numerically tractable. This work opens a straightforward *ab-initio* path to explore the non-equilibrium dynamics of laser-driven superconductors and, in particular, also the creation of superconducting excited states[15–19] from non- superconducting ground

states by laser irradiation. The exploration of these scenarios with the methodology developed in this thesis will be exciting future projects.

Bibliography

[1] M. Born and R. Oppenheimer. Zur quantentheorie der molekeln. *Ann. Phys.*, 389:457, 1927.

[2] M. Born and K. Huang. *Dynamical Theory of Crystal Lattices*. Oxford: Oxford University Press, 1954.

[3] T. R. Nelson, A. J. White, J. A. Bjorgaard, A. E. Sifain, Y. Zhang, B. Nebgen, S. Fernandez-Alberti, D. Adrian, E. Roitberg, and S. Tretiak. Non-adiabatic excited-state molecular dynamics: Theory and applications for modeling photophysics in extended molecular materials. *Chem. Rev.*, 120:2215–2287, 2020.

[4] M. P. Bircher, E. Liberatore, N. J. Browning, S. Brickel, C. Hofmann, A. Patoz, O. T. Unke, T. Zimmermann, M. Chergui, P. Hamm, U. Keller, M. Meuwly, H.-J. Woerner, J. Vaníček, and U. Rothlisberger. Nonadiabatic effects in electronic and nuclear dynamics. *Struct. Dyn.*, 4:061510, 2017.

[5] H. J. Wörner J. B. Bertrand, P. B. Corkum, and D. M. Villeneuve. High-harmonic homodyne detection of the ultrafast dissociation of Br_2 molecules. *Phys. Rev. Lett.*, 105:103002, 2010.

[6] H. J. Wörner, J. B. Bertrand, D. V. Kartashov, P. B. Corkum, and D. M. Villeneuve. Following a chemical reaction using high-harmonic interferometry. *Nature*, 466:604–607, 2010.

[7] A. Cavalleri, Cs. Tóth, C. W. Siders, J. A. Squier, F. Ráksi, P. Forget, and J. C. Kieffer. Femtosecond structural dynamics in VO_2 during an ultrafast solid-solid phase transition. *Phys. Rev. Lett.*, 87:237401, 2001.

[8] F. Carbone, P. Baum, P. Rudolf, and A. H. Zewail. Structural preablation dynamics of graphite observed by ultrafast electron crystallography. *Phys. Rev. Lett.*, 100:035501, 2008.

[9] W. S. Fann, R. Storz, H. W. K. Tom, and J. Bokor. Electron thermalization in gold. *Phys. Rev. B*, 46:13592, 1992.

[10] P. Maldonado, T. Chase, A. H. Reid, X. Shen, R. K. Li, K. Carva, T. Payer, M. Horn von Hoegen, K. Sokolowski-Tinten, X. J. Wang, P. M. Oppeneer,

and H. A. Dürr. Tracking the ultrafast nonequilibrium energy flow between electronic and lattice degrees of freedom in crystalline nickel. *Phys. Rev. B*, 101:100302(R), 2020.

[11] J. K. Dewhurst, P. Elliott, S. Shallcross, E. K. U. Gross, and S. Sharma. Laser-induced intersite spin transfer. *Nano Lett.*, 18:1842, 2018.

[12] C. V. Shank, R. Yen, and C. Hirlimann. Time-resolved reflectivity measurements of femtosecond-optical-pulse-induced phase transitions in silicon. *Phys. Rev. Lett.*, 50:454, 1983.

[13] P. Saeta, J.-K. Wang, Y. Siegal, N. Bloembergen, and E. Mazur. Ultrafast electronic disordering during femtosecond laser melting of GaAs. *Phys. Rev. Lett.*, 67:1023, 1991.

[14] K. Sokolowski-Tinten, J. Bialkowski, and D. von der Linde. Ultrafast laser-induced order-disorder transitions in semiconductors. *Phys. Rev. B*, 51:14186, 1995.

[15] D. Fausti, R.I. Tobey, N. Dean, S. Kaiser, A. Dienst, M. C. Hoffmann, S. Pyon, T. Takayama, H. Takagi, and A. Cavalleri. Light-induced superconductivity in a stripe-ordered cuprate. *Science*, 331:189, 2011.

[16] D.A. Dubroka, M. Rössle, K. W. Kim, V. K. Malik, D. Munzar, D. N. Basov, A. A. Schafgans, S. J. Moon, C. T. Lin, D. Haug, V. Hinkov, B. Keimer, Th. Wolf, J. G. Storey, J. L. Tallon, and C. Bernhard. Light-induced superconductivity in a stripe-ordered cuprate. *Phys. Rev. Lett.*, 406:047006, 2011.

[17] E. Uykur, K. Tanaka, T. Masui, S. Miyasaka, and S. Tajima. Persistence of the superconducting condensate far above the critical temperature of $YBa_2(Cu,Zn)_3O_y$ revealed by c-axis optical conductivity measurements for several Zn concentrations and carrier doping levels. *Phys. Rev. Lett.*, 112:127003, 2014.

[18] M. Mitrano, A. Cantaluppi, D. Nicoletti, S. Kaiser, A. Perucchi, S. Lupi, P. Di Pietro, D. Pontiroli, M. Riccò, S. R. Clark, D. Jaksch, and A. Cavalleri. Possible light-induced superconductivity in K_3C_{60} at high temperature. *Nature*, 530:461–464, 2016.

[19] K. Isoyama, N. Yoshikawa, K. Katsumi, J. Wong, N. Shikama, Y. Sakishita, F. Nabeshima, A. Maeda, and R. Shimano. Light-induced enhancement of superconductivity in iron-based superconductor $FeSe_{0.5}Te_{0.5}$. *Commun Phys*, 4:160, 2021.

[20] A. D. Becke and M. R. Roussel. Exchange holes in inhomogeneous systems: A coordinate-space model. *Phys. Rev. A*, 39:3761, 1989.

[21] A. D. Becke and E. R. Johnson. A simple effective potential for exchange. *J. Chem. Phys.*, 124:221101, 2006.

[22] L. Binci, P. Barone, and F. Mauri. First-principles theory of infrared vibrational spectroscopy of metals and semimetals: Application to graphite. *Phys. Rev. B*, 103:134304, 2021.

[23] C. E. Dreyer, S. Coh, and M. Stengel. Nonadiabatic born effective charges in metals and the drude weight. *Phys. Rev. Lett.*, 128:095901, 2022.

[24] Rolf Heid. *The Physics of Correlated Insulators, Metals, and Superconductors Modeling and Simulation*, volume 3, chapter 12. Verlag des Forschungszentrum Jülich, 2013.

[25] E. Engel and R. M. Dreizler. *Density Functional Theory: An Advanced Course (Theoretical and Mathematical Physics)*. Springer, 2011.

[26] Carsten Ullrich. *Time-Dependent Density-Functional Theory: Concepts and Applications (Oxford Graduate Texts)*. Oxford University Press, 2012.

[27] David J. Singh. *Planewaves, pseudopotentials, and the LAPW method.* Springer, 2006.

[28] P. Hohenberg and W. Kohn. Inhomogeneous electron gas. *Phys. Rev.*, 136:B864, 1964.

[29] R. M. Dreizler and E. K. U. Gross. *Density Functional Theory.* Springer Berlin, Heidelberg, 1990.

[30] T. L. Gilbert. Hohenberg-kohn theorem for nonlocal external potentials. *Phys. Rev. B*, 12:2111, 1975.

[31] W. Kohn and L. J. Sham. Self-consistent equations including exchange and correlation effects. *Phys. Rev.*, 140:A1133, 1965.

[32] J. P. Perdew and Y. Wang. Accurate and simple analytic representation of the electron-gas correlation energy. *Phys. Rev. B*, 45:13244, 1992.

[33] D. M. Ceperley and B. J. Alder. Ground state of the electron gas by a stochastic method. *Phys. Rev. Lett.*, 45:566, 1980.

[34] E. Wigner. On the interaction of electrons in metals. *Phys. Rev.*, 46:1002, 1934.

[35] M. Gell-Mann and K. A. Brueckner. Correlation energy of an electron gas at high density. *Phys. Rev.*, 106:364, 1957.

[36] J. P. Perdew, K. Burke, and M. Ernzerhof. Generalized gradient approximation made simple. *Phys. Rev. Lett.*, 77:3865, 1996.

[37] P. Ziesche, S. Kurth, and J.P. Perdew. Density functionals from LDA to GGA. *Computational Materials Science*, 11:122–127, 1998.

[38] F. Tran and P. Blaha. Accurate band gaps of semiconductors and insulators with a semilocal exchange-correlation potential. *Phys. Rev. Lett.*, 102:226401, 2009.

[39] L. N. Oliveira, E. K. U. Gross, and W. Kohn. Density-functional theory for superconductors. *Phys. Rev. Lett.*, 60:2430, 1988.

[40] N. D. Mermin. Thermal properties of the inhomogeneous electron gas. *Phys. Rev.*, 137:A1441, 1965.

[41] M. Marques. *Density Functional Theory for Superconductors, Exchange and Correlation Potentials for Inhomogeneous Systems.* PhD thesis, Bayerische Julius-Maximilians Universität Wuürzburg, 2000.

[42] E. Runge and E. K. U. Gross. Density-functional theory for time-dependent systems. *Phys. Rev. Lett.*, 52:997, 1984.

[43] Robert van Leeuwen. Mapping from densities to potentials in time-dependent density-functional theory. *Phys. Rev. Lett.*, 82:3863, 1999.

[44] L. Reining, V. Olevano, A. Rubio, and G. Onida. Excitonic effects in solids described by time-dependent density-functional theory. *Phys. Rev. Lett.*, 88:066404, 2002.

[45] S. Botti, A. Fourreau, F. Nguyen, Y. Renault, F. Sottile, and L. Reining. Energy dependence of the exchange-correlation kernel of time-dependent density functional theory: A simple model for solids. *Phys. Rev. B*, 72:125203, 2005.

[46] S. Sharma, J. K. Dewhurst, A. Sanna, and E. K. U. Gross. Bootstrap approximation for the exchange-correlation kernel of time-dependent density-functional theory. *Phys. Rev. Lett.*, 107:186401, 2011.

[47] X. Andrade, A. Castro, D. Zueco, J. L. Alonso, P. Echenique, F. Falceto, and Á. Rubio. Modified ehrenfest formalism for efficient large-scale ab initio molecular dynamics. *J. Chem. Theory Comput.*, 5:728–742, 2009.

[48] M. Calandra, G. Profeta, and F. Mauri. Adiabatic and nonadiabatic phonon dispersion in a Wannier function approach. *Phys. Rev. B*, 82:165111, 2010.

[49] C-Y. Wang, P. Elliott, S. Sharma, and J. K. Dewhurst. Real time scissor correction in td-dft. *J. Phys.: Condens. Matter*, 31:214002, 2019.

[50] F. Nastos, B. Olejnik, K. Schwarz, and J. E. Sipe. Scissors implementation within length-gauge formulations of the frequency-dependent nonlinear optical response of semiconductors. *Phys. Rev. B*, 72:045223, 2005.

[51] Z. H. Levine and D. C. Allan. Linear optical response in silicon and germanium including self-energy effects. *Phys. Rev. Lett.*, 63:1719, 1989.

[52] R. M. Pick, M. H. Cohen, and R. M. Martin. Microscopic theory of force constants in the adiabatic approximation. *Phys. Rev. B*, 1:910, 1970.

[53] X. Gonze and C. Lee. Dynamical matrices, Born effective charges, dielectric permittivity tensors, and interatomic force constants from density-functional perturbation theory. *Phys. Rev. B*, 55:10355, 1997.

[54] C.-Yu Wang, S. Sharma, E. K. U. Gross, and J. K. Dewhurst. Dynamical born effective charges. *Phys. Rev. B*, 106:L180303, 2022.

[55] C.-Yu Wang, S. Sharma, T. Müller, E. K. U. Gross, and J. K. Dewhurst. Coupled bogoliubov equations for electrons and phonons. *Phys. Rev. B*, 105:174509, 2022.

[56] J. Sun, Ch.-W. Lee, A. Kononov, A. Schleife, and C. A. Ullrich. Real-time exciton dynamics with time-dependent density-functional theory. *Phys. Rev. Lett.*, 127:077401, 2021.

[57] P. Sigmund. Stopping of slow ions. *Bull. Russ. Acad. Sci. Phys.*, 72:569, 2008.

[58] M. Caro, A. A. Correa, E. Artacho, and A. Caro. Stopping power beyond the adiabatic approximation. *Sci Rep*, 7:2618, 2017.

List of Publications

Real time scissor correction in TD-DFT, C-Y. Wang, P. Elliott, S. Sharma and
J. K. Dewhurst
J. Phys.: Condens. Matter 31 214002 (2019)

Coupled Bogoliubov equations for electrons and phonons, C.-Yu Wang, S. Sharma,
T. Müller, E. K. U. Gross and J. K. Dewhurst
Phys. Rev. B 105, 174509 (2022)

Dynamical Born effective charges, C.-Yu Wang, S. Sharma, E. K. U. Gross, and
J. K. Dewhurst
Phys. Rev. B 106, L180303 (2022)

Acknowledgments

First of all, I would like to thank Prof. Dr. Hardy Gross for providing me this opportunity to pursue PhD in his group. I am grateful to his generous support particularly during the COVID-19 pandemic. It has been a difficult time for the past two years and I would not be able to finish this PhD work without his support. I would also like to show my gratitude to Dr. J. K. Dewhurst and Dr. S. Sharma for their warm co-supervising. Dr. Dewhurst is always helpful, very patient and open minded. He provided me precious advices and pointed out many blind spots of mine. Dr. Sharma provides me the financial support for the first period of my PhD study. She also introduced me the interesting real-time TD-DFT project. I am very lucky to have them as my co-supervisor. I would like thank Dr. Peter Elliot. Peter helped me to understand the structure of the Elk code and finish our first scientific project. Lastly I would like to thank rest of the members in our group particularly Dr. Antonio Sanna and Dr. Matthew Hodgson for creating inspiring and delightful atmosphere.

Curriculum Vitae

Personal information

Name: Chung-Yu Wang
Nationality: Taiwan

Education

10/2019 - present:	Visiting research fellow in Hebrew university of Jerusalem, supervised by Prof. Eberhard K. U. Gross
09/2016 - 09/2019:	PhD student in Max Planck Institute of Microstructure Physics, supervised by Prof. Eberhard K. U. Gross
09/2015 - 08/2016:	Research assistant in IAMS, Academia Sinica, supervised by Prof. Jer-Lai Kuo
10/2014 - 09/2015:	Mandatory military service
09/2012 - 07/2014:	M. Sc in Physics, National Taiwan University, supervised by Prof. Guang-Yu Guo
09/2008 - 07/2012:	B. Sc in Chemistry, National Taiwan University

Statutory Declaration

I hereby declare that I have written my dissertation independently and without outside help. I have not used any sources or resources other than those I have specified and have identified the passages taken from the works used both verbatim and in terms of content.

Halle (Saale),

Chung-Yu Wang